CRYSTALLIZATION OF HYDROUS RHYODACITE MAGMA DURING CONTINUOUS DECOMPRESSION

A DISSERTATION SUBMITTED TO THE GRADUATE DIVISION OF THE UNIVERSITY OF HAWAIʻI AT MĀNOA IN PARTIAL FULFILLMENT OF THE REQUIREMENTS FOR THE DEGREE OF

DOCTOR OF PHILOSOPHY

IN

GEOLOGY AND GEOPHYSICS

DECEMBER 2011

By
Carrie R. Brugger

Dissertation Committee:

Julia E. Hammer, Chairperson
Michael O. Garcia
John M. Sinton
G. Jeffrey Taylor
David W. Muenow

DEDICATION

To my grandma Helene Jensen, who passed away less than a week after my oral defense of this dissertation. I know you are so proud of me and I will always be your little girl. I will forever miss you more than words could ever express. I love you!

ACKNOWLEDGEMENTS

It is my pleasure to acknowledge the many people who have helped me along the path to this Ph.D. First and foremost I would like to thank my advisor Julia Hammer for her patience, her perseverance, and never-ending support. She has shared a wealth of knowledge with me about crystallization in magmatic melts and my interest in this area has blossomed as a result of her guidance. Without her, this work truly never would have happened. I'd also like to thank Julia for allowing me to move away and pursue my dream job before my Ph.D. was complete. Thank you for believing in me!

Thank you to my committee members Mike Garcia, John Sinton, Jeff Taylor, David Muenow, and Bruce Houghton for their guidance and insights throughout this process. I appreciate how much time each of you invested in reading this dissertation and having discussions with me. I'd also like to thank all those people who have read and contributed to portions of this document along the way.

A big mahalo to all the people who have helped me through this process by providing technical support and assistance. Thank you for help in the laboratory to Julie Bowles, Lisa Petrochilos, Owen Neill, and Mac Rutherford. Thanks to Eric Hellebrand, Mike Garcia, John Donovan, and Tom Shea for their assistance with electron microprobe analyses. I'd also like to thank Gary Huss and Kazuhide Nagashima for assistance with the SEM. And finally, thanks to Scott Sitzman for setting up our EBSD, teaching us how to use it, and answering an unending stream of e-mails filled with questions.

Thank you to the many people at the University of Hawaii who encouraged and helped guide me along the way. To my various officemates Adrienne Oakley, Erin Diurba, Chris Gandy, Rebecca Carey, Jared Marske, Deb Eason, Wendy Stovall and

Alice Coleman, thanks for the companionship and for always being there when I needed it most. Thank you for allowing me to vent, for providing entertainment, and for lending an ear when I needed to bounce ideas off of someone. Thanks to all the faculty and student in VGP for the classes, field trips, and many fond memories. A special thanks to Tom Shea and Rebecca Carey for additional useful science discussions, you guys rock!

Thank you to my many friends in Hawaii who helped make this an amazing and memorable experience. Thank you to Will Koeppen, Meryl McDowell, Loÿc Vanderkluysen, Emily Chapp, Melissa Rotella, Elise Rumpf, Josh Cahill, Mikki Osterloo, Matt Patrick, Chris Bochicchio, Adrienne Oakley, Miriam Riner, Andrea Steffke, Wendy Stovall, Jared Marske, Tom Shea, and many more. I'd also like to thank my paddling ohana at WBBCC for helping me maintain my sanity. Thank you for making sure that I actually went outside and enjoyed the ocean and the Hawaiian sunshine.

Most importantly, I'd like to express my heartfelt gratitude to my family for their unwavering support. Thanks to my mom, dad, brother, and grandma who always believed in me and encouraged me along the way. Thank you for your support and encouragement, it means the world to me. And lastly, thank you to my amaZing husband Ben, who has been my rock and my shoulder to lean on through the past three years. Thank you for being there for me, I love you so much!

Financial support for this research was provided by the National Science Foundation CAREER award EAR04-49888 to Julia Hammer. Additional thanks to the University of Hawaii Graduate Student Organization for funding field work in Chile in 2007, and to Michigan Tech and the University of Iceland for financial support to attend the IAVCEI 2008 General Assembly meeting in Reykjavik, Iceland.

ABSTRACT

This dissertation examines plagioclase crystallization kinetics in a series of continuous decompression experiments on H_2O-saturated rhyodacite magma. Experimental studies provide a contextual link between observations in natural volcanic samples and interpretations of magma ascent processes because they allow examination of the kinetic response of the system to decompression and devolatilization through crystal nucleation, growth, and maturation processes.

Comparisons of plagioclase crystallization in samples decompressed at different rates reveals a strong dependence of nucleation and growth rates on decompression rate. However, a shifting balance is maintained between nuclei formation and growth of existing crystals such that a constant (non-equilibrium) total volume of plagioclase is observed in all samples at the same quench pressure, regardless of decompression rate. Comparisons of multi-step and continuous decompression experiments at the same integrated rate reveal that decompression path influences crystal textures. Thus, considerations of ascent style, in addition to rate, are necessary to strengthen the interpretive power of experimental studies for constraining natural magma ascent processes.

Crystal nucleation and growth rates derived from 3D crystal size distribution (CSD) analysis are substantially lower than corresponding values determined using 2D measurements of bulk crystal populations (batch methods). Although plagioclase growth rates are relatively constant during decompression at a given rate, the average growth rate in a rapidly decompressed sample is approximately five times faster than the growth rate in a more slowly decompressed sample. Because crystal growth rate depends on

decompression rate, CSD analysis is incapable of revealing decompression timescales or magma ascent rates without independent knowledge of crystal growth rate.

Common crystal counting techniques used in textural studies of crystal number density are affirmed using electron backscatter diffraction (EBSD). In addition, EBSD reveals a higher prevalence of growth twinning in plagioclase crystals subjected to a high degree of effective undercooling compared to crystals growing at near-equilibrium conditions. Because of the high energy boundary along twin planes, macroscopic morphological defects are dominated by these internal structural defects. Thus, formation of twins during the incipient stages of crystallization plays a first-order role in the development of anhedral microlite morphologies, including those leading to melt inclusion entrapment.

TABLE OF CONTENTS

LIST OF TABLES

LIST OF FIGURES

CHAPTER 1.

INTRODUCTION

EXPERIMENTAL STUDIES

Crystallization of a hydrous silicate melt is a consequence of either a decrease in temperature or a change in the composition of the melt (Hammer, 2008). Isobaric cooling-induced crystallization has been studied in the laboratory and in igneous rocks (e.g. Muncill & Lasaga, 1987; Cashman & Marsh, 1988) and has provided a means of estimating magma chamber residence times and calculating solidification rates of lava lakes and lava flows (Crisp *et al.*, 1994; Cashman *et al*., 1999). However, water-saturated silicate melts appear to ascend nearly isothermally (Wilson *et al*., 1980) suggesting that decompression-induced volatile exsolution, which leads to an increase in the liquidus temperature of minerals, may be the primary driving force of crystallization in volcanic conduits and domes. Previous decompression experiments have shown that natural groundmass textures form on eruptive timescales over a period of days (Geschwind & Rutherford, 1995; Hammer & Rutherford, 2002). Feldspar mode, composition, and morphology appear to depend on the decompression path, degree of supersaturation, and viscosity of the melt (Hammer & Rutherford, 2002), thus microlites in natural volcanic rocks record information about the ascent history of magma. However, interpretations of magmatic processes from textures of erupted lavas and pyroclasts require an understanding of crystallization kinetics and how textures evolve during cooling, decompression, and devolatilization (Hammer, 2008). Experimental studies are therefore essential to quantify and understand the kinetic response of crystallization to changes in temperature, pressure, and melt composition. These studies provide the fundamental link between observations of natural samples and interpretations of volcanological phenomena.

Experimental studies fall into one of two categories, differing in execution and objectives: static experiments or dynamic experiments. Static experiments consist of an initial anneal period, during which the system equilibrates at the initial conditions, followed by a single rapid perturbation to the system, either a change in temperature or pressure. This is followed by a second annealing period during which the system adjusts to the new conditions. Dynamic experiments consist of continuous regular changes in temperature and/or pressure dispersed over a period of time. The cold seal pressure vessel (CSPV) experiments described herein are dominantly dynamic, and build on previous experiments (Hammer and Rutherford, 2002) that were dominantly static.

Single-Step Decompression Experiments

Static decompression experiments are also referred to as single-step decompression because they consist of a one-time pressure drop. In these experiments, the degree of the pressure drop can be varied and the length of time a sample is allowed to anneal at the final conditions may vary, but the pressure drop itself is nearly instantaneous. This approach imposes an instantaneous discrete thermodynamic driving force for crystallization, which can be estimated using established phase equilibria for a particular system (e.g., Hammer & Rutherford, 2002; Couch, 2003a). In a single-step cooling experiment, this driving force for crystallization is the difference between the liquidus temperature in the equilibrated system before the temperature drop and the new temperature of the system, and is referred to as the "undercooling" (Hammer, 2008). In isothermal decompression studies, the driving force for crystallization is called the "effective undercooling," because no cooling is involved. Rather, effective undercooling

is the difference in temperature between the sample and the liquidus at the new pressure as defined by the phase diagram (Figure 1.1; Hammer, 2008). These static decompression experiments are ideal for studying magma crystallization in a theoretical context because this is the only method in which the effective undercooling of the system can be quantified (Hammer, 2008). In addition, examinations of the system's response to a sudden perturbation can be assessed through time by running the same experiment multiple times with various durations at the final anneal pressure.

Multi-Step Decompression Experiments

Multi-step decompression experiments are an example of dynamic experiments (Hammer, 2008). In these studies, the pressure of the system is regularly adjusted downward in a series of steps (e.g. Hammer and Rutherford, 2002; Couch, 2003a). After each pressure adjustment, the sample is left for a period of time to adjust to the new conditions, before another step is applied. These dynamic studies impose continually changing undercoolings, the magnitude of which at any instant depend on the interval and degree of the pressure drops, the crystallization kinetics of the system at the given conditions, and the kinetics at all previous steps. Thus the variation in effective undercooling through time is likely a sawtooth function, which is continually changing and cannot be ascertained from the phase diagram of the material's bulk composition (Hammer, 2008). Thus the results of dynamic experiments are less easily compared with theoretical predictions. However, they more closely match the conditions of natural magma ascent and are thus utilized in applied studies of syn-eruptive crystallization.

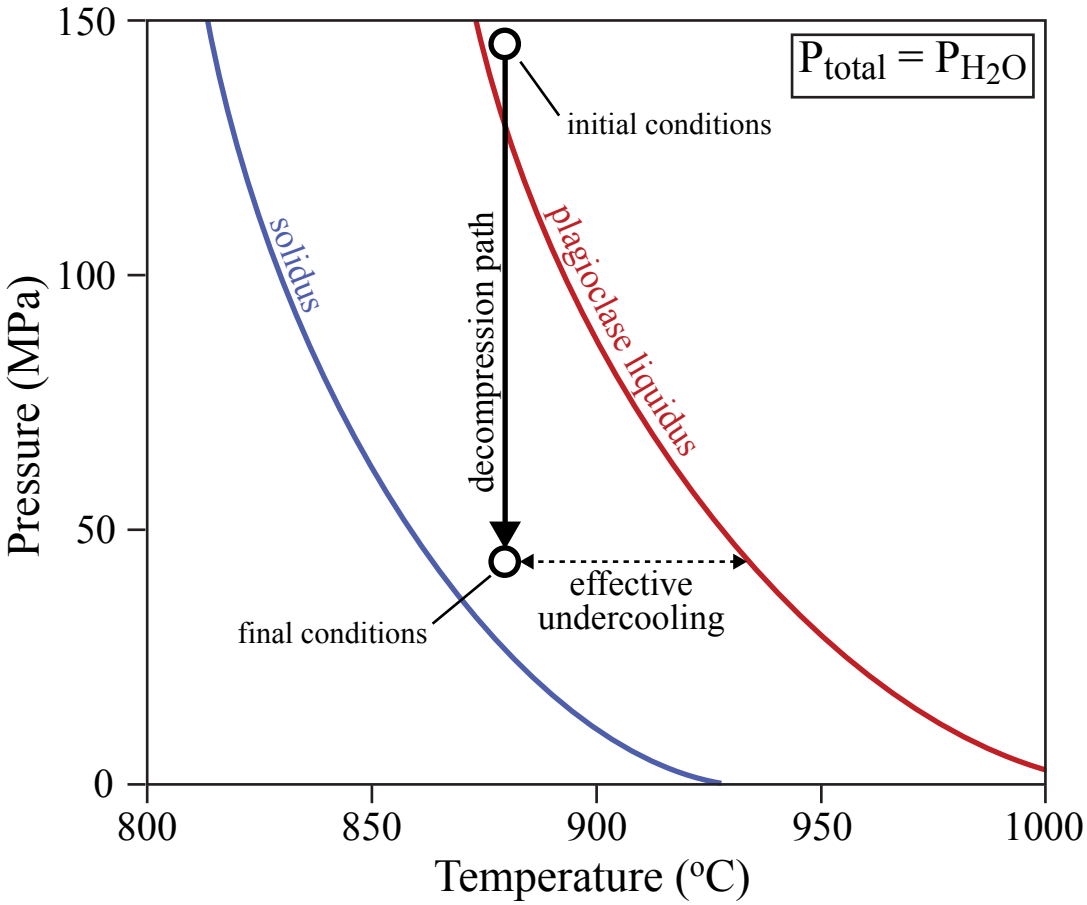

Fig. 1.1. Simplified pressure-temperature phase diagram for a water-saturated rhyodacite magma. Only the plagioclase liquidus is shown, other minerals are omitted for clarity. When a sample is suddenly decompressed, the effective undercooling is the difference in temperature between the sample and the liquidus for the phase of interest.

Continuous Decompression Experiments

The majority of experiments comprising this study are a new type of dynamic decompression experiment referred to herein as “continuous decompression” (Brugger and Hammer, 2010a). Rather than using manual steps to decompress the sample, a programmable controller continuously measures and adjusts the pressure along a predetermined pressure-time path. Continuous dynamic cooling experiments are well established as furnaces have been equipped with programmable power controllers for many years. However, there has never before been an automated method of varying the pressure of a CSPV experiment. Decompression studies have traditionally relied on manual perturbations to the system. For experiments lasting days to weeks, it is not practical to manually adjust pressure in a continuous manner, thus discrete steps are utilized. This dissertation introduces the first use of a motorized pressure variator with programmable pressure controller in dynamic decompression experiments.

ANIAKCHAK VOLCANO, ALASKA

3430 BP Caldera-Forming Eruption

The starting material for these experimental studies is rhyodacite pumice from the 3430 BP eruption of Aniakchak caldera, located 670 km southwest of Anchorage on the Alaska Peninsula (Figure 1.2). The experiments are targeted toward understanding crystallization kinetics in various environmental variables, rather than recreating the conditions specific to the 3430 BP eruption. As the eruption and deposits are not described elsewhere in this dissertation, a brief summary of physical and chemical characteristics of the deposit,

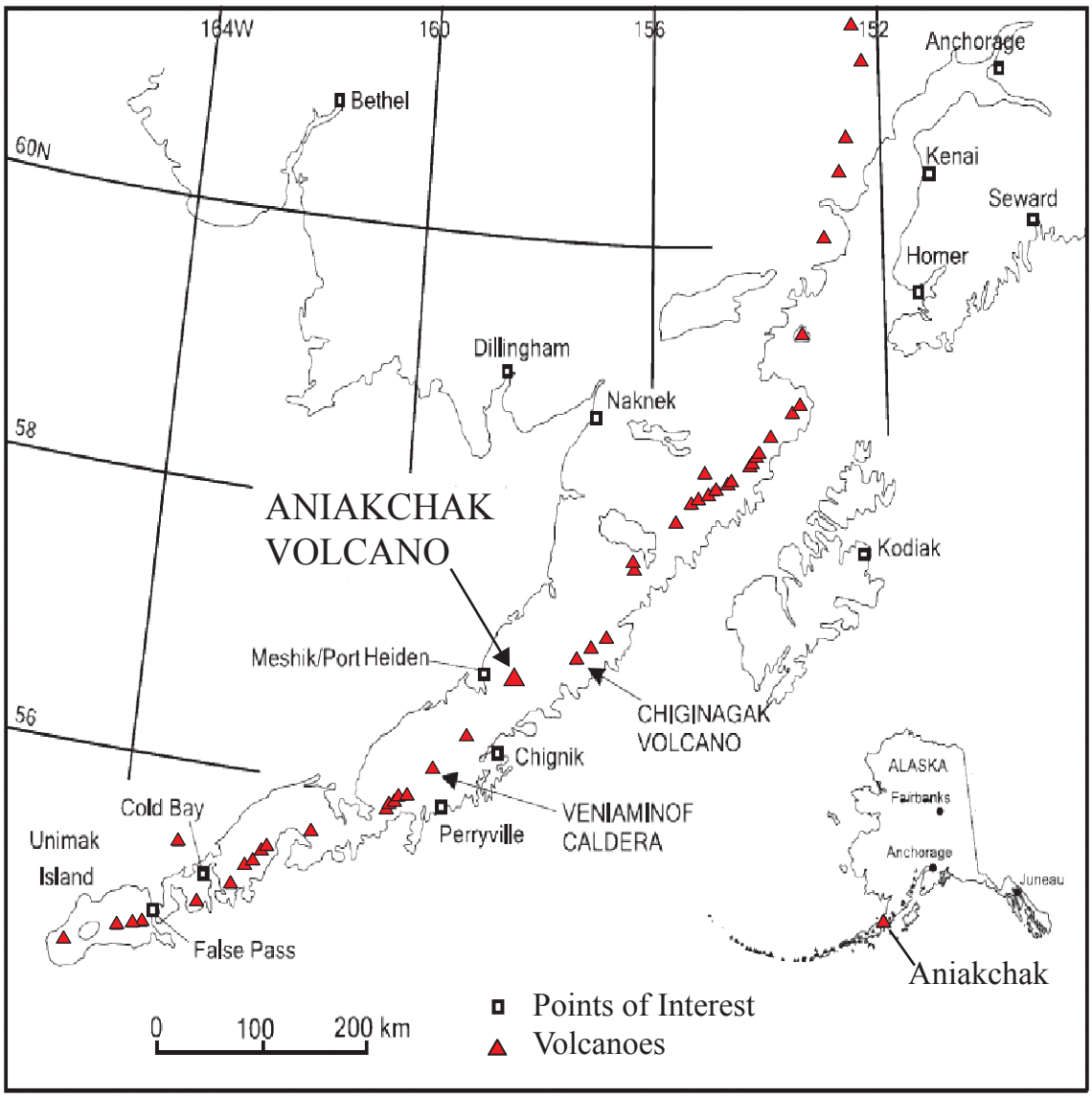

Fig. 1.2. Location map of Aniakchak Volcano on the Alaska Peninsula. After Dreher et al. (2005)

relevant phase equilibrium work on the rhyodacite, and the particular suitability of Aniakchak rhyodacite for our objectives, are provided here.

The 3420 BP eruption of Aniakchak produced a large, nearly circular caldera 10 km in diameter and abundant rhyodacite and andesite pyroclastic flow deposits (Miller & Smith, 1987; Dreher *et al*., 2005). The total eruption volume consisted of approximately 14 km^3 dense rock equivalent (DRE) of calc-alkaline rhyodacite and 13 km^3 DRE of andesite (Dreher, 2002). The bottom of the eruption deposits consist of an early homogeneous rhyodacite Plinian pumice fall overlain by a rhyodacite flow. The middle section is a mingled rhyodacite and andesite pyroclastic flow, which contains significant banding within the pumice clasts. The top of the deposit is a late erupted andesite pyroclastic flow deposit, which also contains minor banding within the scoria clasts (Dreher, 2002; Dreher *et al*., 2005).

Both the rhyodacite and the andesite pumice are crystal poor (Dreher *et al*., 2005). The rhyodacite contains approximately 2 vol% phenocrysts and no microlites. The phenocryst assemblage is dominated by plagioclase (~80%), with subordinate magnetite (~10%), orthopyroxene (~10%), clinopyroxene (~2%) and trace amounts of hornblende, ilmenite, and apatite. The andesite is more phyric, with approximately 8 vol% phenocrysts. Plagioclase is the most abundant phase (~80-85%), with smaller contributions of magnetite (~5-10%) and clinopyroxene (~5-10%), and trace amounts of ilmenite (<1%), resorbed quartz (<1%), and resorbed olivine (<1%).

Plagioclase crystals in the rhyodacite pumice suggest a fairly simple petrogenetic history of this magma, whereas plagioclase crystals in the andesite indicate a more complex history. Rhyodacite plagioclase crystals have similar compositions and display a

unimodal distribution, ranging between An_{33} and An_{41}. The crystals are euhedral and prismatic, with no complex zoning features (Larsen, 2006). In contrast, plagioclase crystals in the andesite comprise three populations. Crystals with compositions from An_{78}–An_{88} are coarsely sieved, with abundant glassy melt inclusions. Crystals in the range An_{52}-An_{59} are unsieved, and have elongate and tabular shapes. A small number of crystals have compositions within the range An_{30}-An_{40}, and these crystals are embedded in regions of clear rhyodacite glass within the andesite pumice (Larsen, 2006).

Isotopic evidence precludes the derivation of the rhyodacite magma from the andesite magma through fractionation (Dreher *et al.*, 2005). The rhyodacite represents the residual liquid from a mostly crystallized basaltic mush, with a small amount of crustal contamination by granitic country rocks, and is independent from the andesite. Dreher *et al.* (2005) concluded that the andesite magma formed prior to the caldera eruption as a result of successive mixing events involving a basaltic magma and a distinct pre-caldera rhyodacite magma exposed as a fall deposit along the modern caldera rim. This andesitic magma was also contaminated with an apatite-rich crustal component (Dreher *et al.*, 2005). The 3430 BP caldera-forming eruption was the result of influx of deeper rhyodacite magma into the andesitic magma chamber and subsequent eruption of this rhyodacite before significant mixing occurred. This injection event then triggered mixing between the rhyodacite and andesite and subsequent draining of much of the andesitic magma from the chamber (Dreher *et al.*, 2005).

Phase Equilibria Experiments

Phase equilibria experiments are a series of static (constant pressure and temperature) experiments that define the stability fields of phenocryst phases for a given magma composition. Once the phase diagram has been generated, the phase assemblages, mineral modes, glass compositions, and mineral rim compositions are compared between the natural and the experimental samples to determine which temperature-pressure conditions best reproduce the natural sample. These best-match conditions are then interpreted to represent the pre-eruptive storage conditions by assuming that the glass and phenocryst rims were in equilibrium prior to the eruption event (e.g., Rutherford *et al.*, 1985; Rutherford & Devine, 1996).

Larsen (2006) performed water-saturated phase equilibria experiments and comparisons with petrologic data from the eruptive products to determine the pre-eruptive storage conditions of the 3430 year-old Aniakchak rhyodacite (Figure 1.3). Water saturation was assumed after studying the dissolved water contents of melt inclusions and based on the presence of amphibole in the sample. The oxygen fugacity of the system was $10^{-10.6}$ to $10^{-11.8}$ bars, as determined from Fe-Ti oxide geobarometry (Larsen, 2006). Based on this phase equilibria work, Larsen (2006) concluded that the pre-eruptive storage conditions of the rhyodacite magma were 870-880°C and 125-150 MPa. All experiments presented in this study began with an initial equilibrium period at 880°C and 130 MPa before decompression commenced.

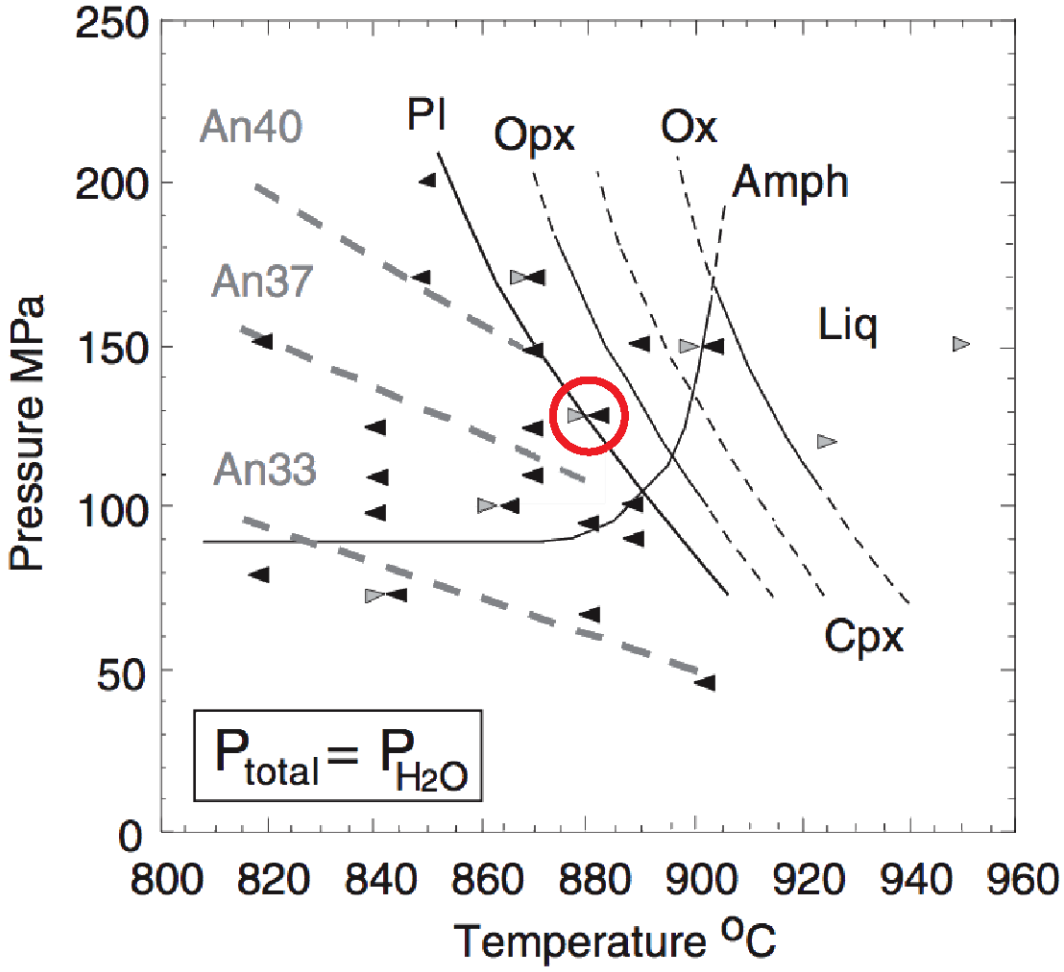

Fig. 1.3. Pressure-temperature phase diagram for the rhyodacite magma erupted from Aniakchak Volcano 3430 years ago as determined by phase equilibria experiments of Larsen (2006). All experiments were water-saturated, thus $P_{total}=P_{H_2O}$. Experimental runs are shown with triangles, the direction they point indicates the directional approach to equilibrium. Black triangles represent crystallization experiments with powdered natural pumice as the starting material. Gray triangles represent reversal experiments performed with crystal-rich starting materials of the same bulk composition. Phase-in boundaries for plagioclase (pl), orthopyroxene (opx), clinopyroxene (cpx), oxides (ox), and amphibole (amph) are shown with solid black lines where well constrained and dashed lines where more uncertain. The dashed gray lines represent the approximate change in plagioclase composition as a function of pressure (P_{H_2O}) and temperature. The red circle indicates the temperature and pressure conditions which best reproduce the phase assemblage, glass composition and plagioclase composition of the rhyodacite pumice. Thus 880°C and 130 MPa were the starting conditions used in all experiments in this dissertation.

Suitability of the Aniakchak Rhyodacite Pumice for Decompression Experiments

The rhyodacite pumice from Aniakchak is an ideal starting material for experimental studies of crystallization because it is abundant, nearly crystal free, and compositionally not yet fully evolved. The low phenocryst content of this magma indicates near-liquidus conditions in the magma chamber prior to the eruption, and the absence of microlites indicates that the ascent was too rapid for syn-eruptive crystallization to occur (e.g., Rutherford & Gardner, 2000). Low pre-existing crystal content is ideal for nucleation studies because undercooling (or effective undercooling) forces the formation of new crystals. In contrast, selection of a crystal-rich starting material would require significant prior superheating to create a fully liquid starting material, thus introducing experimental variables (superheat duration and magnitude) known to cause barriers to nucleation (Walker, 1978). The naturally low crystallinity of the starting material also simplifies quantification of growth on pre-existing crystals and reduces problems associated with determining which crystals nucleated during experiments and which crystals are inherited from the starting material. Prior experiments using compositions near the granite minimum (Hammer & Rutherford, 2002) showed the difficulty in tracking crystallinity through analysis of the coexisting glass. The Aniakchak rhyodacite is far enough from compositional invariance that the liquid's composition evolves with progressive crystallization, facilitating determination of crystal mode and crystal abundance through probe microanalysis of the glass phase.

DISSERTATION OUTLINE

This dissertation contains three main sections that examine various aspects of plagioclase crystallization in a set of continuous decompression experiments, which used rhyodacite pumice from the 3430 caldera-forming eruption of Aniakchak Volcano as starting material. The goal was not to study any particular aspect of the eruption that produced our starting material, but rather to evaluate factors germane to crystallization kinetics of all evolved magmas using continuous decompression experiments. This pumice was utilized simply because of its suitability for experimental studies (see above).

Chapter 2 explains the experimental design and summarizes the broad results of the decompression experiments. The chemical evolution of the melt and plagioclase crystals and textural development of plagioclase are examined along each decompression path and between four different decompression rates. This chapter also presents comparisons between continuous and multi-step decompression experiments.

Chapter 3 presents an in-depth examination of the crystal size distributions (CSD) along two of the decompression paths. Crystal nucleation and growth rates derived from CSDs using standard assumptions are compared with values obtained using batch textural crystallization techniques. This chapter also evaluates the method of using CSDs to calculate decompression timescales and magma ascent rates.

Chapter 4 utilizes electron backscatter diffraction (EBSD) to examine the internal crystallography of plagioclase crystal in a highly undercooled sample and a sample that crystallized under near-equilibrium conditions. Assumptions commonly employed in crystal number density studies regarding the relationships between contiguous crystals are evaluated using crystallographic relationships. The relationship between the internal

crystallographic structures of grains and the disequilibrium morphological features commonly observed in highly undercooled melts is elucidated.

Chapters 2 and 3 have been published in peer-reviewed journals. Chapter 2 was published in the Journal of Petrology in September 2010, and Chapter 3 was published in Earth and Planetary Science Letters in December 2010. Chapter 4 will be submitted to American Mineralogist. Because Chapters 2 and 3 are included unmodified from their original contents, their introductions contain similar material.

CHAPTER 2.

CRYSTALLIZATION KINETICS IN CONTINUOUS DECOMPRESSION EXPERIMENTS: IMPLICATIONS FOR INTERPRETING NATURAL MAGMA ASCENT PROCESSES

Published in its present form as Brugger, C.R. and Hammer, J.E. (2010) Journal of Petrology, 51, 1941-1956. doi:10.1093/petrology/egq044

ABSTRACT

Decompression experiments were performed to study the kinetics of plagioclase crystallization during ascent of hydrous rhyodacite magma. These experiments differ from previous studies in that they employ a continuous, rather than stepwise, pressure-time trajectory. Four series of experiments were performed at rates of 0.5 to 10 MPa h^{-1}, corresponding to ascent rates of ~0.007 to 0.14 m s^{-1}. Experiments quenched along each decompression path allow snapshot-style monitoring of progressive crystallization. As expected, rates of plagioclase nucleation and growth depend strongly on decompression rate. Regardless of decompression rate, approximately equal volumes of feldspar crystallize during a given decompression interval, even when the observed crystallinity is lower than the equilibrium crystallinity. Apparently, a constant degree of solidification is maintained by a crystallization mechanism striking a shifting balance between nuclei formation and growth of existing crystals. Other key results pertain to the efficacy with which experimental results enable interpretation of the decompression histories of natural rocks. Feldspar microlites do not maintain chemical equilibrium with melt. They are more anorthite-rich than equilibrium plagioclase, suggesting that interpretations of magma ascent processes in nature require comparisons with dynamic rather than static (phase equilibrium) experiments. While decompression rate is an important element controlling final textures in volcanic rocks, no single compositional or textural parameter uniquely records this rate. Of the criteria examined, microlite number density and morphology are the best indicators of magma decompression rate. Based on a small number of comparisons between continuous and multi-step decompression style at the same time-integrated decompression rate (1 MPa h^{-1}), decompression path evidently

influences crystal texture, with stepwise decompression yielding textures correlative with faster decompression than indicated by the time-integrated decompression rate. Thus, consideration of magma ascent style, in addition to rate, will undoubtedly strengthen the interpretive power of experimental studies for constraining natural magma ascent processes.

INTRODUCTION

Magma ascent processes are increasingly recognized as controlling the style of volcanic activity, thus explaining the intensity of research on post-eruption indicators of ascent rate. For example, the rate at which magma ascends from a storage zone has been estimated using a number of techniques, including seismicity during eruptive periods (Endo *et al*., 1990; Scandone & Malone, 1985; Lees & Crosson, 1989), plagioclase size distributions (Cashman, 1988, 1992), and reaction rim development on amphibole phenocrysts (Rutherford & Hill, 1993; Rutherford & Devine, 1997). A magmatic closure pressure, or pressure at which kinetic factors inhibit further crystallization and melt chemistry is frozen-in, has been identified in natural volcanic rocks from elevated volatile contents (Newman *et al*., 1988; Blundy & Cashman, 2008; Castro & Gardner, 2008). Laboratory decompression experiments performed on hydrous magmas of intermediate composition demonstrate that feldspar abundance, composition, and morphology depend on the decompression path, degree of mineral supersaturation, and viscosity of the melt (Hammer & Rutherford, 2002), thus suggesting that ascent processes are recorded in crystal textures. Decompression drives crystallization because declining H_2O solubility causes volatile exsolution (Burnham & Davis, 1971, Moore *et al*., 1998, Papale *et al*.,

2006), and subsequent increases in the temperature at which mineral phases form (Wilson *et al.*, 1980; Eichelberger, 1995). Moreover, experiments demonstrate that natural groundmass textures form on eruptive timescales (Geschwind & Rutherford, 1995; Hammer & Rutherford, 2002). The provisional success of the experimental approach for addressing crystallization processes during eruptive decompression suggests that quantitative constraints on the ascent histories of erupted magma may be gleaned ultimately from the groundmass textures of natural rocks (Cashman & Blundy, 2000).

While the exact nature of magma ascent is not understood, it likely displays temporal and spatial variability among volcanic systems. Magma ascent may at times be intermittent and pulsatory, with rapid accelerations followed by irregular pauses, while at other times it may consist of steady fluid flow. The only previous experiments to employ continuous decompression have imposed very rapid decompression (typically >50 MPa h^{-1}) using a manually operated bleed valve, and they have primarily focused on studies of volatile exsolution, bubble nucleation, and bubble growth processes (e.g., Gardner *et al*., 1999; Mangan & Sisson, 2000; Martel & Schmidt, 2003). Ascent rates of this magnitude correspond to intense explosive eruptions, which typically produce microlite-free materials because the time scales are too short for appreciable groundmass crystallization. In contrast, crystallization in ascending silica-rich magmas, whether natural or synthetic, requires time scales of days to weeks (Rutherford & Gardner, 2000; Martel & Schmidt, 2003). Out of necessity, nearly all decompression-induced crystallization experiments have utilized a stepped technique, either single-step decompression (SSD) or multi-step decompression (MSD) (e.g., Hammer & Rutherford, 2002; Couch *et al*., 2003b; Martel & Schmidt, 2003). In SSD experiments, the pressure is changed manually and

instantaneously using a pressure bleed valve from an initial pressure (P_i) to a final pressure (P_f), held at P_f for a period of time, and then quenched. Using variable run times at P_f, this type of experiment can be used to study the evolution of magma in response to a pressure perturbation. In addition, this method provides the only means of applying a known degree of effective undercooling to the sample, and thus it is preferred for placing crystal nucleation and growth rate kinetics in a theoretical context (Hammer, 2004; 2008). However, SSD experiments do not simulate the natural magma ascent process. MSD experiments, which consist of a series of small pressure drops and dwell periods, have been used to study syn-eruptive crystallization and make interpretations about magma ascent rates at various volcanic centers (Hammer & Rutherford, 2002; Coombs *et al*., 2003; Couch *et al*., 2003b, Martel & Schmidt, 2003; Nicholis & Rutherford, 2004; Browne & Gardner, 2006; Szramek *et al*., 2006; Suzuki *et al*., 2007; Castro & Gardner, 2008). The MSD approach is thought to closely approximate natural magma ascent because the small steps in pressure are regarded as insignificant in comparison with the total amount of decompression. However, the effects of varying pressure- and time-step size on resulting crystal textures has never been investigated. Comparisons between stepped and continuous experiments at the same time-integrated decompression rate allow preliminary evaluation of the effects of decompression style on crystal textures.

Here we report the results of continuous decompression experiments performed in a new hydraulically driven screw pump pressure variator with programmable controller. This instrument was designed (Harwood Engineering, Walpole, MA) to measure and control pressure to within a 0.5 MPa tolerance over a 0-300 MPa pressure range using a motorized screw jack that drives a piston out of a large capacity pressure vessel. The

objectives of this research are to (a) examine the evolution of crystal textures during continuous decompression (CD) of H_2O-saturated rhyodacite magma, (b) quantify the effect of decompression rate on crystal texture and phase compositions, and (c) evaluate any differences between continuous and multi-step decompression experimental methods using a small number of pilot experiments. We also evaluate the degree to which chemical equilibrium is reached in each run product, in order to determine whether any ascent histories promote crystal-melt equilibrium or, conversely, preclude attainment of equilibrium. Experimental results are compared with prior work and a calculated equilibrium liquid line of descent, and we consider plagioclase-melt equilibria in the context of binary T-X phase relations. We conclude with cautionary remarks regarding the interpretation of magma decompression rate from groundmass crystal textures.

METHODS

Starting Material

The experimental starting material consists of lightly crushed pyroclasts from the 3430 yBP caldera-forming ignimbrite of Aniakchak Volcano in the Aleutian Arc (Table 2.1, Figure 2.1). The experiments are considered germane to crystallization in natural H_2O-rich evolved silicic magmas from a variety of volcanic settings because kinetics of crystallization in hydrous rhyodacites at the experimental temperature (880˚C) should be similar. That is, the present study is relevant to groundmass crystallization in less-evolved

Table 2.1. Bulk chemical composition of Aniakchak rhyodacite starting material, wt%

SiO_2	TiO_2	Al_2O_3	FeOt	MnO	MgO	CaO	Na_2O	K_2O	P_2O_5
71.11	0.56	15.76	2.69	0.15	0.53	2.16	5.69	2.99	0.12

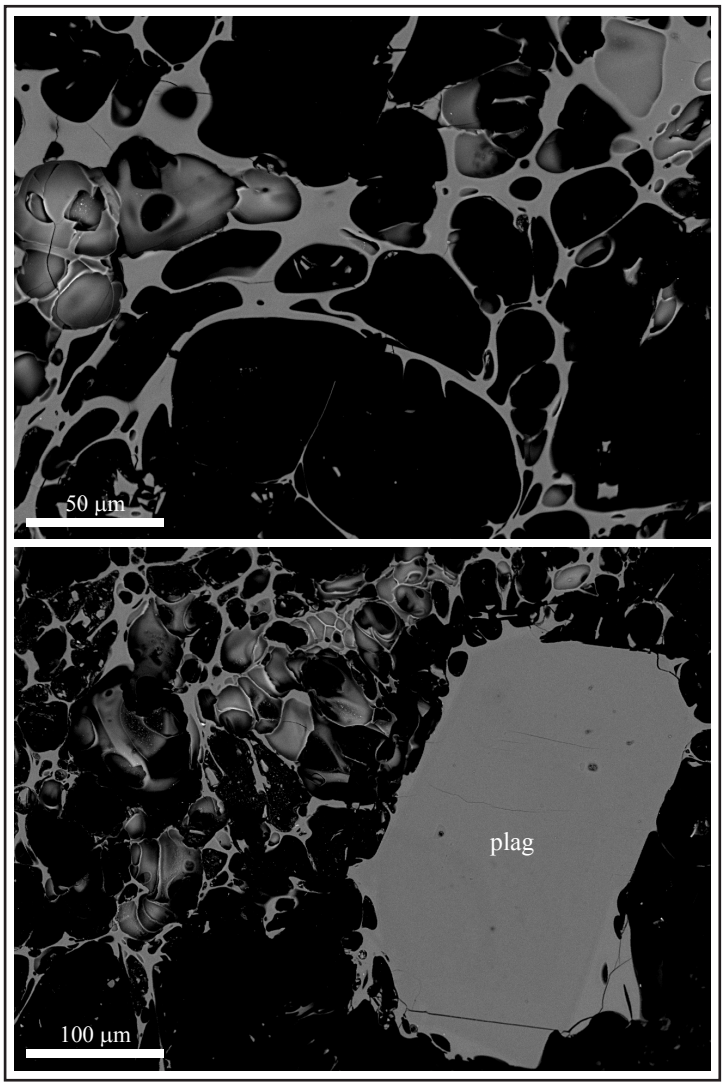

Fig. 2.1. Backscatter electron images of the Aniakchak Volcano pumice used as a starting material for decompression experiments. This rock contains very few phenocrysts (~2 vol. %) and no plagioclase crystals in the size range created in these experiments (≤100 mm). Void space is black and glass is gray. The lower image shows a typical plagioclase phenocryst (plag), which is slightly darker gray than the glass.

natural magmas—andesites and dacites—possessing a rhyodacite matrix melt composition. This rock is unaltered and contains very few crystals (~2 vol% phenocrysts and no microlites; Dreher *et al*., 2005) compared with other similarly prepared natural starting materials (e.g., Hammer & Rutherford, 2002), which reduces the problems of (a) determining which crystals nucleate during an experiment and which crystals are inherited from the starting material, and (b) quantifying the amount of growth on newly-formed and pre-existing crystals. The dominant crystallizing phase is plagioclase, the principal focus of textural studies in natural rocks (e.g., Gardner *et al*., 1998; Hammer *et al*., 1999; Cashman & Blundy, 2000; Hammer *et al*., 2000; Martel & Poussineau, 2007).

Experimental Methods

The initial conditions for decompression experiments are adopted from the pre-eruptive storage conditions determined by Larsen (2006) for this rhyodacite: 870-880°C, oxygen fugacity corresponding to 0.8 ± 0.2 log units above the Ni+NiO (NNO) buffer, and 110-140 MPa. Charges were held at the starting conditions for at least 24 hours prior to decompression. The decompression experiments were run H_2O-saturated (P_{H2O} = P_{TOTAL}) at a constant temperature of 880°C, initiated from 130 MPa (P_i). Pumice clasts were lightly crushed (rather than powdered) to reduce exposure of phenocryst cores to the matrix melt (Pichavant *et al*., 2007), with which they are not in equilibrium. The starting material was placed inside $Ag_{70}Pd_{30}$ capsules along with distilled water sufficient to saturate the melt with a vapor at the starting conditions (≥ 4.3 wt% according to Moore *et al*., 1998).

Two families of experiments were employed. The first comprised a series of runs quenched at regular pressure intervals along a given decompression path (Table 2.2). These are termed “snapshot” experiments, because they record the state of the magma at specific pressures during decompression. Interpretations about the evolution of crystal textures through time rest on the assumption that samples decompressed at the same rate follow identical crystallization trajectories. Thus, we infer that a sample quenched at low pressure was previously indistinguishable from a sample quenched at higher pressure. The second family of experiments are called “anneal” experiments because at some point during the decompression they were isolated from the variator and held at a constant pressure for 65-1295 hours (Table 2.2), with the duration contingent on the decompression rate and quench pressure. These anneal durations are similar to or exceed dwell periods used in experimental equilibrium studies at similar temperatures, H_2O contents, and bulk compositions (Larsen, 2006; Couch *et al*., 2003a; Hammer *et al*., 2002; Rutherford *et al*., 1985). Chemical equilibrium of anneal samples was evaluated using the time-variance of the matrix glass composition among otherwise identical experiments held at the same final pressure (Table 2.2, 2.3).

All experiments were run in cold-seal Waspaloy® pressure vessels using methods described in detail previously (Geschwind & Rutherford, 1992; Gardner *et al*., 1995; Hammer & Rutherford, 2002). Briefly, oxygen fugacity was buffered at the run conditions using a short section of Ni filler rod (~15mm), temperature was maintained at 880˚C using an external thermocouple, and static pressure was applied to the capsules using water as the pressurizing medium and monitored using a factory-calibrated Heise gauge providing 0.5 MPa precision. During CD experiments, pressure was controlled to

Table 2.2. Decompression experiments and results

sample number	type	decompression rate (MPa h^{-1}) [a]	P_f (MPa)	decompression duration (hrs)	time at P_f (hrs)	N_A (mm^{-2})	ϕ[b]
6-1	snapshot	10	5	12.6	0	16976 (6179)	0.213 (7)
20-2	snapshot	10	45	8.6	0	9362 (4103)	0.122 (7)
12-2	snapshot	10	68	6.3	0	5732 (2353)	0.077 (5)
5-4	snapshot	10	87	4.4	0	11 (15)	0.001 (0)
12-1	snapshot	10	109	2.2	0	21 (17)	0.003 (1)
6-2	anneal	10	5	12.6	342	16070 (5978)	0.509 (9)
17-3	anneal	10	5	12.6	1302	21053 (846)	0.475 (9)
20-3	anneal	10	26	10.6	219	3029 (1205)	0.283 (7)
5-1	anneal	10	45	8.6	141	301 (89)	0.215 (7)
5-2	anneal	10	87	4.4	90	68 (25)	0.062 (3)
20-1	anneal	10	87	4.4	240	102 (49)	0.083 (4)
18-3	snapshot	2	5	64.9	0	31664 (6481)	0.274 (6)
BJ3	snapshot	2	26	52.9	0	26683 (3367)	0.193 (6)
18-2	snapshot	2	45	44.4	0	17847 (7811)	0.154 (5)
18-1	snapshot	2	68	32.3	0	155 (118)	0.015 (2)
14-2	snapshot	2	87	22.4	0	541 (307)	0.026 (4)
14-1	snapshot	2	109	10.8	0	23 (16)	0.004 (1)
11-1	anneal	2	5	64.9	588	15127 (10815)	0.446 (6)
18-5	anneal	2	45	44.4	94	329 (144)	0.153 (5)
18-4	anneal	2	87	22.3	285	2646 (6435)	0.040 (3)
15-4	snapshot	1	5	134.9	0	347 (49)	0.222 (8)
15-3	snapshot	1	26	111.7	0	1028 (587)	0.156 (6)
15-2	snapshot	1	45	92.4	0	20875 (4191)	0.193 (6)
16-2	snapshot	1	68	66.7	0	7460 (2957)	0.089 (5)
15-1	snapshot	1	87	46.5	0	3809 (1180)	0.032 (4)
16-1	snapshot	1	109	22.5	0	1788 (618)	0.028 (3)
15-7	anneal	1	5	134.9	915	8309 (6518)	0.454 (7)
15-6	anneal	1	45	92.4	813	23074 (9605)	0.225 (6)
15-5	anneal	1	87	46.4	528	14 (27)	0.054 (3)
13-3	snapshot	0.5	5	279.3	0	2510 (593)	0.250 (6)
13-1	snapshot	0.5	26	231.0	0	13708 (3924)	0.203 (7)
8-1	snapshot	0.5	45	197.7	0	6938 (2541)	0.137 (7)
21-1	snapshot	0.5	68	144.0	0	3262 (2117)	0.081 (4)
7-2	snapshot	0.5	87	99.9	0	13586 (6105)	0.088 (5)
7-1	snapshot	0.5	109	48.4	0	15559 (5564)	0.092 (4)
13-2	anneal	0.5	5	279.5	1295	14489 (2642)	0.513 (9)
8-3	anneal	0.5	45	197.8	619	15015 (6866)	0.219 (8)
7-4	anneal	0.5	87	99.9	65	19677 (2441)	0.112 (5)
23-1	anneal	n.a.	130	0.0	n.a.	-	-
23-2	anneal	n.a.	130	0.0	n.a.	-	-
10-4[c]	SSD	n.a.	5	0.0	1010	-	-
10-5	SSD	n.a.	45	0.0	966	17909 (7360)	0.225 (6)
10-1	SSD	n.a.	87	0.0	964	4706 (2933)	0.102 (6)
22-2	MSD	1	5	134.2	n.a.	1019 (989)	0.144 (5)
22-1	MSD	1	26	111.6	n.a.	13 (9)	0.004 (2)

[a] The pressure variator's true decompression rate is slightly faster than the programmed rate shown here.
[b] In this column the values in parentheses represent one sigma error bars when multiplied by 10^{-3}.
[c] Crystals in the 5 MPa SSD experiment are too small to perform textural characterization.

Table 2.3. Experimental matrix glass compositions, wt%

sample	n[a]	SiO_2[b]	TiO_2	Al_2O_3	FeOt	MnO	MgO	CaO	Na_2O	K_2O	P_2O_5	total
6-1	9	72.29 (87)	0.27 (8)	13.57 (31)	1.19 (6)	0.13 (2)	0.26 (3)	0.61 (9)	5.00 (41)	3.92 (15)	0.07 (5)	97.31
12-3	10	70.92 (72)	0.33 (7)	14.93 (16)	1.56 (13)	0.12 (2)	0.38 (2)	1.58 (5)	5.47 (27)	2.96 (2)	0.06 (3)	98.31
20-2	9	69.56 (115)	0.35 (5)	14.51 (43)	1.29 (12)	0.14 (2)	0.38 (2)	1.32 (28)	5.13 (26)	3.12 (18)	0.06 (4)	95.84
12-2	10	69.14 (52)	0.33 (4)	13.71 (30)	1.49 (12)	0.11 (2)	0.33 (3)	1.18 (18)	5.12 (11)	3.09 (15)	0.02 (2)	94.52
5-4	9	67.95 (68)	0.25 (9)	14.13 (13)	1.83 (11)	0.10 (4)	0.22 (2)	1.46 (5)	5.09 (10)	2.84 (6)	0.02 (2)	93.88
12-1	10	67.06 (45)	0.23 (9)	13.96 (15)	1.60 (10)	0.08 (4)	0.24 (4)	1.42 (4)	5.02 (10)	2.90 (5)	0.01 (1)	92.51
6-2	8	75.29 (105)	0.28 (7)	11.29 (47)	1.36 (13)	0.07 (2)	0.03 (0)	0.20 (5)	3.79 (18)	4.80 (10)	0.07 (4)	97.18
17-3	8	75.42 (85)	0.37 (16)	11.92 (89)	1.32 (46)	0.07 (2)	0.08 (1)	0.28 (5)	3.90 (45)	4.73 (39)	0.03 (2)	98.12
20-3	12	74.19 (102)	0.36 (7)	12.15 (15)	1.29 (4)	0.08 (2)	0.14 (1)	0.51 (9)	4.37 (32)	4.03 (10)	0.06 (6)	97.18
5-1	10	74.31 (113)	0.33 (3)	13.08 (34)	1.22 (8)	0.10 (3)	0.21 (2)	0.74 (14)	3.90 (33)	3.43 (11)	0.07 (9)	97.39
5-2	11	68.78 (44)	0.31 (13)	14.06 (16)	1.61 (14)	0.11 (5)	0.36 (4)	1.48 (13)	5.23 (7)	2.92 (7)	0.04 (3)	94.91
20-1	10	70.95 (53)	0.24 (7)	13.27 (13)	1.07 (9)	0.11 (5)	0.29 (2)	0.98 (7)	4.94 (15)	3.21 (8)	0.02 (3)	95.08
18-3	10	74.67 (93)	0.38 (14)	12.98 (39)	1.38 (18)	0.14 (2)	0.29 (4)	0.35 (5)	4.75 (42)	4.14 (14)	0.05 (3)	99.14
BJ3	10	74.11 (123)	0.32 (7)	12.91 (19)	1.12 (9)	0.11 (3)	0.27 (1)	0.46 (2)	4.43 (21)	3.76 (3)	0.03 (2)	97.53
18-2	8	72.57 (127)	0.32 (11)	13.28 (30)	1.00 (19)	0.11 (2)	0.27 (9)	0.61 (8)	4.20 (29)	3.31 (7)	0.05 (2)	95.71
18-1	6	71.21 (138)	0.39 (8)	14.26 (16)	1.36 (24)	0.12 (1)	0.30 (2)	1.28 (5)	5.15 (25)	3.13 (4)	0.06 (2)	97.24
14-2	10	69.30 (58)	0.33 (10)	13.93 (42)	1.39 (32)	0.08 (2)	0.25 (2)	1.26 (18)	5.16 (12)	3.06 (13)	0.04 (3)	94.80
14-1	10	68.35 (49)	0.32 (6)	13.93 (15)	1.49 (7)	0.10 (4)	0.32 (2)	1.33 (4)	5.13 (8)	2.96 (7)	0.01 (2)	93.94
11-1	8	75.81 (142)	0.36 (7)	11.26 (62)	1.20 (13)	0.06 (2)	0.06 (1)	0.26 (7)	3.83 (35)	4.71 (12)	0.03 (3)	97.59
18-5	9	72.55 (118)	0.35 (9)	13.72 (37)	1.35 (7)	0.11 (3)	0.31 (2)	0.89 (12)	4.43 (22)	3.34 (12)	0.09 (7)	97.14
18-4	11	70.04 (41)	0.33 (5)	13.65 (17)	1.35 (13)	0.12 (3)	0.34 (3)	1.14 (8)	5.04 (9)	3.16 (9)	0.03 (2)	95.20
15-4	9	74.01 (75)	0.34 (5)	13.95 (49)	1.67 (8)	0.15 (2)	0.27 (3)	0.82 (5)	4.77 (32)	3.79 (6)	0.05 (4)	99.83
15-3	10	72.27 (86)	0.35 (8)	13.91 (41)	1.31 (10)	0.14 (2)	0.34 (1)	0.92 (14)	5.30 (12)	3.49 (6)	0.07 (3)	98.10
15-2	7	75.48 (76)	0.32 (6)	13.17 (7)	1.04 (16)	0.10 (3)	0.21 (4)	0.48 (5)	4.19 (20)	3.45 (9)	0.05 (3)	98.50
16-2	10	71.30 (35)	0.41 (8)	13.52 (16)	1.37 (12)	0.09 (4)	0.32 (2)	0.94 (9)	4.96 (13)	3.20 (5)	0.01 (1)	96.12
15-1	10	69.51 (73)	0.34 (7)	14.00 (49)	1.22 (12)	0.10 (3)	0.33 (7)	1.31 (25)	4.94 (17)	3.01 (11)	0.03 (3)	94.79
16-1	10	67.96 (38)	0.32 (6)	13.80 (14)	1.37 (10)	0.12 (2)	0.36 (3)	1.32 (7)	4.97 (9)	3.02 (4)	0.02 (4)	93.25
15-7	11	78.14 (109)	0.33 (5)	11.28 (92)	1.15 (9)	0.05 (2)	0.07 (1)	0.25 (7)	3.63 (33)	4.83 (12)	0.06 (5)	99.81
15-6	10	75.40 (73)	0.27 (9)	12.77 (31)	1.23 (12)	0.09 (2)	0.15 (1)	0.63 (13)	4.47 (21)	3.81 (9)	0.04 (5)	98.85
15-5	10	70.22 (13)	0.37 (7)	13.73 (9)	1.28 (8)	0.08 (3)	0.35 (2)	1.23 (3)	5.07 (9)	3.12 (5)	0.04 (4)	95.49
13-3	11	74.15 (73)	0.32 (5)	12.81 (17)	1.28 (9)	0.09 (2)	0.13 (2)	0.31 (4)	4.47 (33)	4.44 (3)	0.03 (3)	98.03
13-1	10	74.67 (101)	0.33 (5)	12.79 (10)	1.14 (7)	0.11 (2)	0.25 (2)	0.42 (2)	4.69 (25)	3.80 (4)	0.03 (2)	98.24
8-1	10	73.83 (84)	0.31 (6)	13.17 (10)	1.03 (6)	0.13 (2)	0.30 (1)	0.55 (2)	4.67 (30)	3.63 (3)	0.05 (3)	97.66
21-1	10	71.27 (37)	0.43 (4)	13.40 (26)	1.23 (6)	0.13 (3)	0.31 (3)	0.89 (11)	4.88 (11)	3.30 (4)	0.02 (3)	95.85
7-2	8	70.43 (47)	0.31 (6)	13.33 (34)	1.07 (12)	0.09 (4)	0.30 (5)	0.91 (16)	4.90 (16)	3.21 (12)	0.02 (3)	94.57
7-1	10	69.15 (53)	0.23 (12)	13.74 (33)	1.44 (10)	0.09 (3)	0.17 (2)	1.10 (13)	4.96 (9)	3.04 (9)	0.004 (10)	93.92
13-2	6	77.24 (68)	0.31 (5)	10.33 (15)	1.76 (16)	0.07 (2)	0.06 (1)	0.20 (2)	3.14 (26)	4.60 (30)	0.02 (4)	97.73
8-3	10	74.77 (65)	0.27 (7)	12.24 (9)	0.98 (7)	0.08 (3)	0.18 (1)	0.52 (10)	4.44 (16)	3.82 (6)	0.05 (7)	97.36
7-4	5	70.64 (65)	0.26 (6)	13.24 (38)	0.90 (9)	0.07 (1)	0.21 (2)	0.91 (21)	4.78 (12)	3.29 (12)	0.03 (2)	94.31
23-1	9	67.11 (35)	0.45 (6)	14.10 (20)	2.35 (9)	0.12 (3)	0.54 (1)	1.68 (5)	5.09 (9)	2.71 (6)	0.03 (2)	94.18
23-2	10	67.29 (52)	0.43 (7)	14.02 (15)	2.29 (7)	0.13 (3)	0.56 (1)	1.71 (4)	5.12 (8)	2.76 (4)	0.03 (3)	94.35
10-5	10	69.50 (113)	0.36 (7)	12.96 (15)	1.15 (10)	0.08 (3)	0.20 (1)	0.49 (1)	4.58 (26)	4.17 (6)	0.03 (2)	93.53
10-1	8	71.28 (64)	0.32 (5)	13.61 (15)	1.08 (11)	0.12 (1)	0.25 (1)	0.80 (2)	4.64 (37)	3.30 (4)	0.03 (1)	95.42
22-2	11	71.20 (83)	0.38 (8)	15.05 (22)	1.76 (12)	0.15 (1)	0.42 (7)	1.31 (26)	5.34 (37)	3.70 (20)	0.06 (5)	99.39
22-1	8	70.97 (51)	0.42 (5)	15.12 (15)	1.56 (21)	0.15 (3)	0.53 (2)	1.68 (5)	4.90 (26)	3.05 (4)	0.09 (2)	98.48

[a] Number of microprobe analyses averaged to determine the average glass composition and estimated error.
[b] Values in parentheses represent one sigma errors when multiplied by 10^{-2}.

within ±0.5 MPa by the pressure variator, and regularly checked against the Heise gauge. Snapshot experiments were quenched immediately upon reaching their final pressure. When an anneal experiment reached final pressure (P_f) it was isolated from the variator and pressure was checked daily. All experiments were quenched by removing the pressure vessel from the furnace and quickly inverting it so that the charge fell to the water-cooled end (after Mangan & Sisson, 2000), which is estimated to cool samples by 300˚C within 6 seconds.

Continuous decompression (CD) experiments were run at four decompression rates: 0.5, 1, 2, and 10 MPa h^{-1} (Table 2.2). The slowest decompression rate corresponds to an ascent rate (~0.007 m s^{-1}) typical of a dome-building effusive eruption (e.g., Mount St Helens), while the fastest decompression simulates an ascent rate (~0.14 m s^{-1}) corresponding to that preceding low-intensity explosive activity (Rutherford & Gardner, 2000). Along each decompression path, six snapshot experiments and three anneal experiments were performed, with snapshots at 109, 87, 68, 45, 26 and 5 MPa, and anneal runs at 87, 45, and 5 MPa (Table 2.2). Three single-step decompression (SSD) experiments were performed and quenched at 87, 45 and 5 MPa. In addition, two multi-step decompression (MSD) experiments were conducted using a pressure step of 10 MPa every 10 hours, which is equivalent to a time-integrated decompression rate of 1 MPa h^{-1}. The MSD decompression experiments were quenched at 26 and 5 MPa, and performed according to previously published techniques (e.g., Hammer & Rutherford, 2002; Couch, 2003b; Martel & Schmidt, 2003; Browne & Gardner, 2006; Szramek *et al*., 2006, etc.). Assuming a lithostatic pressure gradient, each 10 MPa pressure step corresponds to instantaneous ascent of ~300 meters. Most MSD experiments designed to study

decompression-induced crystallization utilize time steps longer than 10 hours. Some of the MSD experiments performed by Martel and Schmidt (2003) have step sizes between 1 day and 15 seconds, although these comparatively short experiments do not result in significant crystallization, and are therefore used to study water exsolution and bubble growth.

Timescales of decompression-induced water migration from silicate melts into bubbles occurs much faster than the decompression timescales used in CD experiments (Zhang *et al*., 1991; Zhang & Behrens, 2000). Previous experimental and analytical work (Gardner *et al*., 1999; Martel & Schmidt, 2003) suggests that melt-bubble equilibrium is maintained with respect to H_2O distribution for the decompression rates utilized here. Thus, differences in crystal contents and textures observed in CD experiments at a given pressure result only from factors influencing the kinetics of crystallization, not factors controlling H_2O migration. While the individual pressure steps in MSD experiments are nearly instantaneous and thus significantly faster than rates of H_2O exsolution, the anneal period between pressure steps is sufficient for attainment of melt-bubble equilibrium before the next pressure drop.

Analytical Methods

Chemical compositions were obtained using a Cameca SX-50 electron probe microanalyzer (EPMA) at University of Hawaii Manoa and a Cameca SX-100 EPMA at the University of Oregon. Glass compositions were analyzed using a 15 kV accelerating voltage, 10 nA beam current, and defocused spot size of 5-20 μm (Table 2.3). Sodium and potassium were measured first to minimize loss due to volatilization, and were

extrapolated back to initial (time=0) values using the online correction scheme of Nielsen & Sigurdsson (1981). A suite of synthetic hydrated glasses provided by MJ Rutherford (described in Devine *et al*., 1995) were used as bench standards (e.g., Hammer & Rutherford, 2002) to derive nominal correction factors to account for alkali loss in the hydrous glasses (Devine *et al*., 1995; Morgan & London, 1996). Crystalline phases were analyzed similarly, except using a focused beam. Microlite crystals were not detectably zoned with respect to back-scattered electron (BSE) generation, and small size precluded multiple analyses per grain. Therefore all reported compositions were obtained using a focused beam on the crystal centers. Many charges contained crystals too small to analyze quantitatively, and thus the reported analyses are biased toward crystals larger than ~5 microns. Transect analyses were performed on several suitably-sized crystals, yielding compositional variation smaller than the intra-grain variation within the same sample. The raw data were corrected using ZAF-PAP procedures (e.g., Reed, 1993). Chemical compositions reported in Table 2.3 are averages of 5-12 analyses from each sample.

Back-scatter electron (BSE) images were collected with a JEOL-5900LV scanning electron microscope (SEM) at University of Hawaii Manoa using an acceleration voltage of 15 kV. Although container-initiated crystallization was not observed, images were acquired away from the sample edges whenever possible. Most quantitative textural measurements utilized images at 750x magnification, however samples containing fewer and/or larger crystals were imaged at 500x and 250x. Between 4 and 15 images from each sample were analyzed, with quantity depending on the homogeneity of the sample and the area density of crystals. Plagioclase microlite number

density [crystals mm^{-2}, N_A] on a vesicle-free basis was obtained using methods described in Hammer *et al*. (1999) using the image processing software package ImageJ. One standard deviation error bars were calculated using the variance between individual images. The area fraction of plagioclase microlites (ϕ_A) on a vesicle-free basis was determined using a method similar to Hammer *et al*. (1999) except a point counting grid was utilized, and error bars were determined using the Van der Plas & Tobi (1965) equation for determining point counting errors ($[(\phi_A\ (\phi_A\text{-}1))/n]^{½}$, where n is the number of points counted). Because the samples contain no discernible fabric, the area fraction of plagioclase microlites (ϕ_A) is assumed equal to the volume fraction (ϕ; DeHoff & Rhines, 1968). Phenocrysts inherited from the starting material are significantly larger (>200 μm) than experimentally produced crystals (≤100 μm), thus exclusion of phenocrysts from textural analyses was straightforward. Only plagioclase crystals formed during experiments were used to determine microlite number density and area fraction. Based on five repeat experiments at different decompression rates and quench pressures, we determined that N_A and ϕ are experimentally reproduceable within the one sigma error associated with the variation between different images of an individual sample. In other words, variation within an individual sample exceeds variation among repeat experiments.

Microlite number density and area fraction measurements were used to calculate the characteristic crystal size, S_N [mm] = $(\phi_A/N_A)^{½}$, and volumetric number density, N_V [mm^{-3}] = N_A/S_N (Cheng & Lemlich, 1983; Blundy & Cashman, 2008). Crystal nucleation rates (I) and growth rates (G) were calculated using

$$I\left[\mathrm{mm^{-3}\,s^{-1}}\right] = \frac{N_V}{t}, \text{ and} \qquad \text{Eq. (1)}$$

$$G\left[\mathrm{mm\,s^{-1}}\right] = \frac{S_N}{t} = \left(\frac{\phi_A}{N_A}\right)^{\frac{1}{2}} \Big/ t \qquad \text{Eq. (2)}$$

respectively, where t is the total amount of time spent below P_i (Hammer & Rutherford, 2002). The nucleation rates thus obtained are time-integrated values, and are lower than would be observed immediately following a nucleation pulse. Similarly, actual instantaneous crystal growth rates are higher than are obtained using Eq. 2, given that linear growth rates are highest for small crystals and thus greatest following a nucleation pulse. We also emphasize that the G values obtained using Eq. 2 are based on the *characteristic* size of a population and do not represent growth rates observed for any individual crystals.

A small amount of plagioclase crystallization (totaling ~1.6 vol. %) occurred within 24 hours at 130 MPa and 880°C, the conditions imposed on all experiments prior to decompression. These "initial dwell" crystals exhibit a limited size range (20-60 μm at 130 MPa, increasing to ≤100 μm at P_f=5 MPa), which makes them distinctly larger than decompression-induced nucleated crystals and smaller than phenocrysts inherited from the starting material (>200 μm; Figure 2.1). Crystal size distribution analyses of these experimental charges (see Chapter 3) confirm the visual size distinction between dwell and decompression-induced crystals. Crystallization during the initial dwell period suggests that either (a) the magma storage conditions prior to the 3430 yBP caldera-forming Aniakchak eruption are not exactly 130 MPa and 880˚C, or (b) the natural magma was initially slightly H_2O-undersaturated, as suggested by Larsen (2006). Because this study does not address the magma ascent history specific to the 3430 yBP

Aniakchak eruption, the mismatch between the magma chamber conditions and the experimental starting conditions is not relevant. Rather, the fact that each experiment was preceded by a dwell period of identical conditions ensures that results are internally consistent. To ensure that our interpretations of decompression-induced crystallization are not affected by the crystals formed at P_i or crystal growth that occurred prior to commencement of decompression, the average microlite number density (N_A) and area fraction (ϕ) of feldspar (72 mm^{-2} and 0.016, respectively) in samples quenched after 24-40 hours at P_i were subtracted from quantitative textural results (Table 2.2).

RESULTS

Mineralogy

Every charge contains plagioclase, orthopyroxene, clinopyroxene, Fe-Ti oxides, and trace amounts of apatite. Alkali feldspar is present only in anneal runs terminated at low pressure (26 and 5 MPa). A silica phase formed in anneal experiments at 5 MPa. Distinctive botryoidal texture, multiple contraction fractures, and preferential formation at the margins of irregular void spaces all suggest cristobalite deposition from a late-stage, silica-rich vapor phase (Hoblitt & Harmon, 1993). No silica phase is present in snapshot experiments at any of the quench pressures in this study, suggesting a delay in nucleation longer than the timescale of the slowest decompression run to 5 MPa. While amphibole should be stable at 880˚C and 109 MPa as determined by Larsen (2006), it was not present as a groundmass phase in the runs at P_f=109 MPa. However, this is not surprising because the starting material only contained trace amounts of amphibole

(Dreher *et al*., 2005) and these conditions are very close to the amphibole stability curve (Larsen, 2006).

At each quench pressure, all slowly decompressed samples (≤1 MPa h^{-1}) contain microlites that formed during decompression, in addition to initial dwell crystals. In the two fastest decompression series (10 and 2 MPa h^{-1}), microlites resulting from decompression-induced nucleation are not visible until ≤68 MPa (Figure 2.2c-d). A nucleation delay following exposure of a melt to conditions of crystal supersaturation is commonly observed in silicate systems (James, 1974, 1985; Fokin *et al*., 1981), and attributed to the time necessary for structural reorganization of the melt and establishment of subcritical clusters. The lack of decompression-induced nucleation in rapidly decompressed (≥2 MPa h^{-1}) rhyodacite quenched at ≥87 MPa suggests a feldspar nucleation delay on the order of ~4.5-6 hours for the 10 MPa h^{-1} decompression rate and ~11-22 hours for 2 MPa h^{-1}. The presence of decompression crystals in every slowly decompressed sample constrains plagioclase nucleation delays of <22 hours in the 1 MPa h^{-1} series and <49 hours in the 0.5 MPa h^{-1} series (Table 2.2).

Crystal Morphology

Fe-Ti oxide crystals are typically equant, euhedral, small (<5 μm), and evenly distributed throughout the sample. Although Fe-Ti oxide crystals range up to 20 μm in some samples, there is no systematic correlation between oxide size and decompression rate or quench pressure. Pyroxene crystals are generally euhedral, with the exception being hopper and elongate (40-60 μm) skeletal crystals in runs decompressed >0.5 MPa h^{-1} and annealed at 5 MPa, and those annealed at 26 MPa following decompression at 10 MPa h^{-}

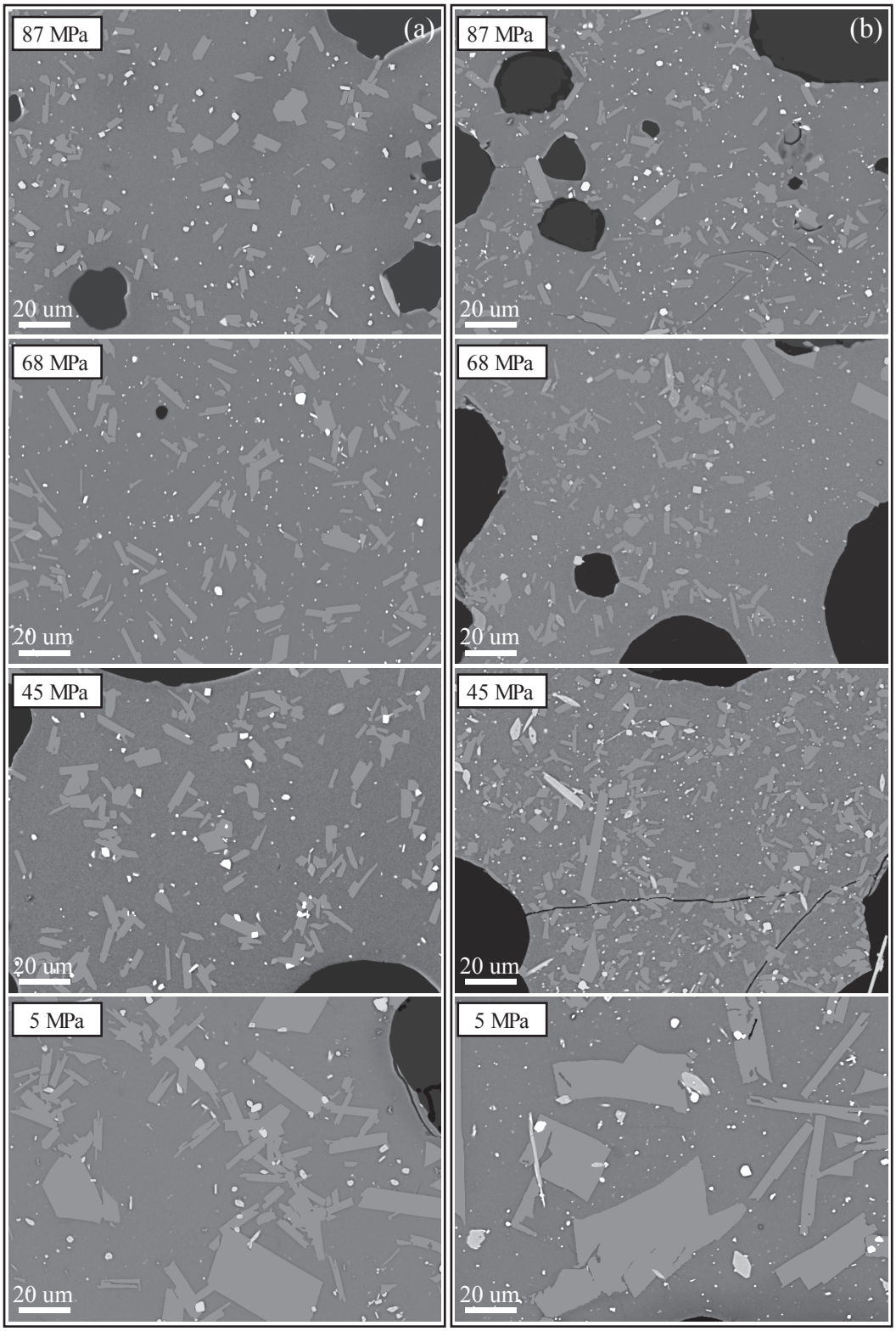

Fig. 2.2. Backscatter electron images of textures found in snapshot samples: (a) 0.5 MPa h^{-1}; (b) 1 MPa h^{-1}; (c) 2 MPa h^{-1}; and (d) 10 MPa h^{-1}. Feldspar crystals (medium gray) have been manually colored a lighter shade of gray to make viewing easier. Black areas are void space, white grains are Fe-Ti oxides, and light gray crystals are pyroxene or occasionally apatite. The different scale for the 87 MPa runs in (c) and (d) should be noted; all crystals in these two runs are inherited from the initial dwell period. (continued)

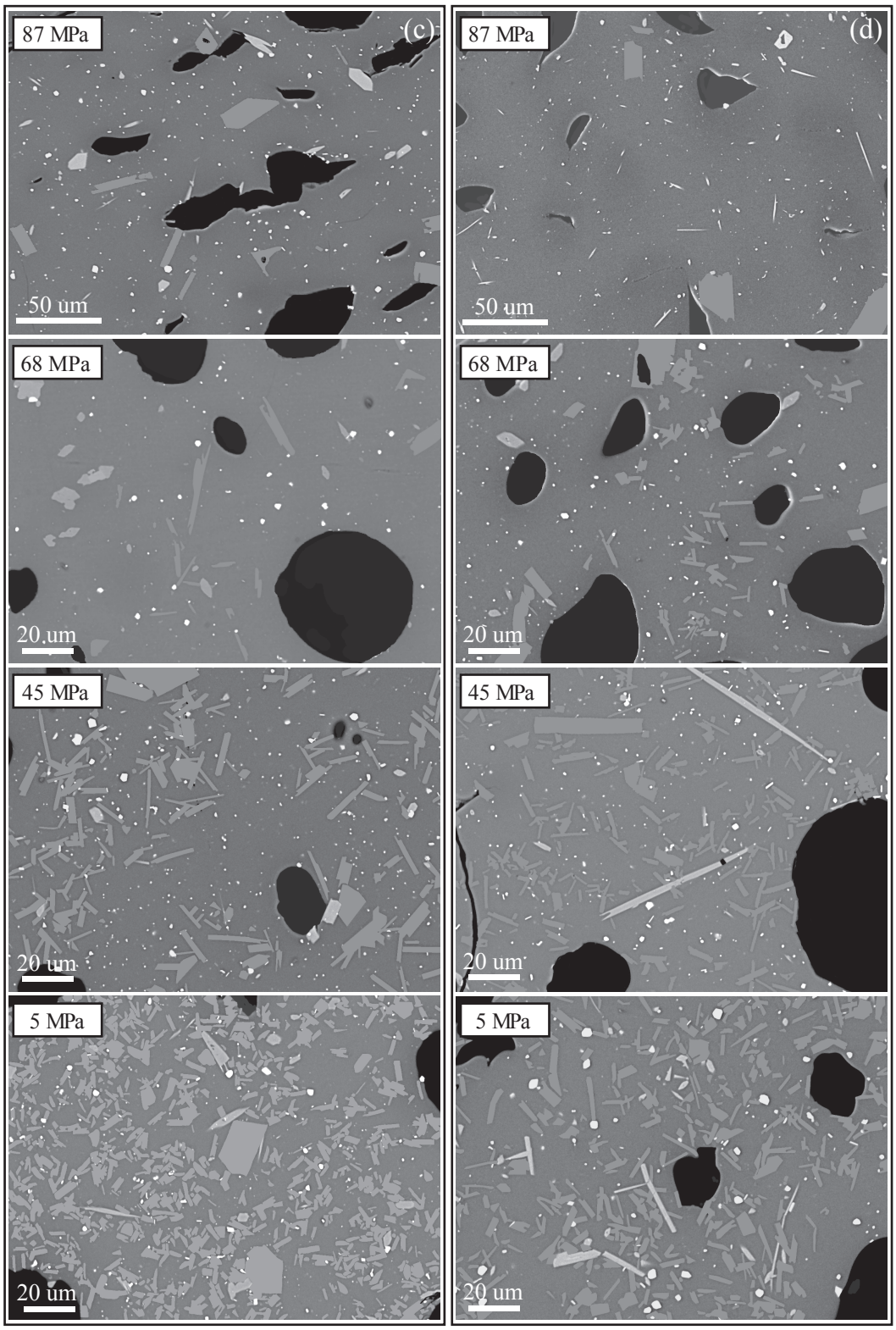

Fig. 2.2. Continued.

[1]. Pyroxene crystals are generally <20 μm in length and <10 μm in width, as ascertained from BSE images. However, some samples contain crystals of similar width ranging up to 60 μm in length. Pyroxene crystal length is uncorrelated with decompression rate or quench pressure, suggesting that high aspect ratio crystals are simply slices through highly flattened tabular morphologies (Peterson, 1996).

Feldspar crystallization is extremely sensitive to changes in P_{H2O} and effective undercooling; consequently, feldspar textures vary coherently with respect to the experimental variables of decompression rate and quench pressure (Figure 2.2, Appendix 2.A). Qualitative inspection of samples at each quench pressure indicate that feldspar morphologies (excluding initial dwell crystals) display progressively more disequilibrium features as decompression rate increases. Slowly decompressed samples contain predominantly tabular and euhedral plagioclase crystals during almost the entire decompression history, with a small fraction of swallowtail morphologies present in only the lowest pressure sample (Figure 2.2a). As decompression rate increases, swallowtail and high aspect ratio crystals become more prevalent and they begin appearing at progressively higher quench pressures (Figure 2.2b-d). Crystal populations also display distinct trends attributable to decompression rate. At the highest pressures examined, fast decompression leads to growth of initial dwell crystals and the absence of nucleation, resulting in few large crystals; slow decompression is characterized by early nucleation as well as growth, which results in a crystal population dominated by small microlites (Figure 2.2, top row). By the time low pressures are reached, rapid decompression causes substantial nucleation, which results in a large number of small crystals. Slowly

decompressed samples ultimately contain fewer and larger crystals as a consequence of growth-dominated crystallization (Figure 2.2, bottom row).

Crystals in anneal runs are typically larger than crystals in snapshot runs at the same decompression rate and quench pressure (Figure 2.3). However, the textures of anneal samples quenched at the same P_f are not homogeneous. Anhedral morphologies and disequilibrium textures are commonly found in samples quenched at low pressures and with faster initial decompression rates (Figure 2.3). The textural variation between samples 17-3 and 6-2, both decompressed at 10 MPa h^{-1} to P_f=5 MPa, suggests that the length of the anneal segment is crucial to the textural development of the crystals. Although the volume of plagioclase in these samples is identical, the sample with longer anneal time (sample 17-3; 1302 h) contains euhedral crystals whereas the shorter duration experiment (sample 6-2; 342 h) contains crystals with disequilibrium textures (swallowtail and hopper crystals).

Skeletal and hopper morphologies are common in the multi-step decompression experiments, while comparable continuous decompression experiments contain dominantly faceted crystals (Figure 2.4). Another interesting textural difference between CD and MSD samples is inhomogeneous distribution of plagioclase crystals in the MSD runs. Crystal-free pockets are interspersed with areas containing a high density of contiguous or clumped crystals. These grains may touch outside the plane of the thin section.

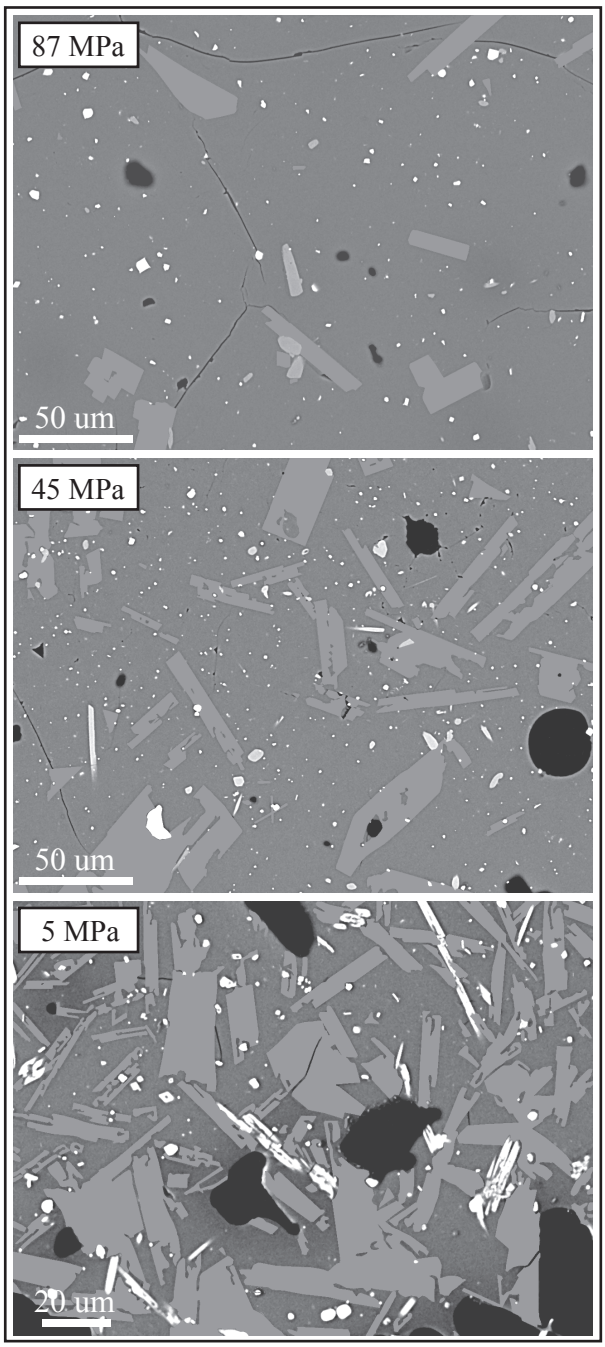

Fig. 2.3. Textural examples of anneal runs at 87, 45, and 5 MPa. The samples shown were decompressed at 2 MPa h^{-1}, and annealed for 285, 94, and 588 hours, respectively. Textural examples of snapshot runs from the same decompression series are shown in Fig. 2.2c. Feldspar crystals (medium gray) have been manually colored to make viewing easier. Black areas are void space, white grains are Fe-Ti oxides, and light gray crystals are pyroxene.

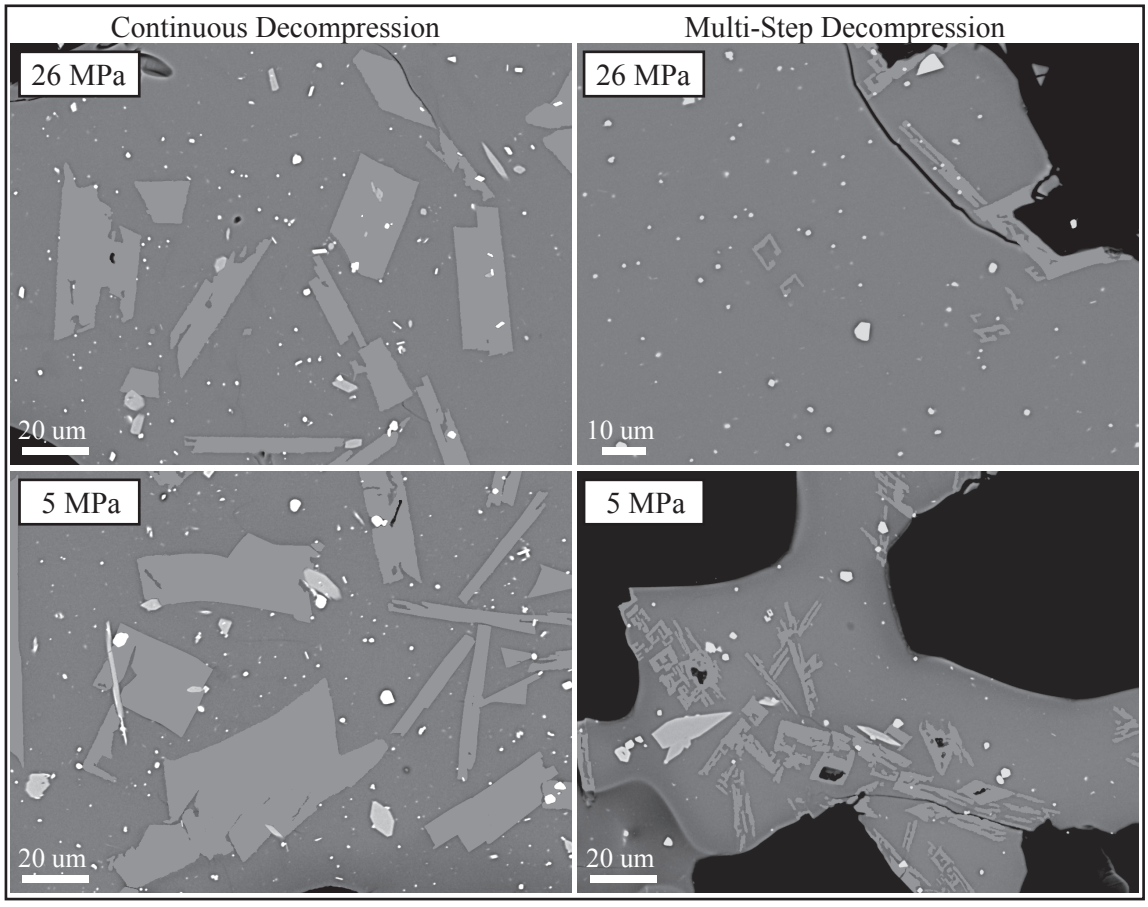

Fig. 2.4. Textural comparisons between continuous decompression and multi-step decompression experiments, both at an integrated decompression rate of 1 MPa h^{-1}. Feldspar crystals (medium gray) have been manually colored to make viewing easier. Other phases include pyroxene (light gray) and Fe-Ti oxides (white). Black areas are void space.

Phase Compositions

Glass

Anneal experiments performed at different decompression rates and for various anneal durations produce comparable matrix glass compositions and similar volumes of plagioclase at each quench pressure with no apparent relationship to decompression rate or anneal duration (Tables 2.2 and 2.3). This time-invariance suggests that the anneal runs achieved chemical steady-state, and thus are interpreted as achieving equilibrium plagioclase compositions, crystallinities, and glass compositions. Matrix glasses of anneal experiments thus record the equilibrium liquid line of descent during isothermal crystallization at varying P_{H2O}. With the exception of alkali feldspar (which only forms in low-pressure anneal runs), potassium is essentially incompatible in the crystallizing assemblage. Thus the K_2O content of snapshot glasses increases with total crystallinity (Figure 2.5). Similarly, as plagioclase is the only crystallizing phase rich in aluminum, progressive decline in glass Al_2O_3 isolates the plagioclase contribution to the crystallizing assemblage (Figure 2.5).

The K_2O contents of matrix glass in snapshot experiments reveal the extent of crystallization driven by continuous and multi-step decompression, with the K_2O contents of anneal experiments providing equilibrium values for comparison. At 109 MPa, each snapshot run contains glass with nearly the same K_2O content as the interpolated anneal run using bracketing experiments at 130 and 87 MPa. This indicates that the extent of crystallization at pressures ≥109 MPa is not only equivalent regardless of decompression rate in the investigated range, but also that crystallization occurs sufficiently rapidly to maintain chemical equilibrium (Figure 2.5). Upon further decompression, the snapshot

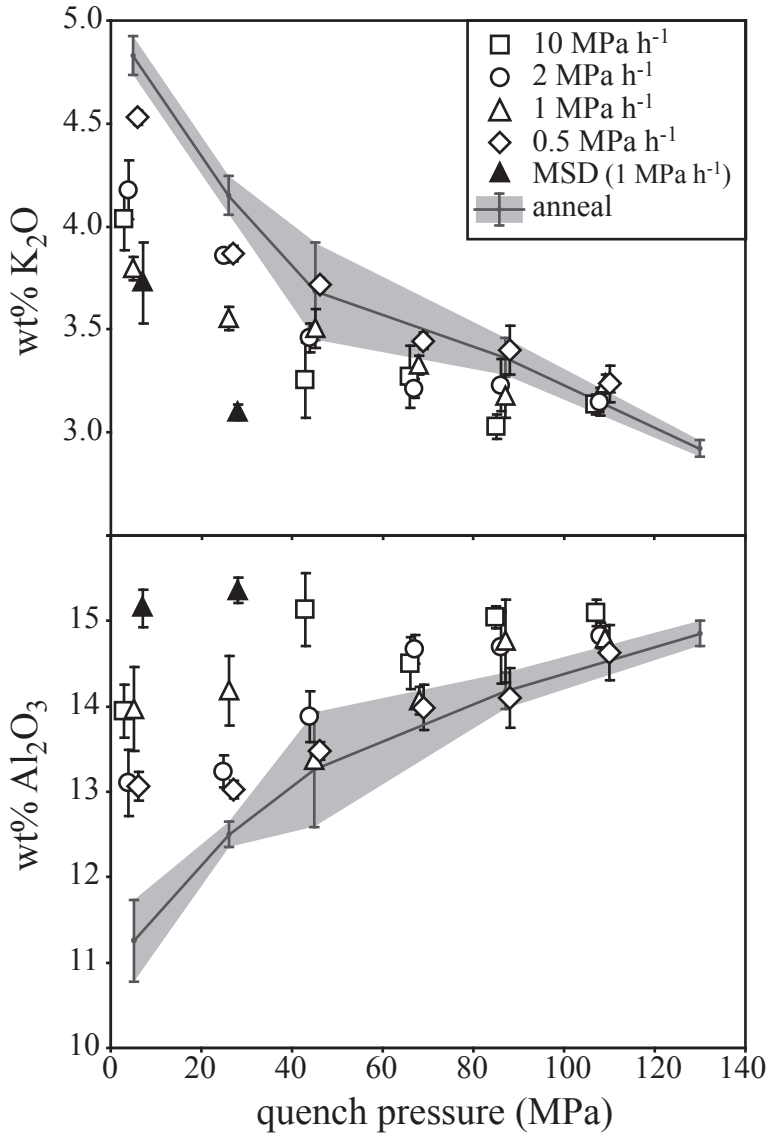

Fig. 2.5. Variation of glass compositions in MSD samples and CD snapshot samples compared to anneal samples. Each point is an average of 5-12 microprobe analyses and error bars represent 1σ variation. The anneal curve was created by averaging all the anneal runs at the given quench pressure and the shading around the curve represents this variation between anneal experiments at the same pressure. Each decompression series is offset slightly on the x-axis for clarity.

runs systematically depart from the equilibrium K_2O- P_f trend. Across all P_f's, snapshot runs performed at the lowest decompression rate have compositions that most closely approach equilibrium, although the high Al_2O_3 contents of the slowest-decompressed samples suggest disproportionate contributions from pyroxene and other nominally Al-free phases to the total crystallinity. Conversely, high decompression rate and MSD produce glasses that are markedly low in K_2O, indicating insufficient crystallization relative to equilibrium. Because the anneal runs at the lowest pressures (5 and 26 MPa) contain alkali feldspar containing up to 4 wt% K_2O, the potassium contents of the glasses in these runs are lower than would be the case if potassium behaved incompatibly. Thus the alkali feldspar-free snapshot runs are even further from the equilibrium crystal content than is suggested by their glass K_2O contents.

Plagioclase

Plagioclase compositions vary widely among the 4-15 crystals analyzed in each run (Figure 2.6, Table 2.4, Appendix 2.B), and there is no clear relationship between crystal size and composition. The compositions in snapshot experiments vary by approximately 10-15 mol% An at each P_f, and there appears to be no relationship between decompression rate and plagioclase composition (Figure 2.6a-b). Anneal experiments display variation over a similarly wide range, although the 5 MPa samples contain some crystals with more Ab- and Or-rich compositions (Figure 2.6c). The most An-rich crystals in all snapshot and anneal runs have similar compositions (An_{39}-An_{43}), regardless of decompression rate or quench pressure. In anneal samples, the compositions of the most alkalic crystals vary coherently with P_f. Samples quenched at 87 and 45 MPa

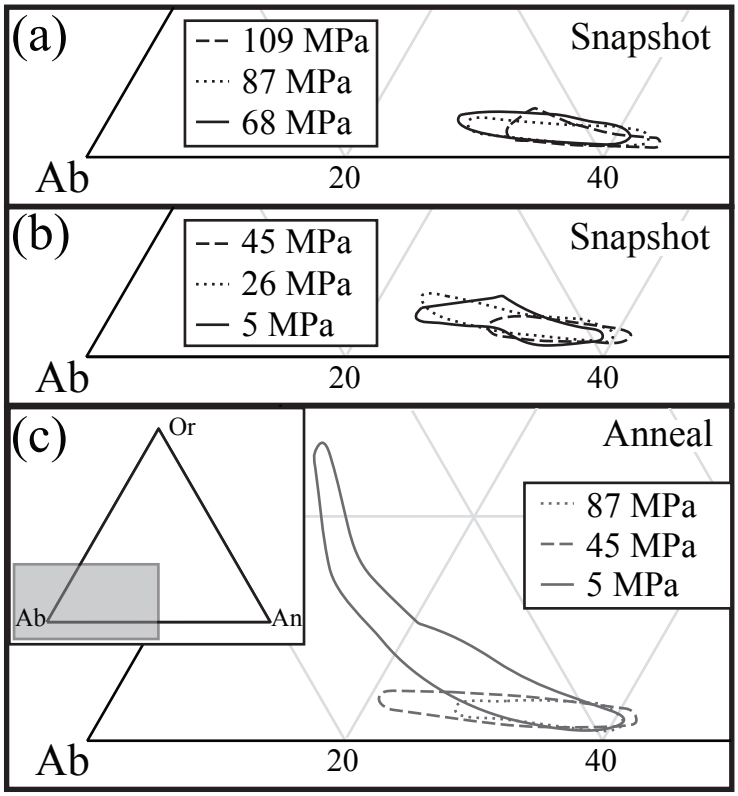

Fig.2.6. Feldspar microlite compositions are plotted in the Anorthite-Albite-Orthoclase (An-Ab-Or) ternary diagram. For clarity, plots are separated into three groups: (a) high pressure snapshot; (b) low pressure snapshot; (c) anneal samples. Each field represents a different quench pressure, with no distinction made between different decompression rates. The plot area in (c) is represented by the shaded region in the inset.

Table 2.4. Select analyses of crystalline phases

sample	phase[a]	SiO_2	TiO_2	Al_2O_3	FeO[b]	Fe_2O_3	MnO	MgO	CaO	Na_2O	K_2O	An	Ab	Or	Kd
5-1	plag	63.0	nd	22.9	nd		nd	nd	4.4	8.7	0.7	21.2	75.0	3.9	2.7
5-2	opx	53.3	0.2	0.6	20.1		1.8	22.4	1.3	0.0	0.0				
5-2	Na-pyx	46.1	2.1	9.3	13.9		0.8	14.1	9.7	2.1	0.4				
5-2	plag	60.4	nd	24.7	nd		nd	nd	6.5	7.1	0.4	32.7	65.1	2.2	4.6
5-4	opx	53.1	0.2	1.0	19.8		1.8	21.9	2.1	0.0	0.0				
5-4	cpx	51.7	0.6	2.2	12.3		1.3	14.2	16.8	0.4	0.1				
5-4	plag	60.4	nd	24.6	nd		nd	nd	6.7	6.7	0.3	34.8	63.1	2.1	3.5
6-1	opx	52.7	0.3	0.9	19.5		1.9	21.8	1.8	0.0	0.0				
6-1	cpx	52.3	0.3	1.2	9.9		0.9	14.1	20.0	0.3	0.0				
6-1	plag	60.2	nd	25.0	nd		nd	nd	6.7	7.4	0.3	32.7	65.4	1.9	7.3
6-2	opx	52.9	0.3	1.0	19.4		1.9	22.0	2.5	0.0	0.0				
6-2	plag	59.5	nd	25.1	nd		nd	nd	7.1	7.3	0.3	34.2	63.8	2.0	18.3
7-1	plag	59.2	nd	25.2	nd		nd	nd	6.9	7.5	0.4	32.8	65.0	2.1	4.1
7-2	opx	53.8	0.2	0.7	18.8		1.7	24.2	1.2	0.0	0.0				
7-2	Na-pyx	45.9	2.1	9.2	10.4		0.8	15.8	10.8	2.2	0.4				
7-2	cpx	50.0	1.1	3.6	11.1		0.9	13.0	19.7	0.4	0.0				
7-2	plag	58.9	nd	25.6	nd		nd	nd	7.2	7.1	0.3	35.2	62.8	2.0	5.5
7-4	opx	53.0	0.3	0.8	19.3		2.1	23.1	1.5	0.0	0.0				
7-4	Na-pyx	46.8	1.8	8.5	11.3		0.8	15.7	10.6	2.0	0.4				
7-4	cpx	52.1	0.4	1.6	10.0		0.9	14.4	20.1	0.3	0.0				
7-4	plag	59.8	nd	24.6	nd		nd	nd	6.6	7.3	0.5	32.5	64.8	2.8	4.8
8-1	Na-pyx	45.9	1.8	9.5	9.8		0.8	16.5	10.9	2.2	0.4				
8-1	cpx	52.5	0.3	1.2	8.5		1.1	14.7	20.3	0.4	0.0				
8-1	plag	60.3	nd	24.7	nd		nd	nd	6.3	7.7	0.4	30.4	67.2	2.3	7.0
8-3	opx	54.1	0.3	0.7	16.1		3.3	24.4	1.3	0.0	0.0				
8-3	plag	60.0	nd	24.2	nd		nd	nd	6.3	7.6	0.5	30.4	66.7	2.9	7.0
11-1	mgt	0.1	9.4	1.9	37.2	47.9	1.3	0.8	0.0	0.0	0.0				
11-1	ilm	0.1	42.6	0.2	33.4	16.2	2.0	1.6	0.1	0.0	0.0				
11-1	opx	53.5	0.3	0.5	19.5		1.9	22.0	1.3	0.0	0.0				
11-1	plag	66.6	nd	19.7	nd		nd	nd	3.0	7.4	2.0	15.9	71.3	12.8	5.9
12-1	plag	59.6	nd	25.4	nd		nd	nd	6.8	7.7	0.4	32.3	65.7	2.0	3.1
12-2	plag	58.4	nd	23.7	nd		nd	nd	6.1	7.1	0.5	31.3	65.9	2.8	3.7
12-3	mgt	0.1	11.5	2.2	37.9	44.7	1.2	1.9	0.0	0.0	0.0				
12-3	Na-pyx	45.6	2.5	8.5	12.9		0.6	13.3	10.9	2.3	0.5				
12-3	cpx	52.4	0.7	2.3	10.9		1.1	14.0	17.4	0.5	0.1				
12-3	opx	52.6	0.3	1.3	19.8		1.9	21.8	2.1	0.0	0.0				
12-3	plag	58.7	0.1	24.7	0.5		0.0	0.0	6.9	7.4	0.4	33.3	64.5	2.2	3.2
13-1	opx	54.9	0.2	0.7	15.3		2.9	25.1	0.9	0.0	0.0				
13-1	plag	62.2	0.0	22.3	0.4		0.0	0.0	4.7	7.9	0.8	23.7	71.3	5.0	6.8
13-2	opx	53.5	0.2	0.7	20.3		1.8	21.9	1.4	0.0	0.1				
13-2	plag	62.3	nd	22.6	nd		nd	nd	4.3	8.2	1.7	20.3	70.2	9.5	8.0
13-3	opx	52.6	0.3	0.9	20.0		1.9	21.9	1.7	0.0	0.0				
13-3	plag	61.0	nd	23.6	nd		nd	nd	5.7	7.7	0.6	28.1	68.3	3.7	10.8

[a] phases: plag=most Ab-rich plagioclase analyzed, opx=orthopyroxene, cpx=clinopyroxene, Na-pyx=sodium-rich pyroxene, ilm=ilmenite, mgt=magnetite.

[b] iron is listed as total iron except in ilm and mgt where it was converted into a combination of FeO and Fe_2O_3 using ILMAT (Lepage, 2002).

Table 2.4. (continued) Select analyses of crystalline phases

sample	phase[a]	SiO_2	TiO_2	Al_2O_3	FeO[b]	Fe_2O_3	MnO	MgO	CaO	Na_2O	K_2O	An	Ab	Or	Kd
14-1	opx	53.0	0.2	0.6	20.2		1.9	22.4	1.4	0.0	0.0				
14-1	cpx	51.0	0.5	2.4	11.9		1.2	14.3	17.1	0.4	0.0				
14-1	plag	60.0	nd	24.8	nd		nd	nd	6.5	7.5	0.4	31.6	65.9	2.4	3.4
14-2	opx	52.9	0.3	1.0	19.0		1.9	23.2	1.5	0.0	0.0				
14-2	Na-pyx	46.7	1.8	9.2	10.4		0.7	15.5	10.7	2.1	0.4				
14-2	cpx	51.3	0.6	2.0	13.8		0.4	14.4	17.0	0.3	0.0				
14-2	plag	60.0	nd	24.3	nd		nd	nd	6.2	7.6	0.4	30.1	67.4	2.5	3.3
15-1	plag	61.6	nd	23.9	nd		nd	nd	5.8	7.7	0.5	28.6	68.7	2.7	2.8
15-2	Na-pyx	47.1	1.8	8.1	11.8		1.0	15.9	9.9	2.0	0.4				
15-2	plag	59.3	nd	24.4	nd		nd	nd	6.4	7.4	0.4	31.5	66.0	2.5	7.1
15-3	mgt	0.2	6.7	2.3	31.7	54.0	1.9	2.6	0.0	0.0	0.0				
15-3	cpx	50.9	0.9	2.8	13.3		0.5	15.2	15.2	0.3	0.0				
15-3	opx	52.5	0.9	4.6	13.8		1.9	20.5	3.8	0.6	0.3				
15-3	Na-pyx	45.1	2.0	9.9	11.6		0.6	15.0	10.6	2.2	0.5				
15-3	plag	64.6	nd	23.6	nd		nd	nd	5.3	7.9	0.6	26.2	70.4	3.5	3.9
15-4	Na-pyx	46.1	2.1	9.2	11.5		0.7	15.2	10.4	2.2	0.4				
15-4	cpx	53.0	0.3	2.2	10.1		1.3	15.0	17.5	0.4	0.1				
15-4	plag	62.5	nd	23.1	nd		nd	nd	5.0	8.3	0.6	24.2	72.4	3.3	3.5
15-5	plag	60.7	nd	25.0	nd		nd	nd	6.5	7.4	0.4	31.9	65.5	2.6	3.6
15-6	opx	53.1	0.2	1.2	17.2		3.4	23.5	0.9	0.0	0.0				
15-6	plag	60.4	nd	24.7	nd		nd	nd	6.7	7.6	0.5	31.8	65.5	2.7	6.2
15-7	opx	53.7	0.2	0.6	19.7		1.9	23.0	1.2	0.0	0.0				
15-7	Na-pyx	47.5	2.3	9.9	12.0		0.7	14.0	9.3	2.5	0.7				
15-7	plag	64.7	nd	20.8	nd		nd	nd	2.4	7.9	2.4	12.4	72.7	14.8	4.5
16-1	Na-pyx	47.7	1.6	8.9	9.9		0.8	15.5	10.9	2.3	0.5				
16-1	cpx	52.1	0.7	2.7	10.2		1.1	14.1	18.0	0.6	0.1				
16-1	plag	60.1	nd	25.1	nd		nd	nd	6.7	7.4	0.4	32.6	65.2	2.2	3.4
16-2	mgt	0.1	8.4	1.9	33.8	51.3	1.7	2.4	0.0	0.0	0.0				
16-2	ilm	0.1	44.9	0.2	30.2	16.5	2.5	4.3	0.0	0.0	0.0				
16-2	opx	54.5	0.2	0.7	18.7		2.0	22.8	1.3	0.0	0.0				
16-2	Na-pyx	45.8	2.4	8.7	10.4		0.7	15.4	10.7	2.2	0.4				
16-2	plag	61.4	nd	24.3	nd		nd	nd	5.8	7.6	0.5	28.9	67.9	3.2	4.1
17-1	plag	58.5	0.0	24.9	0.5		0.0	0.0	7.0	7.2	0.4	34.2	63.7	2.1	18.3
18-1	mgt	0.1	6.4	2.1	32.1	54.5	1.5	2.4	0.0	0.0	0.0				
18-1	opx	54.0	0.2	0.5	19.2		1.8	22.1	1.7	0.0	0.0				
18-1	Na-pyx	46.0	2.6	9.0	11.0		0.7	15.1	10.6	2.2	0.5				
18-1	cpx	52.1	0.8	2.6	9.8		1.0	14.1	19.0	0.4	0.0				
18-1	plag	59.7	0.0	23.8	0.6		0.0	0.0	5.7	7.8	0.5	27.7	69.2	3.0	2.9
18-2	plag	56.9	nd	24.0	nd		nd	nd	6.1	7.3	0.4	30.6	66.8	2.6	5.7
18-3	plag	60.6	nd	24.0	nd		nd	nd	6.2	7.4	0.6	30.6	66.1	3.3	11.2
18-4	plag	60.4	nd	24.4	nd		nd	nd	6.2	7.5	0.5	30.4	67.0	2.6	3.6
18-5	plag	60.2	nd	23.4	nd		nd	nd	5.2	7.9	0.5	25.9	70.9	3.2	3.3
20-1	plag	58.5	nd	23.5	nd		nd	nd	5.5	7.6	0.4	27.9	69.4	2.7	3.7

[a] phases: plag=most Ab-rich plagioclase analyzed, opx=orthopyroxene, cpx=clinopyroxene, Na-pyx=sodium-rich pyroxene, ilm=ilmenite, mgt=magnetite.

[b] iron is listed as total iron except in ilm and mgt where it was converted into a combination of FeO and Fe_2O_3 using ILMAT (Lepage, 2002).

Table 2.4. (continued) Select analyses of crystalline phases

sample	phase[a]	SiO_2	TiO_2	Al_2O_3	FeO[b]	Fe_2O_3	MnO	MgO	CaO	Na_2O	K_2O	An	Ab	Or	Kd
20-2	plag	60.8	nd	24.8	nd		nd	nd	6.6	7.1	0.5	32.7	64.5	2.8	3.6
20-3	plag	63.4	nd	22.1	nd		nd	nd	3.8	8.5	1.1	18.5	75.1	6.4	3.8
21-1	plag	59.5	nd	24.7	nd		nd	nd	6.3	7.2	0.4	32.0	65.8	2.2	4.8
22-1	opx	53.1	0.3	0.6	20.2		1.9	21.6	1.4	0.0	0.0				
22-1	cpx	49.9	1.0	3.8	8.4		1.1	13.9	20.2	0.6	0.0				
22-1	plag	59.6	0.1	23.0	0.6		0.0	0.0	5.6	7.8	0.5	27.6	69.4	2.9	2.1
22-2	mgt	0.3	9.6	3.5	35.3	44.8	1.1	2.3	0.0	0.0	0.1				
22-2	opx	53.3	0.2	1.1	15.9		1.9	23.3	2.5	0.0	0.0				
22-2	cpx	49.0	1.1	4.4	9.9		1.2	13.1	19.0	0.5	0.1				
22-2	plag	62.4	0.0	22.2	0.5		0.0	0.1	4.7	8.2	0.6	23.1	73.5	3.4	2.3
BJ3	plag	59.4	nd	23.1	nd		nd	nd	5.4	7.3	0.7	27.6	67.9	4.5	7.1

[a] phases: plag=most Ab-rich plagioclase analyzed, opx=orthopyroxene, cpx=clinopyroxene, Na-pyx=sodium-rich pyroxene, ilm=ilmenite, mgt=magnetite.

[b] iron is listed as total iron except in ilm and mgt where it was converted into a combination of FeO and Fe_2O_3 using ILMAT (Lepage, 2002).

contain crystals with $Or_{\leq 3.9}$, and anorthite contents of ≥27.9 and ≥21.1, respectively. In contrast, crystals in P_f=5 MPa samples are $An_{\geq 5.6}$ and up to $Or_{25.5}$.

Plagioclase Volume Fraction and Microlite Number Density

Plagioclase volume fractions (ϕ) in anneal experiments are consistent with the K_2O trends described above, they exhibit an accelerating increase in crystallinity with decreasing P_f (Table 2.2 and Figure 2.7a). As with the compositional data, ϕ values for anneal samples provide a means of evaluating the extent to which snapshot crystallinities approach equilibrium. Snapshot ϕ values are surprisingly uncorrelated with decompression rate, having nearly uniform feldspar contents for each P_f and very few outliers.

At the highest pressures, ϕ values in snapshot experiments are within 2σ of the anneal values. However, starting at ~ 45 MPa, the snapshot ϕ values progressively fall below the anneal values. By 5 MPa, the snapshot runs contain approximately half the amount of plagioclase present in anneal samples. Thus, the volume fraction of plagioclase obtained by image analysis is consistent with glass composition data, which reveal progressive departure from equilibrium with decreasing P_f.

At each of the pressures examined, multi-step decompression produces significantly less plagioclase than continuous decompression (Figure 2.7a). By 26 MPa the MSD sample crystallized less than 2% plagioclase, approximately equivalent to the CD sample at 87-109 MPa, and by 5 MPa it contains only 16% plagioclase, which was present in the CD experiment by 45 MPa. This is consistent with previous studies that recognize groundmass crystallinities in near-fully decompressed MSD samples to be

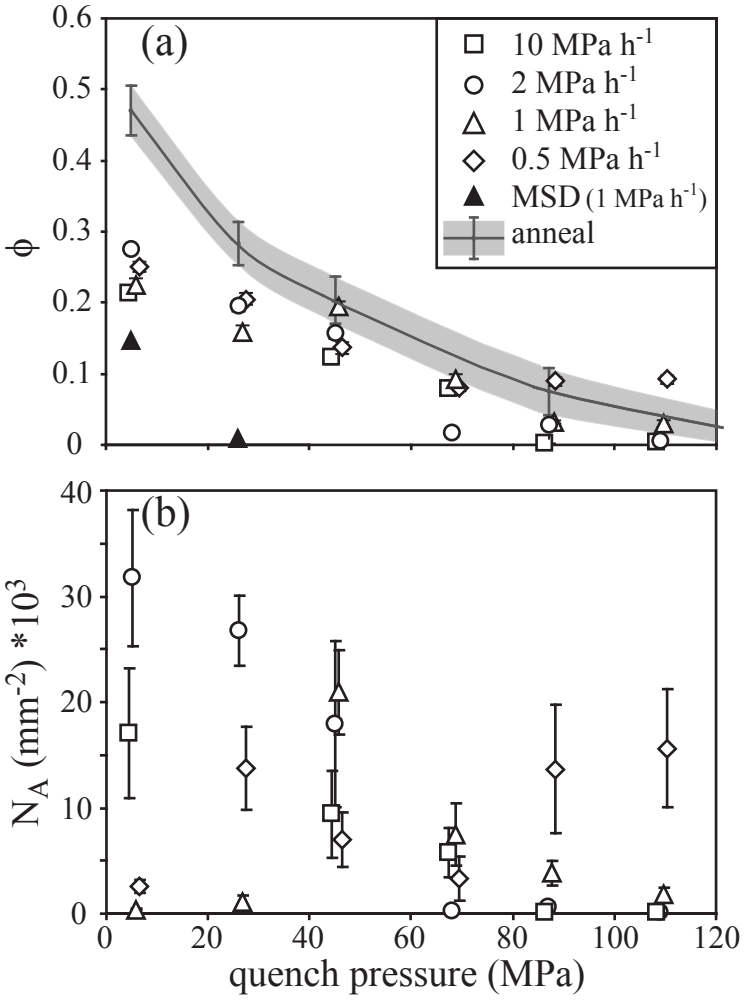

Fig. 2.7. (a) Volume fraction of plagioclase (ϕ) in each run as a function of decompression rate and quench pressure. The anneal curve was created by averaging all the anneal runs at the given quench pressure and the shading represents the 1σ error of this variation. The 1σ error bars are calculated using the equation of Van der Plas & Tobi (1965) for estimation of point counting errors. Where error bars are not visible they are smaller than the symbol. (b) The number density of plagioclase microlites (N_A) in each sample as a function of decompression rate and quench pressure. The error bars are 1σ values representing variation between BSE images. Each decompression series is offset slightly on the x-axis for clarity.

several vol% lower than in natural samples (Hammer & Rutherford, 2002; Couch *et al.*, 2003b; Cashman & McConnell, 2005).

In contrast to ϕ, microlite number density (N_A) varies appreciably as a function of decompression rate among CD snapshot samples (Figure 2.7b). At the two fastest decompression rates, N_A remains fairly low until ≤50 MPa, then peaks at 5 MPa. At an intermediate decompression rate of 1 MPa h^{-1}, N_A increases to a peak at 45 MPa, and then declines. There is no obvious number density peak at the slowest decompression rate. Rather, moderately high N_A is achieved at relatively high pressure (by 109 MPa) and subsequent snapshots in this series have similar or lower N_A values.

Textural differences among the products of high-intensity and low-intensity volcanic eruptions are manifested in the relative magnitudes of N_A and ϕ (Figure 2.8), textural parameters that therefore facilitate quantitative comparisons of experimental products and natural volcanic rocks. The 1991 pre-climactic subplinian eruptions of Mt. Pinatubo and 1980 post-climactic subplinian eruptions of Mount St Helens produced pyroclasts with high number densities but low total volume fraction (Hammer *et al.*, 1999; Cashman & McConnell, 2005). In contrast, the effusive 1986-1995 dome-building eruptions of Merapi, 1991-1995 block-and-ash flows of Mt. Unzen, 1997 vulcanian explosions at Soufriere Hills, and 1859 lava flows from Mauna Loa Volcano generated samples with low N_A values but high plagioclase volume fractions (Hammer *et al.*, 2000; Clarke *et al.*, 2007; Noguchi *et al.*, 2008; Riker *et al.* 2009). The experimental samples of this study plot within the range of effusive and low-intensity explosive eruptions, as befitting the decompression rates utilized. The coincidence of N_A/ϕ between synthetic

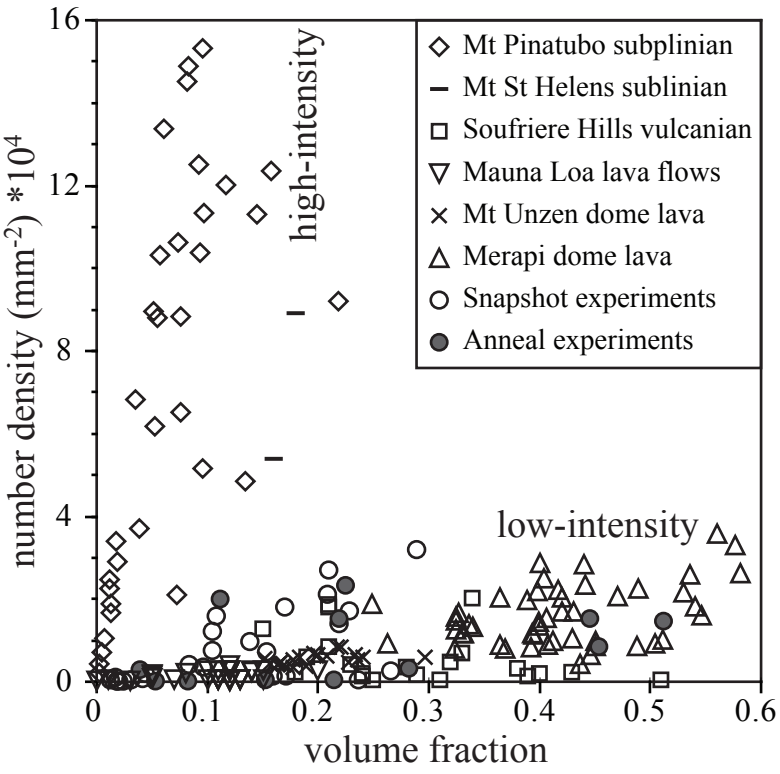

Fig 2.8. Textural differences between high-intensity and low-intensity eruptions are displayed on a plot of number density (N_A) vs plagioclase volume fraction (ϕ). Data sources: Pinatubo, Hammer *et al*. (1999); Merapi, Hammer *et al*. (2000); Mount St. Helens, Cashman & McConnell (2005); Soufriere Hills, Clarke *et al*. (2007); Mt Unzen, Noguchi *et al*. (2008); Mauna Loa, Riker *et al*. (2009).

and natural samples supports the underlying premise of our study—that the texture-controlling processes of crystallization are reproduced in a laboratory environment.

Nucleation and Growth Rates

As expected from the above trends in ϕ and N_A, plagioclase nucleation (I) and growth rates (G) in snapshot experiments vary with decompression rate and quench pressure. Closely reflecting variations in N_A with decompression rate, time-integrated nucleation rates peak at different pressures for each series (Figure 2.9). The pressure of the maximum nucleation rate decreases as the decompression rate increases. Nucleation rate maxima occur at 5, 26, 45, and 109 MPa, respectively, as decompression rate decreases from 10 to 0.5 MPa h^{-1}.

Average plagioclase growth rates in snapshot samples range from 10^{-6} to 10^{-9} mm s^{-1} (Figure 2.10), which is the same range found in previous MSD experiments utilizing intermediate to silicic magmas (Hammer & Rutherford, 2002; Couch *et al*., 2003b). However, each decompression rate is associated with a unique range of G, and the magnitude of internal variation is markedly different for each decompression rate. The slowest decompression series produces G values spanning less than one order of magnitude, while G values from the fastest decompressions vary by more than two orders of magnitude. In the two fastest decompression series, maximum G occurs at the highest pressure (109 MPa) and then steadily decreases with decreasing P_f. In contrast, crystal growth rates in the two slower decompression series remain fairly constant throughout decompression.

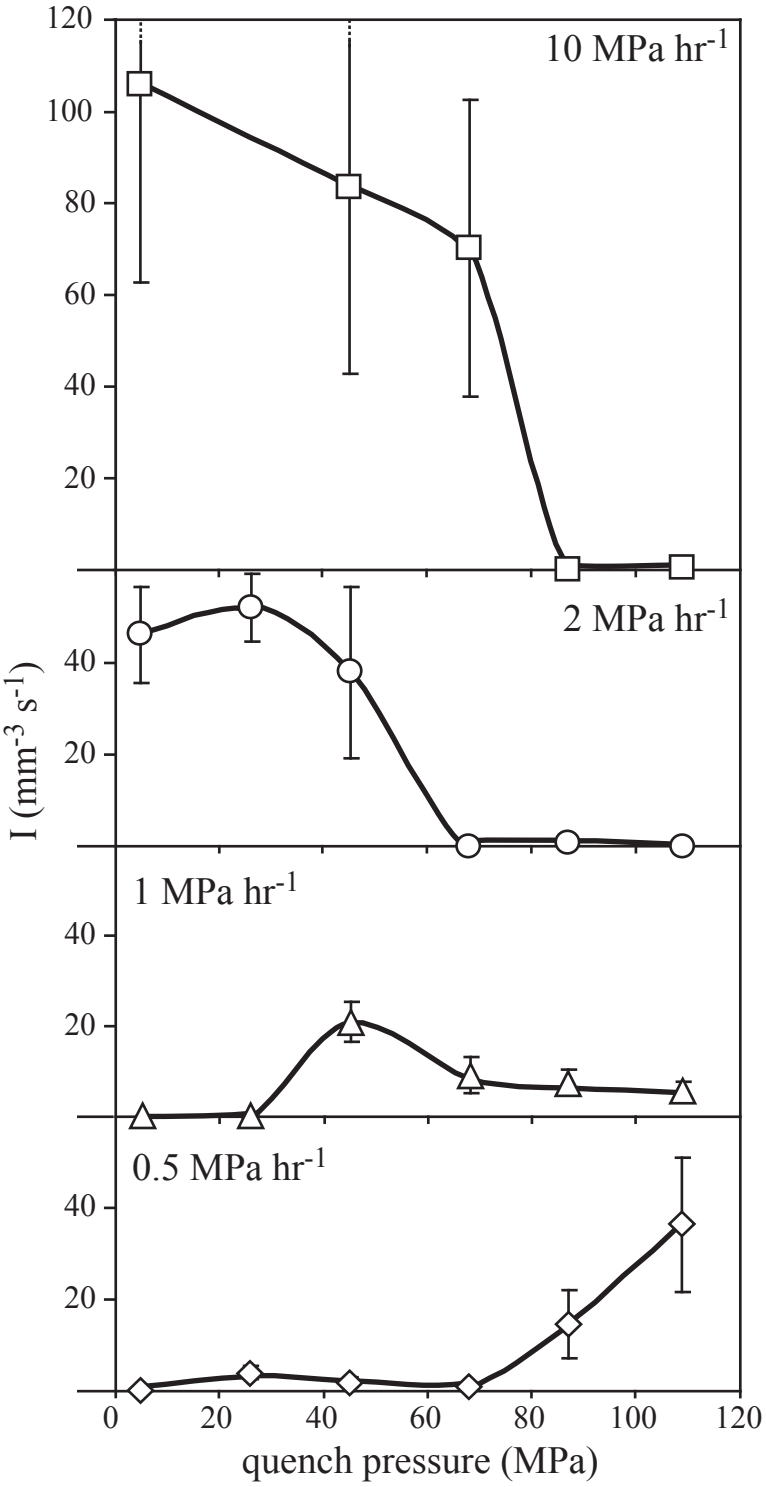

Fig. 2.9. Nucleation rate (I) of plagioclase microlites in each sample as a function of quench pressure. Error bars are 1σ values.

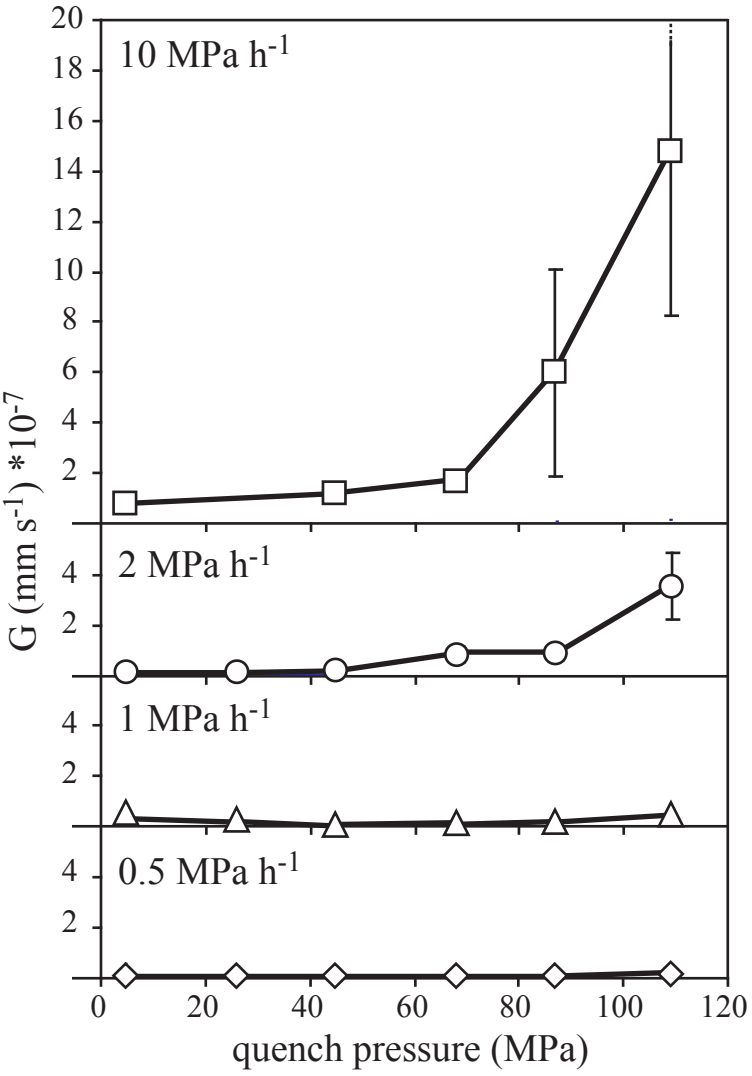

Fig. 2.10. Growth rate (G) of plagioclase microlites in each sample as a function of quench pressure. Error bars are 1σ values.

DISCUSSION

Melt Evolution During Decompression

Compositions of anneal and snapshot glasses are projected into the haplogranite (Qtz-Ab-Or) ternary diagram using the scheme of Blundy & Cashman (2001; Figure 2.11), a tool for tracking liquid lines of descent (LLD) in silicic liquids with ≤1 wt% normative corundum (e.g., Cashman & Blundy, 2000; Hammer & Rutherford, 2002; Couch *et al*., 2003b; Martel & Schmidt, 2003). At each quench pressure, the liquid compositions of the four anneal runs are the same within uncertainty (Figure 2.11a). Together, these anneal melts define a trend interpreted to represent the equilibrium liquid line of descent. Between 130 and 45 MPa all of the anneal melts follow a similar trajectory away from the Ab-component towards the feldspar-quartz cotectic, consistent with progressive crystallization of feldspar. Between 45 and 5 MPa the anneal trend reaches the cotectic, having saturated with a silica phase, and bends toward the Qtz-Or join. While the position of the 5 MPa quartz-feldspar cotectic in Qtz-Ab-Or haplogranitic melts has not been explicitly determined, the positions of the cotectic between 500 and 50 MPa were determined by Tuttle & Bowen (1958), Luth *et al*. (1964), and Ebadi & Johannes (1991) and the one atmosphere (0.1 MPa) cotectic was defined by Brugger *et al*. (2003) using projections of natural rock experimental data into the Qtz-Ab-Or system (projection scheme of Blundy & Cashman, 2001). The 5 MPa anneal runs plot in the approximate location of the interpolated 5 MPa cotectic.

Two snapshot samples containing >1.7 wt.% normative corundum, both quenched at 45 MPa, are labeled on the plot but omitted from discussion because they fall outside of the compositional range accounted for in the projection scheme. As expected from the

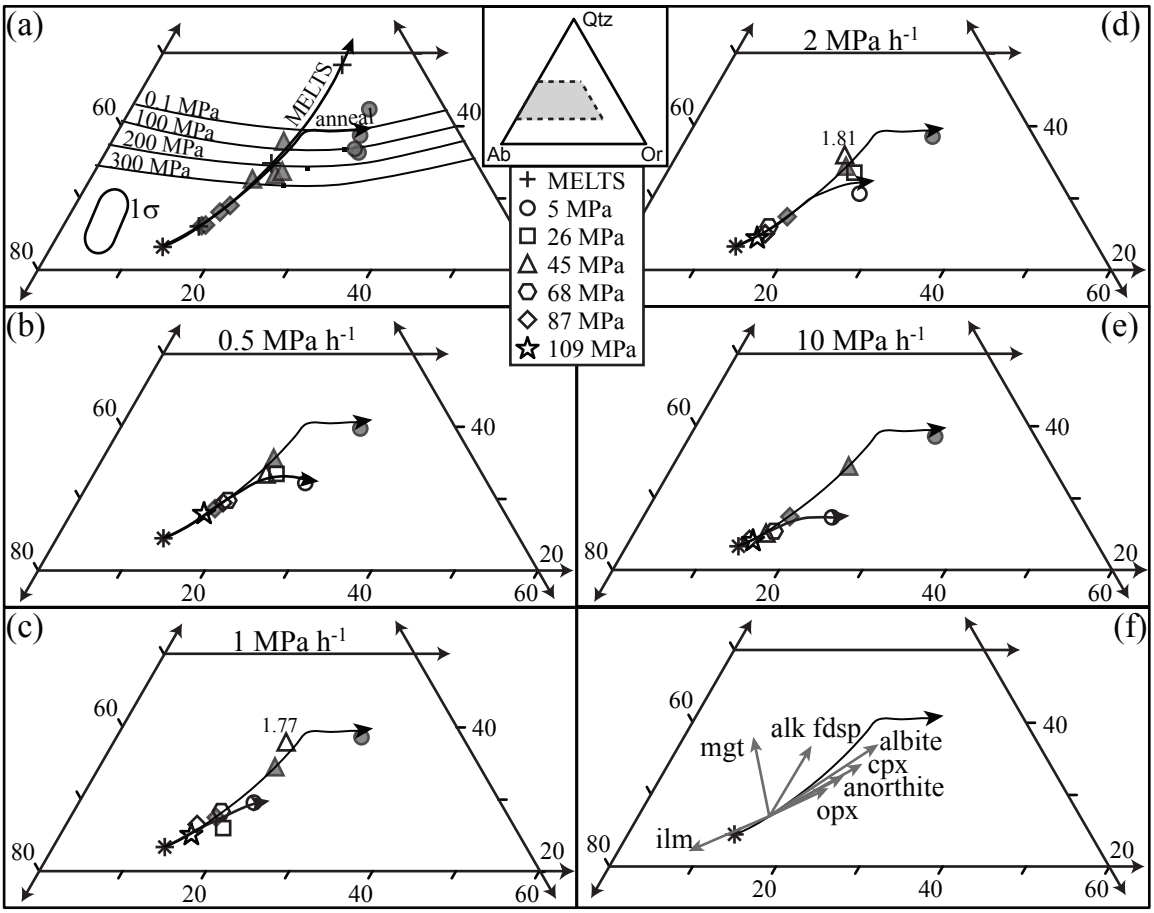

Fig. 2.11. Projection of snapshot, anneal, and MELTS calculated liquids into the Qz-Ab-Or ternary diagram using the projection scheme of Blundy & Cashman (2001). The dashed quadrilateral in the inset represents the area depicted in (a)-(f). The star (*) in each panel represents the glass composition of the starting material after annealing for ≥24 h at 130 MPa and 880˚C. The MELTS modeling utilized this glass composition along with 4.33 wt% H_2O, [the saturation value calculated by the water solubility model of Moore *et al*. (1998)], an oxygen fugacity corresponding to NNO+1, and bulk equilibrium crystallization. (a) Comparisons between MELTS calculated liquids (black crosses) and anneal experiments at 87 MPa (filled diamonds), 45 MPa (filled triangles), and 5 MPa (filled circles) for each decompression series. A liquid line of descent trajectory is shown for MELTS and for the anneal experiments. Quartz-feldspar cotectics and thermal minima are shown for 300, 200, 100, and 0.1 MPa. The 1σ error ellipse for experimental glasses is based on the chemical errors of SiO_2, Na_2O, and K_2O (Table 3) and applies to (a)-(e). (b-e) Snapshot experiments (open symbols) at each quench pressure and estimated snapshot trajectory compared with the anneal liquid line of descent (filled symbols represent the average anneal composition). Two samples contain >1 wt% normative corundum, the maximum abundance accounted for in the projection scheme. The normative corundum abundance in these two samples are labeled in (c) and (d). (f) Given a melt composition lying on the equilibrium liquid line of descent, each arrow represents the trajectory of the melt resulting from crystallization of a particular phase (magnitude of the arrow is not relevant, only direction).

glass data, the LLD of snapshot experiments performed at all decompression rates initially tracks with the anneal curve, but deviates appreciably at $P_f \leq 45$ MPa (Figure 2.11b-e). Surprisingly, the low- P_f snapshot glass compositions appear to plot on a high pressure (~500 MPa) quartz-feldspar cotectic, as they are significantly closer to the Qtz-Or join than the equilibrium LLD trend, and they are further from the Qtz apex than any plausible low-pressure cotectic. However, none of the snapshot runs contain a trace of crystalline silica, and so the turn toward the Qtz-Or join is not the result of quartz (or cristobalite)+plagioclase co-crystallization. This low-pressure deflection toward the Qtz-Or join without crystallization of a silica phase has been observed in previous decompression experiments involving silicic melts (Hammer & Rutherford, 2002; Martel & Schmidt, 2003). One possible explanation for this deflection is crystallization of excessively Ca-rich feldspar, which results in a downward bend of the LLD (Figure 2.11f). Another possibility is that the deflection is caused by a decrease in the proportion of feldspar in the crystallizing assemblage. That is, although the SiO_2 contents (anhydrous basis) of the 5 MPa snapshot glasses are identical to the SiO_2 contents of 45 MPa glasses, their K_2O contents are higher and Al_2O_3 unchanged (Figure 2.5). In order for Al_2O_3 to become only moderately compatible in the crystallizing assemblage, another phase must ascend in volumetric dominance. Declining proportionate feldspar contribution could arise from excess orthopyroxene (for example) crystallization, but is more likely due to declining rate of plagioclase crystallization. Both possibilities may act in concert. As discussed previously, snapshot samples consistently contain less feldspar than the corresponding anneal samples, and the discrepancy increases with decreasing P_f

(Figure 2.7a). In addition, snapshot feldspar is on average more Ca-rich than anneal feldspar for a given P_f (Figure 2.6), as discussed in greater detail below.

The MELTS algorithm (Ghiorso & Sack, 1995; Asimow & Ghiorso, 1998) is widely used to calculate equilibrium phase relations in mafic igneous systems (e.g., Trua *et al*., 2002; Eason & Sinton, 2006; McCarter *et al*., 2006; Fowler *et al*., 2007). Due to a lack of sufficient phase equilibrium data for hydrous multicomponent magmas at pressure <200 MPa, the model is not considered applicable to crystallization of magmas such as andesites, dacites, or rhyolites at crustal conditions. The anneal experiments described here, which we believe represent points along an equilibrium LLD during isothermal decompression, provide an opportunity to assess the predictive ability of MELTS outside its calibration range. Applying the intensive variables of the experiments presented here (880˚C, P_i=130 MPa, fO_2=NNO+1), we model crystallization of the H_2O-saturated Aniakchak starting material using bulk equilibrium crystallization and a pressure step-size of 1 MPa. The MELTS calculated LLD closely matches the glass compositions of the anneal samples between 130 and 45 MPa (Figure 2.11a). However, at 5 MPa the MELTS liquid overshoots the anneal-derived 5 MPa quartz-feldspar cotectic by approximately 10 normative wt% Qtz (Figure 2.11a), and finally predicts silica saturation at 3 MPa. MELTS also fails to predict formation of apatite, clinopyroxene, and alkali feldspar at any pressure. In summary, MELTS adequately predicts the early stages of melt evolution due to isothermal decompression, although it does not generate the observed phase assemblage or low-pressure phase relations.

Crystallization Kinetics

The time-invariance of anneal run melt compositions allows utilization of these samples to determine chemical disequilibrium in snapshot experiments. By comparing plagioclase volume fractions in anneal and snapshot runs at the same quench pressure, relative magnitudes of crystal supersaturation ($\Delta\phi$)

$$\Delta\phi = \phi_{\text{anneal}} - \phi_{\text{snapshot}} \qquad \text{Eq. (3)}$$

can be used to evaluate how the magnitude of chemical disequilibrium progressively changes during decompression as a function of decompression rate. For snapshot samples with no pressure-equivalent anneal run, equilibrium plagioclase volume fraction is interpolated from neighboring anneal runs. If a snapshot run and corresponding anneal run contain the same volume of plagioclase, $\Delta\phi=0$ and they are presumed equally crystalline. For all decompression rates examined, $\Delta\phi$ correlates inversely with quench pressure, and as pressure decreases, $\Delta\phi$ increases at an accelerating rate (Figure 2.12a). Quench pressure has a much stronger influence on $\Delta\phi$ than does decompression rate, except at the highest quench pressures where rapidly decompressed samples experience a delay in nucleation of plagioclase, which leads to slightly higher $\Delta\phi$ values. The positive relationship between melt viscosity (calculated using Giordano *et al.*, 2008) and $\Delta\phi$ (Figure 2.12a inset) hints at the nature of the control on accumulated driving force. With decreasing P_{H2O} and thus increasing viscosity, diffusivities of crystal-forming components in the melt decrease and interface reactions become more sluggish.

In agreement with previous studies of crystallization kinetics, growth rate appears to depend on the magnitude of chemical disequilibrium, although the nature of the dependence varies with decompression rate (Figure 2.12b) (Lofgren, 1980; Kirkpatrick,

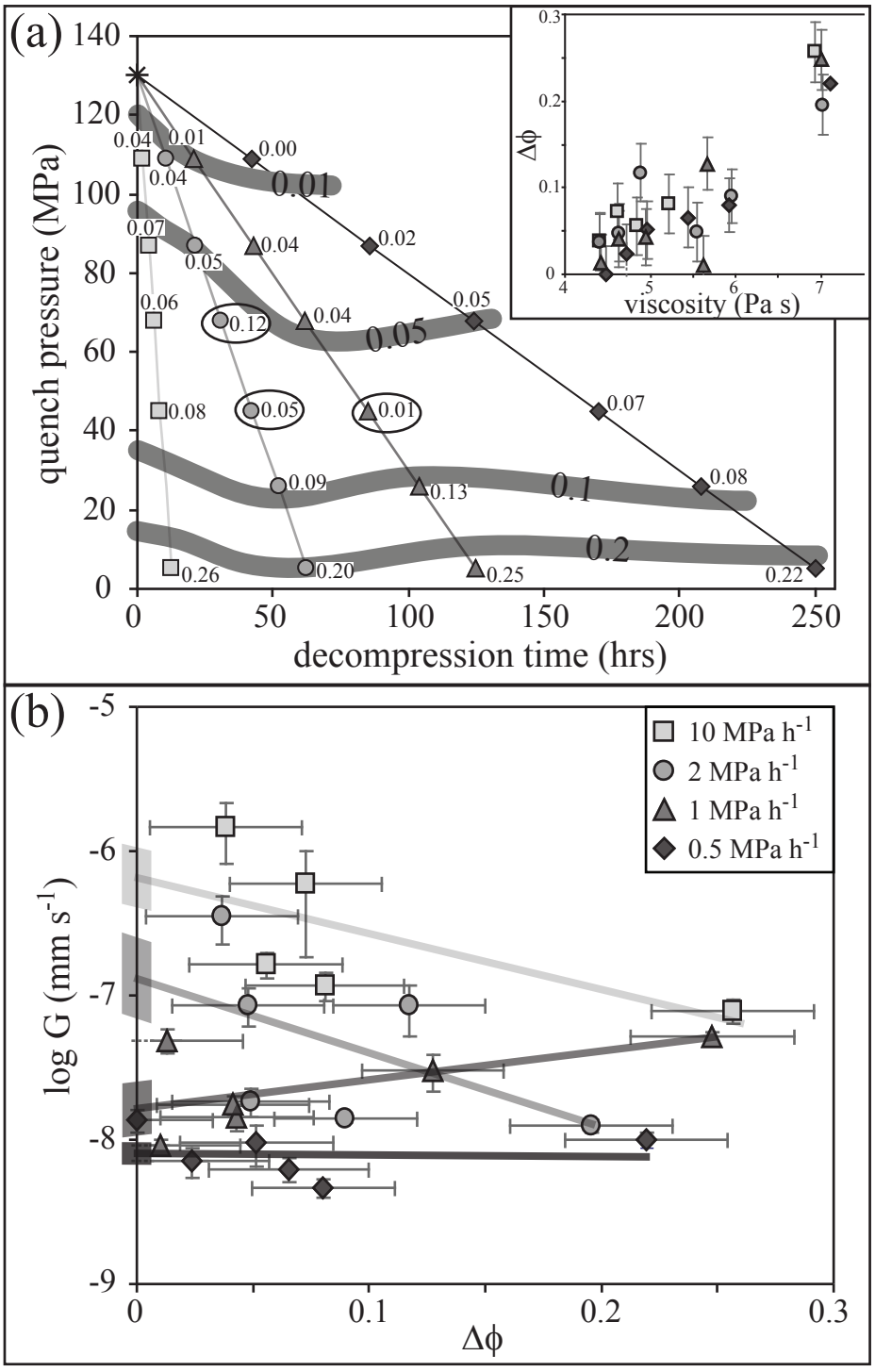

Fig. 2.12. (a) Δϕ contours (wide bands) for values of 0.01, 0.05, 0.1, and 0.2 are drawn by connecting equal interpolated Δϕ values in each set of snapshot samples (Δϕ values are written next to each experiment). Circled symbols do not satisfy the isograd characterization as drawn. Inset: Melt viscosity calculated using the model of Giordano *et al*. (2008) using the melt composition for each sample and its water content at the quench pressure, calculated after Moore *et al*. (1998). (b) Plagioclase growth rate (G) as a function of crystal supersaturation, and the linear best fit for each decompression series. Shaded regions on the y-axis represent the linear extrapolation of log G back to Δϕ=0, and the heights of the shaded regions reflect scatter in the data.

1981; Cashman, 1990). With the exception of the 1 MPa h^{-1} series, all decompression rates produce maximum growth rates (G_{max}) at very low $\Delta\phi$, in agreement with theory (Dowty, 1980a; Kirkpatrick, 1981). Importantly, the value of G_{max} correlates with decompression rate. Fast decompression results in the highest crystal growth rates, and slower decompression causes slower crystal growth (Figure 2.10 and 2.12b).

The preceding estimates of nucleation (I) and growth (G) rates were calculated in the same manner as all prior experimental decompression studies of crystal nucleation and growth rates (e.g., Hammer & Rutherford, 2002; Couch *et al.*, 2003). Although useful, these values incorporate the full decompression duration up to the point of quench and do not reflect instantaneous rates of nucleation and growth. While truly instantaneous rate measurements require continuous knowledge N_V and S_N variations through time, near-instantaneous nucleation and growth rates can be estimated using neighboring snapshot experiments. Snapshot nucleation rates (I_{snap}) and growth rates (G_{snap}) are calculated using differences in N_V and S_N, respectively, between adjacent snapshot experiments divided by the time spent between the two pressures. For example, G_{snap} between 68 and 45 MPa = ($N_{V\ 45MPa} - N_{V\ 68\ MPa}$) / (time $_{45MPa}$ – time $_{68\ MPa}$). I_{snap} and G_{snap} are still time-averaged values, but they are computed over moving time windows of relatively short duration so they more closely approximate instantaneous rates. To the extent that I and G represent continuous functions of number density and size with respect to quench pressure (sparsely sampled in our experiments; Figures 2.9 and 2.10), I_{snap} and G_{snap} are ideally the instantaneous rates of change of these functions. In fact, the maximum I_{snap} and G_{snap} values occur at pressures corresponding to the steepest sloping line segments on Figures 2.9 and 2.10, respectively. Values of maximum near-

instantaneous nucleation and growth rates are up to 3 times greater than their time–integrated counterparts. Most importantly, the maximum near-instantaneous I_{snap} and G_{snap} are coherently and monotonically related to decompression rate (Figure 2.13). We conclude that magma ascent rate exerts the primary control on instantaneous rates of plagioclase nucleation and growth, presumably because transformation kinetics are intimately linked to the degree of thermodynamic disequilibrium.

Interestingly, all four decompression rates appear to result in the same amount of plagioclase (Figure 2.7a) and produce melts with similar compositions (Figure 2.5 and Table 2.2) for any given P_f, despite large differences in the rates of plagioclase nucleation and growth. An inverse relationship between the rates of nucleation and growth (which are *individually* sensitive to decompression rate) leads to apparent path-independence with respect to overall crystallinity (Figure 2.7a). This is consistent with cooling rate studies on calcalkaline and high-K calcalkaline Stromboli lavas which find similar liquid lines of descent in magmas undergoing very different cooling histories (Conte *et al*., 2006). Conte *et al*. (2006) conclude that dynamic crystallization conditions have little effect on the residual liquid compositions in multiply saturated assemblages.

MSD vs CD

Magma ascent is very likely fitful during volcanic eruptions, with accelerations and decelerations, irregular pauses and periods of continuous rise (Tuffen *et al.,* 2003; Roman & Cashman, 2006; Smith *et al*., 2007; Scandone *et al*., 2007). Examination of the effects of discontinuous magma ascent is a line of experimental inquiry that would be well suited to examination by the programmable pressure variator, as the preceding MSD

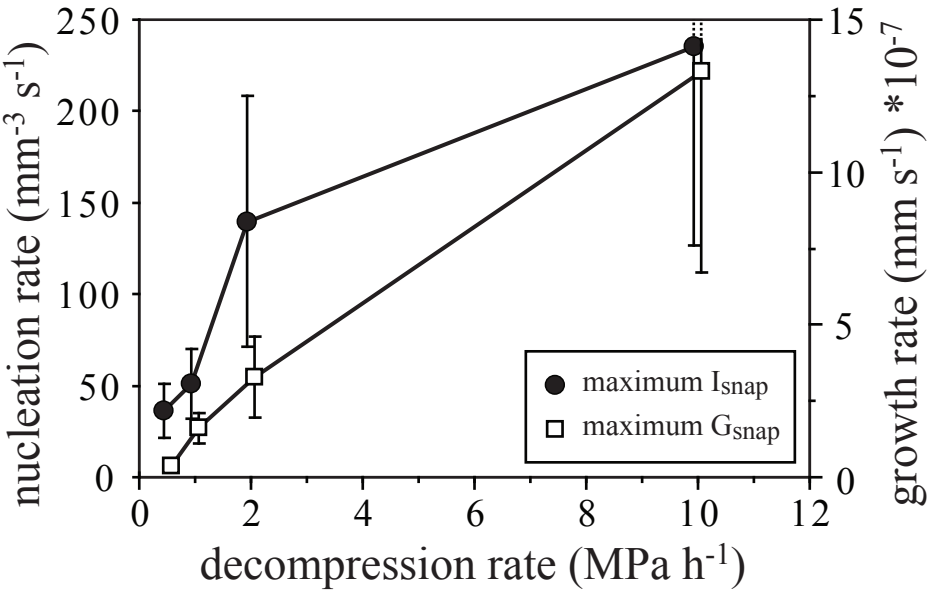

Fig. 2.13. Maximum values of near-instantaneous nucleation and growth rates (I_{snap} and G_{snap}) plotted as a function of decompression rate. I_{snap} and G_{snap} are calculated using the time duration and change in N_V and S_N, respectively, between neighboring snapshot experiments (see text). Error bars are 1σ values. I_{snap} and G_{snap} are offset slightly on the x-axis for clarity.

experimental studies have employed a variety of multi-step methodologies (Hammer & Rutherford, 2002; Couch *et al.*, 2003b; Martel & Schmidt, 2003). In fact, prior experimental work has employed multiple step decompressions out of technical necessity, with no stated intention of replicating the complexities of a natural process. While the simple CD scenario we examine is not necessarily more realistic than MSD in principle, the continuous decompression suite provides an essential reference case for any future systematic study of the effects of fitful ascent dynamics on crystal texture.

Textural comparisons between 1 MPa h^{-1} MSD and CD runs indicate that stepwise decompression yields textures correlative with faster decompression than the IDR would indicate. Plagioclase crystals in CD samples appear faceted suggesting interface reaction controlled growth (Figure 2.4; Lofgren, 1974; Sunagawa, 1981), typically associated with growth at low effective undercooling. However, these crystals contain occasional melt inclusions and some swallowtail morphologies demonstrating that they have not undergone near-equilibrium crystallization throughout their formation. In contrast, plagioclase crystals in MSD runs are dominantly hopper and skeletal (Figure 2.4), indicating a diffusion-limited growth throughout decompression and probably consistently higher effective undercooling (Lofgren, 1974; Corrigan, 1982; Hammer & Rutherford, 2002). Without independent knowledge of the decompression histories of these two samples afforded by the experimental methods, these textural variations would likely be attributed to different magma ascent rates or different closure pressures (Lofgren, 1973; Hammer & Rutherford, 2002).

The mismatch in crystal contents produced in multi-step and continuous decompression at comparable IDR has important implications for the volcanological

applications of dynamic crystallization experiments. The consistently lower crystallinities produced during these pilot MSD experiments suggest that quantitative determination of closure pressure of continuously ascended natural rocks using a MSD calibration set could overestimate closure pressure and therefore depth of magma crystallization. As decompression rate increases and step size decreases the differences between CD and MSD experiments will presumably lessen. Further experiments are clearly needed to explore the extent of the MSD-CD textural mismatch with regard to different pressure increments and time steps.

Plagioclase compositions

It is well known from phase equilibrium studies that the An-content of plagioclase decreases continuously with decreasing temperature and P_{H2O} (e.g., Moore & Carmichael, 1998; Couch *et al*., 2003a; Larsen, 2006). Syn-eruptive crystallization, however, is inherently a disequilibrium process. In dynamic systems, the rate of decompression, degassing, and cooling control diffusivities of chemical components in the melt, crystallization rates, and melt composition. In agreement with Castro & Gardner (2008), our results do not support a clear relationship between decompression rate and feldspar composition, although we acknowledge that the small size of elongate crystals formed during rapid decompression precludes quantitative analysis to fully test this assertion. However, there is a robust relationship between the most albitic crystals and P_f, which is revealed when experimental glass and plagioclase compositions are projected into the binary Ab-An system to generate a P_{H2O}-X diagram (Figure 2.14). By direct analogy with the T-X plagioclase loop, glass compositions become more Ab-rich with

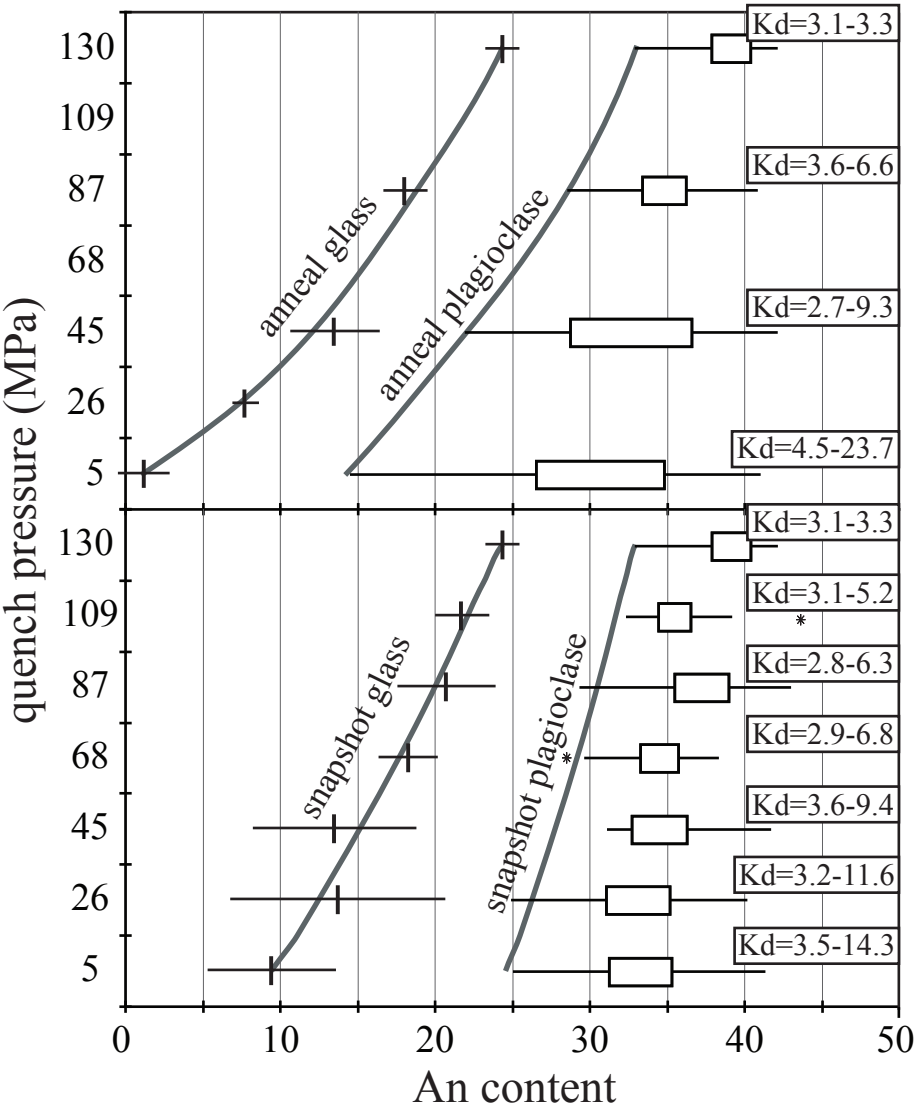

Fig. 2.14. Albite-Anorthite loop diagram as a function of pressure. The An and Ab component of the melt is determined by using the glass composition at each pressure to calculate the CIPW mole proportion of An and Ab (shown normalized to 100%). All runs at the same quench pressure are averaged together with error bars representing 1σ variation. For plagioclase compositions the An+Ab components are normalized to 100%. Because of the large variation in plagioclase compositions, all samples quenched at the same pressure are plotted together regardless of decompression rate. The edges of each box represent the upper and lower quartile of all the analyzed plagioclase crystals at a given quench pressure. The left end of the bar and right end of the bar represent the most Ab-rich and most An-rich crystals, respectively. The stars (*) are outlier compositions, defined as greater than 1.5 x IQR (inter-quartile range) from the upper or lower quartile value. The range of Kd values for each quench pressure is shown.

decreasing pressure, and they are always more Ab-rich than the coexisting plagioclase crystals. As previously discussed, An_{39}- An_{43} crystals are present in every run because crystals with this composition formed during the initial dwell period. In anneal samples, the range of plagioclase compositions increases with decreasing pressure; thus we interpret the compositions of the most albitic crystals to reflect growth near the quench pressure. Snapshot experiments also display a general trend of increasingly albitic compositions with decreasing pressure, however anneal experiments always contain more Ab-rich crystals than snapshot experiments at the same P_f (Figure 2.14). This agrees with previous studies reporting plagioclase crystallizing in equilibrium isobaric experiments as more albitic than those forming in MSD experiments at the same P_f (Martel & Schmidt, 2003; Suzuki *et al*., 2007). Thus, even the most Ab-rich plagioclase crystals in snapshot CD samples do not represent compositional equilibrium crystallization from the coexisting melt despite the fact that high pressure snapshot experiments contain the equilibrium feldspar abundance (Figure 2.7).

Calcium-sodium partition coefficients for plagioclase are calculated using the molar fraction (X) of CaO and Na_2O in crystals and glass, where

$$Kd = \frac{\left(X_{CaO}^{plag} / X_{Na_2O}^{plag}\right)}{\left(X_{CaO}^{glass} / X_{Na_2O}^{glass}\right)} \qquad \text{Eq. (4)}$$

(Figure 2.14, Appendix 2.B). Comparisons between plagioclase compositions in experiments and natural rocks have been used to interpret crystallization pressures, magma ascent rates, and the compositional history of coexisting magmas (e.g., Martel *et al*., 2006; Suzuki *et al*., 2007). For instance, microlites in the Mount Pelée silicic melt are interpreted (Martel *et al*., 2006) to be inherited from a basaltic magma because Ca/Na

partition coefficients are greater than 5, typically viewed as the upper limit in island-arc magmatic systems (Sisson & Grove, 1993; Martel *et al.*, 1999; Pichavant *et al.*, 2002). However, results of this study show that early-formed microlites do not re-equilibrate with the melt over the decompression timescales examined, and thus they are more An-rich than equilibrium plagioclase (Figure 2.14). While it is possible that these micron-scale crystals have extremely thin rims in compositional equilibrium with the melt, no rims are visible in BSE images; and if existant, are too narrow to analyze with a standard electron microprobe. Thus, microlites may retain high partition coefficients as a natural consequence of disequilibrium crystallization during dynamic decompression. Echoing the cautions presented a quarter century ago in the lunar crystallization literature (Grove & Bence, 1979) for mafic minerals, we suggest that phase equilibrium experiments on silicic magmas are inadequate for interpreting hydrous magma ascent processes from crystals formed at disequilibrium.

IMPLICATIONS

It has long been recognized that plagioclase growth rates vary as a function of cooling rate (Walker *et al.*, 1978; Cashman, 1993; Lesher *et al.*, 1999; Conte *et al.*, 2006), and this study suggests that growth rates also depend on decompression rate (Figure 2.10 and 2.13). Instantaneous plagioclase growth rates vary by >3 orders of magnitude over the range of decompression rates examined. If ascent rate varies during decompression, which is extremely likely for natural magmas undergoing closed-system degassing, then plagioclase growth rates may likewise vary by several orders of magnitude during ascent (Figure 2.10; Hammer & Rutherford, 2002; Couch *et al.*, 2003b). This variation has

important implications for calculations of magmatic timescales that utilize crystal growth rates, a topic presented in greater detail in Chapter 3.

In agreement with previous studies of decompression-induced crystallization, our results clearly indicate that decompression rate is an important factor controlling crystal morphologies and microlite number densities in volcanic rocks. Examination of the 5 MPa experiments, which most closely represent products of natural decompression during volcanic eruptions, reveals an increasing prominence of disequilibrium morphologies as decompression rate increases (Figure 2.2). This trend is consistent with previous studies that map morphological changes with increasing effective undercooling: from compact euhedral, to tabular, then swallowtail and hopper (Lofgren, 1974; Corrigan, 1982; Hammer & Rutherford, 2002). Samples in each decompression series experienced different degrees of undercooling, different rates of crystal nucleation and growth, and thus different final microtextures. Faster decompression produces high microlites number densities that record late-stage high instantaneous effective undercooling, while lower N_A (Figure 2.7b) and the euhedral morphologies of growth-dominated crystallization reflect smaller instantaneous undercooling throughout slow decompression.

Surprisingly, our CD experiments reveal no relationship between N_V and quench pressure, as has been reported for MSD experiments (Hammer & Rutherford, 2002; Couch *et al*., 2003b), and utilized in interpreting natural samples (Cashman & McConnell, 2005; Clarke *et al*., 2007; Blundy & Cashman, 2008). Also counterintuitive, we find no relationship between decompression rate and plagioclase microlite compositions, glass compositions, or plagioclase volume fractions. Although the snapshot

samples are texturally disparate (Figure 2.2), and they clearly did not all attain chemical equilibrium (Figures 2.5, 2.7, 2.11, and 2.14), they do contain approximately equal volumes of plagioclase crystals at each given quench pressure (Figure 2.7a). The difference between ϕ in snapshot and anneal experiments increases with continued decompression, indicating declining chemical equilibrium that is remarkably insensitive to decompression rate. Within the range of decompression rates investigated in this study, growth of preexisting crystals and nucleation of new crystals apparently sustains a given (disequilibrium) proportion of feldspar at each pressure, and samples consistently maintain low, but non-zero, effective undercooling.

Results from decompression experiments are commonly compared with textural characteristics of natural rocks to make interpretations about magma ascent rates (e.g., Rutherford & Hill, 1993; Hammer & Rutherford, 2002; Couch *et al*., 2003b; Nicholis & Rutherford, 2004; Cashman & McConnell, 2005). The well-founded premise of these studies is that decompression rate exerts of first-order control on crystal microtextures. However, our comparisons between continuous and multi-step decompression experiments at an integrated decompression rate of 1 MPa h^{-1} suggest that magma ascent style may also govern crystallization textures to a first order. In fact, within the range of decompression rates studied here, decompression style has a more pronounced effect on crystal number densities and morphologies than decompression rate. Just as magma ascent rates vary widely across volcanic systems, ascent styles probably span a wide range from purely continuous to entirely pulsatory. In addition, the style of magma ascent almost certainly varies between various magmatic systems and perhaps temporally within any given system. Thus, consideration of ascent style in addition to rate will undoubtedly

strengthen the interpretive power of experimental studies for constraining natural magma ascent processes. Evaluation of natural textures with the goal of quantitative interpretation of magma ascent rate may only be meaningful using experimentally calibrated systems that are chemically and thermally similar to the test case. Thus, continuous decompression experiments provide an essential reference case for any future systematic study of textures in naturally decompressed magmas. Future work in this field needs to explore textural variations between MSD and CD experiments with a range of pressure- and time-steps and with a variety of magma compositions in an effort to better understand how decompression style controls textural characteristics.

ACKNOWLEDGEMENTS

Thanks to Jessica Larson for supplying the Aniakchak rhyodacite starting material and to Mac Rutherford, Barbara Jean Kahawaii, Lisa Tatsumi-Petrochilos, and Julie Bowles for their help running several experiments. Also thanks to Eric Hellebrand, Mike Garcia, and John Donovan for their assistance with electron microprobe analyses. This paper was significantly improved by constructive reviews by Wendy Bohrson, Caroline Martel, and two anonymous reviewers. This work was supported by National Science Foundation CAREER award [EAR04-49888 to J.E.H.].

APPENDIX 2.A. Backscatter electron images of textures 10 MPa h^{-1}

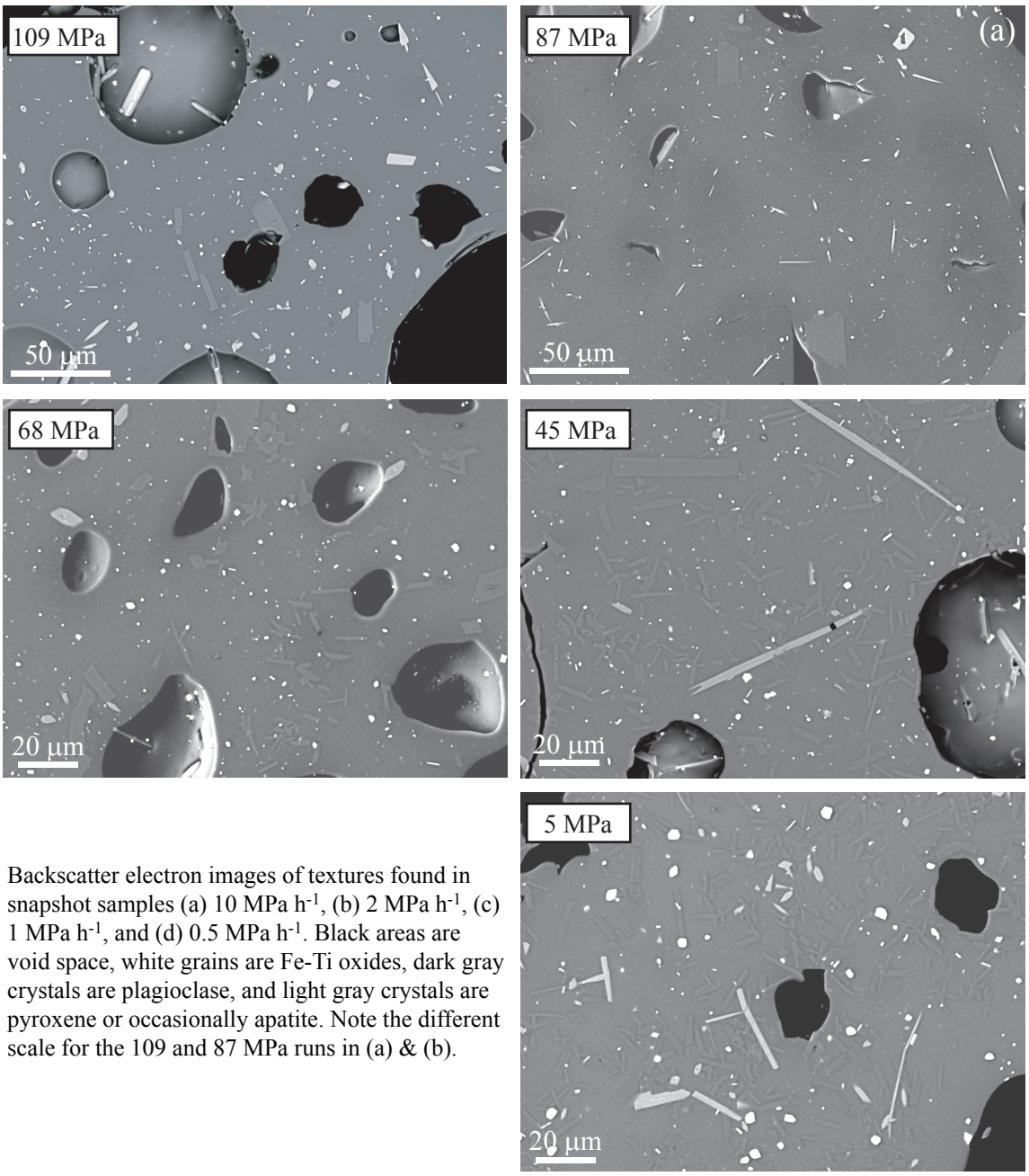

Backscatter electron images of textures found in snapshot samples (a) 10 MPa h^{-1}, (b) 2 MPa h^{-1}, (c) 1 MPa h^{-1}, and (d) 0.5 MPa h^{-1}. Black areas are void space, white grains are Fe-Ti oxides, dark gray crystals are plagioclase, and light gray crystals are pyroxene or occasionally apatite. Note the different scale for the 109 and 87 MPa runs in (a) & (b).

APPENDIX 2.A. (continued) Backscatter electron images of textures 2 MPa h^{-1}

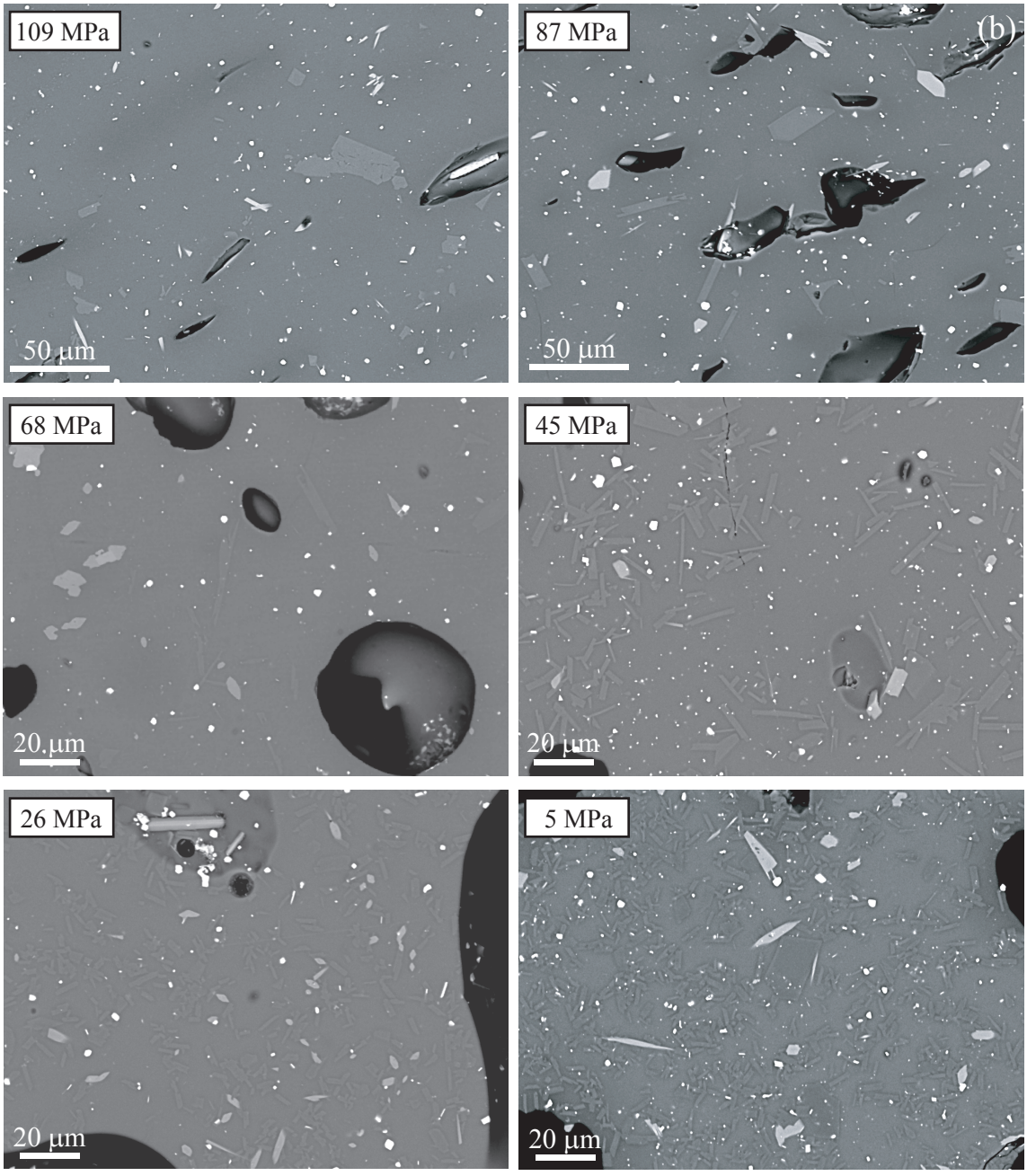

APPENDIX 2.A. (continued) Backscatter electron images of textures 1 MPa h^{-1}

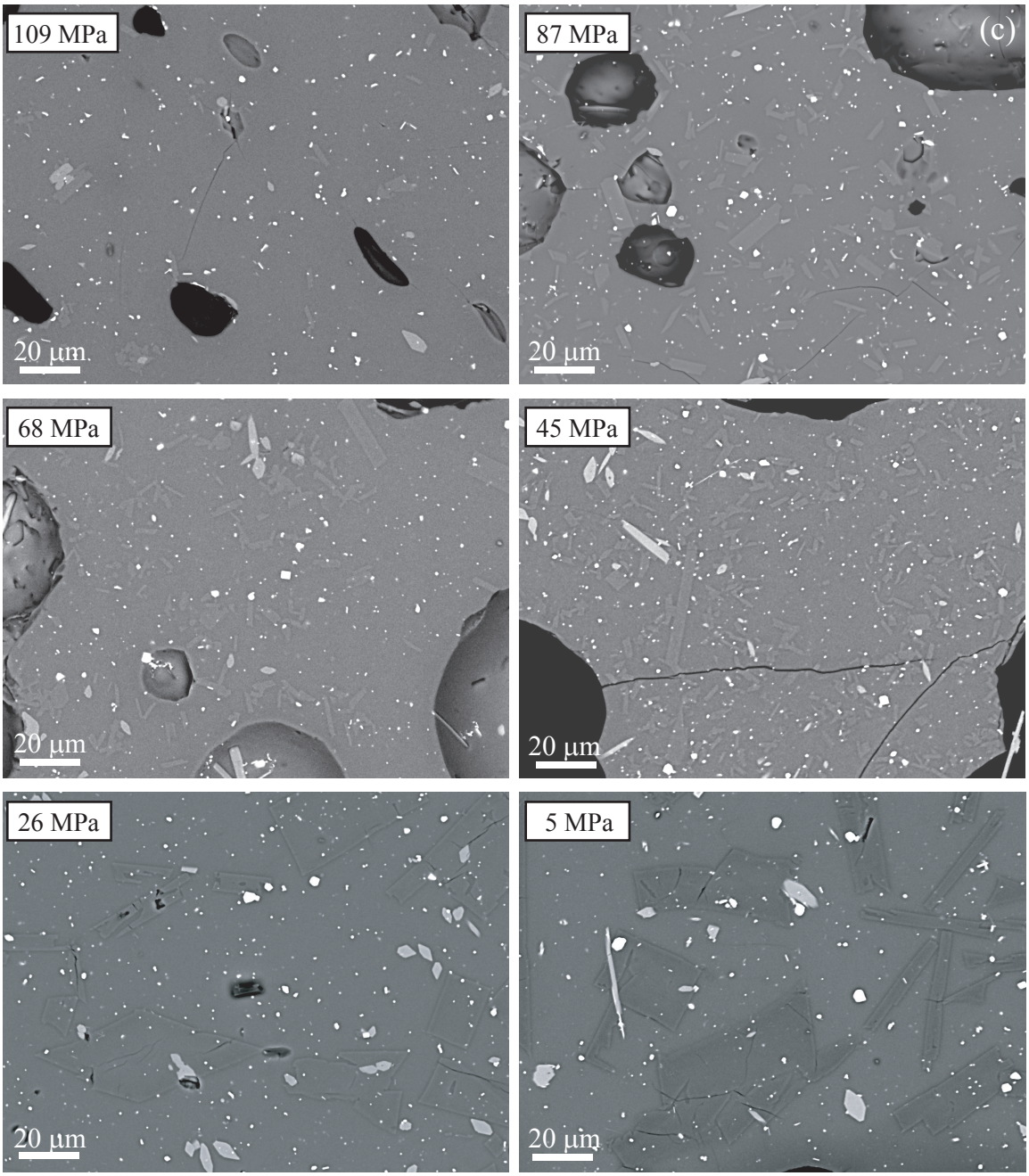

APPENDIX 2.A. (continued) Backscatter electron images of textures 0.5 MPa h^{-1}

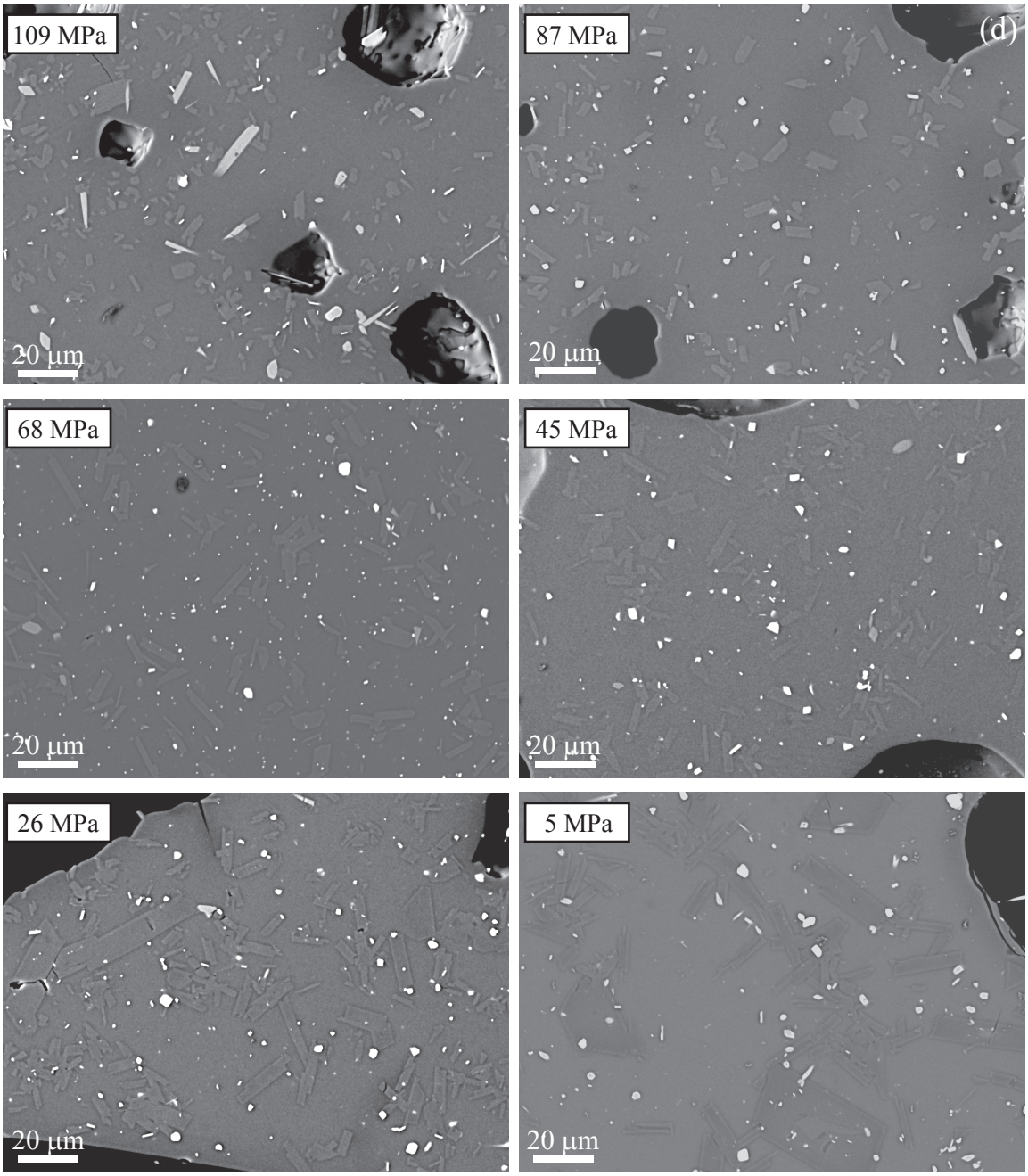

APPENDIX 2.B. Compositional analyses of all analyzed feldspar crystals

Sample	Na_2O	Al_2O_3	SiO_2	K_2O	CaO	FeO[1]	total	An	Ab	Or	Kd[2]
5-1	6.7	26.3	57.7	0.3	8.2	n.d	99.3	39.57	58.64	1.79	6.5
	6.9	26.0	58.3	0.3	8.0	n.d	99.6	38.39	59.88	1.73	6.1
	7.1	26.0	58.1	0.3	8.0	n.d	99.5	37.80	60.41	1.78	6.0
	6.9	26.2	57.9	0.3	8.2	n.d	99.4	39.19	59.20	1.61	6.3
	7.0	25.9	58.4	0.3	7.8	n.d	99.5	37.28	61.02	1.70	5.9
	7.0	25.9	58.5	0.3	7.7	n.d	99.5	37.07	61.17	1.76	5.8
	8.2	23.3	61.9	0.7	5.1	n.d	99.2	24.37	71.81	3.82	3.3
	8.2	23.3	61.4	0.6	5.2	n.d	98.6	25.07	71.65	3.27	3.4
	7.9	23.6	61.4	0.7	5.5	n.d	99.1	26.51	69.65	3.84	3.6
	8.7	22.9	63.0	0.7	4.4	n.d	99.7	21.15	74.98	3.87	2.7
	8.4	23.4	62.4	0.6	4.8	n.d	99.7	23.29	73.16	3.55	3.1
5-2	6.9	25.0	60.3	0.4	6.9	n.d	99.5	34.98	62.84	2.18	5.1
	7.0	24.9	61.0	0.4	6.4	n.d	99.7	32.74	64.93	2.33	4.6
	7.1	24.9	60.3	0.4	6.5	n.d	99.2	33.01	64.80	2.18	4.7
	6.6	24.5	60.3	0.5	6.8	n.d	98.7	35.33	61.75	2.93	5.2
	7.1	24.7	60.4	0.4	6.5	n.d	99.1	32.66	65.12	2.21	4.6
	7.2	24.8	60.4	0.4	6.6	n.d	99.3	32.59	65.05	2.37	4.6
	7.1	24.5	61.1	0.4	6.4	n.d	99.5	32.27	65.33	2.40	4.5
	7.0	24.9	60.3	0.4	6.6	n.d	99.2	33.62	64.06	2.32	4.8
	7.0	24.8	60.7	0.4	6.6	n.d	99.5	33.32	64.43	2.25	4.7
	7.1	24.5	60.5	0.4	6.4	n.d	98.8	32.60	65.06	2.34	4.6
5-4	6.8	25.3	59.6	0.3	7.1	n.d	99.1	36.07	61.95	1.99	3.7
	6.6	25.5	59.5	0.3	7.5	n.d	99.3	37.79	60.33	1.88	4.0
	6.6	24.7	59.9	0.4	7.0	n.d	98.6	36.29	61.14	2.58	3.7
	6.7	24.5	60.6	0.5	6.7	n.d	99.0	34.57	62.52	2.91	3.5
	6.7	24.6	60.4	0.3	6.7	n.d	98.7	34.76	63.10	2.14	3.5
	6.3	25.9	58.4	0.2	8.1	n.d	99.0	40.73	57.81	1.46	4.4
	6.7	25.6	58.9	0.3	7.7	n.d	99.1	38.11	60.04	1.84	4.0
	6.5	25.8	58.4	0.3	7.9	n.d	98.9	39.62	58.86	1.52	4.2
	6.2	26.3	58.3	0.3	8.3	n.d	99.3	41.85	56.50	1.65	4.7
	5.9	25.5	59.0	0.4	7.8	n.d	98.6	41.04	56.29	2.66	4.6
	6.2	26.2	58.2	0.3	8.4	n.d	99.3	42.14	56.16	1.70	4.7
6-1	7.3	25.4	59.6	0.3	7.1	n.d	99.7	34.365	63.655	1.979	7.9
	7.0	25.9	58.9	0.3	7.6	n.d	99.6	37.121	61.236	1.642	8.9
	7.2	25.4	59.7	0.3	7.1	n.d	99.7	34.556	63.577	1.867	7.9
	7.4	25.0	60.2	0.3	6.7	n.d	99.6	32.681	65.381	1.938	7.3
	7.1	25.6	59.1	0.3	7.3	n.d	99.3	35.644	62.516	1.839	8.3
	6.9	26.0	59.1	0.3	7.5	n.d	99.8	36.999	61.132	1.869	8.8
	6.7	25.8	58.6	0.3	7.8	n.d	99.2	38.492	59.731	1.777	9.4
6-2	7.0	25.6	58.9	0.3	7.4	n.d	99.2	36.22	61.94	1.83	20.0
	7.3	25.1	59.5	0.3	7.1	n.d	99.2	34.18	63.84	1.98	18.3
	6.8	26.4	58.1	0.3	8.0	n.d	99.5	39.02	59.43	1.56	22.4
7-1	7.3	25.5	59.6	0.4	7.1	n.d	100.0	34.29	63.68	2.04	4.4
	7.5	25.7	59.5	0.3	7.1	n.d	100.1	33.84	64.21	1.95	4.3
	7.3	26.0	59.0	0.3	7.5	n.d	100.1	35.63	62.54	1.83	4.6
	7.0	26.2	58.5	0.3	7.9	n.d	99.9	37.99	60.29	1.73	5.1

[1] n.d. indicates FeO was not determined.

[2] Kd values were calculated using the CaO and Na_2O contents of the crystals and coexisting glass.

APPENDIX 2.B (continued)

Sample	Na_2O	Al_2O_3	SiO_2	K_2O	CaO	FeO[1]	total	An	Ab	Or	Kd[2]
7-1	7.2	25.5	58.6	0.3	7.3	n.d	98.9	35.17	63.01	1.83	4.6
	7.5	25.2	59.2	0.4	6.9	n.d	99.2	32.83	65.03	2.15	4.1
	7.0	26.2	58.3	0.3	8.1	n.d	99.8	38.44	59.94	1.62	5.2
	7.3	25.9	58.9	0.3	7.6	n.d	100.0	35.87	62.47	1.66	4.7
	7.0	26.1	58.6	0.3	7.8	n.d	99.8	37.45	60.89	1.66	5.0
	7.1	26.1	59.0	0.3	7.8	n.d	100.2	37.19	61.12	1.69	5.0
	7.3	25.7	59.4	0.3	7.3	n.d	100.0	34.81	63.29	1.91	4.5
	7.4	25.5	59.7	0.4	7.1	n.d	100.0	33.86	64.13	2.01	4.3
7-2	6.9	26.4	58.1	0.3	8.1	n.d	99.7	38.69	59.65	1.66	6.3
	7.1	25.9	58.6	0.3	7.5	n.d	99.3	36.35	61.94	1.71	5.7
	7.0	25.7	58.7	0.3	7.5	n.d	99.4	36.36	61.66	1.98	5.7
	7.1	25.7	58.5	0.4	7.5	n.d	99.2	36.05	61.92	2.04	5.7
	7.1	25.6	58.9	0.3	7.2	n.d	99.1	35.23	62.81	1.96	5.5
7-4	6.7	26.2	58.1	0.3	8.1	n.d	99.4	39.36	59.03	1.62	6.4
	6.7	26.6	58.2	0.3	8.2	n.d	100.0	39.82	58.57	1.61	6.5
	6.7	26.3	58.0	0.3	8.0	n.d	99.3	39.08	59.19	1.72	6.3
	6.9	26.0	58.3	0.3	7.8	n.d	99.3	37.86	60.50	1.64	6.0
	6.6	26.6	57.6	0.3	8.2	n.d	99.3	40.11	58.21	1.68	6.6
	7.3	25.2	58.9	0.4	7.0	n.d	98.7	34.06	63.77	2.16	5.1
	6.6	25.5	58.7	0.4	7.7	n.d	98.9	38.34	59.24	2.41	6.2
	7.3	24.9	59.2	0.3	6.9	n.d	98.7	33.86	64.15	1.98	5.0
	7.3	24.6	59.8	0.5	6.6	n.d	98.8	32.47	64.75	2.77	4.8
8-1	7.4	25.2	59.4	0.4	7.1	n.d	99.5	33.77	64.19	2.03	8.1
	7.6	24.9	59.2	0.4	6.6	n.d	98.8	31.73	66.01	2.26	7.4
	7.6	25.0	60.1	0.4	6.6	n.d	99.7	31.66	66.18	2.15	7.3
	7.7	24.7	60.3	0.4	6.3	n.d	99.4	30.44	67.22	2.34	7.0
	7.2	25.6	59.2	0.3	7.2	n.d	99.5	35.07	63.16	1.77	8.5
	7.6	25.1	59.5	0.4	6.8	n.d	99.4	32.46	65.54	2.00	7.6
8-3	7.4	25.3	59.3	0.4	7.0	n.d	99.3	33.43	64.45	2.12	8.0
	7.8	24.7	60.1	0.4	6.5	n.d	99.5	30.93	66.86	2.21	7.1
	7.4	25.5	59.1	0.3	7.0	n.d	99.3	33.69	64.39	1.92	8.0
	7.5	25.3	60.0	0.4	6.8	n.d	100.0	32.48	65.03	2.49	7.7
	7.7	25.0	60.1	0.5	6.4	n.d	99.6	30.82	66.47	2.71	7.1
	7.6	24.2	60.0	0.5	6.3	n.d	98.6	30.41	66.70	2.88	7.0
	7.4	25.2	59.9	0.4	6.7	n.d	99.7	32.67	64.76	2.57	7.7
11-1	7.9	23.9	60.6	0.8	5.6	n.d	98.7	26.85	68.75	4.40	10.3
	7.8	22.9	62.1	0.9	4.9	n.d	98.6	24.11	70.34	5.55	9.1
	7.3	25.2	59.7	0.6	6.7	n.d	99.6	32.27	64.10	3.63	13.3
	7.5	22.5	62.5	1.2	4.9	n.d	98.6	24.53	68.13	7.34	9.5
	8.0	21.9	63.2	1.6	4.0	n.d	98.7	19.68	70.93	9.39	7.3
	7.7	24.7	60.0	0.6	6.2	n.d	99.1	29.67	66.82	3.51	11.7
	7.4	19.7	66.6	2.0	3.0	n.d	98.7	15.91	71.25	12.84	5.9
	7.4	25.0	60.4	0.4	6.6	n.d	99.8	32.20	65.49	2.31	13.0
	7.5	25.1	59.4	0.5	6.8	n.d	99.3	32.56	64.77	2.67	13.3
	7.0	24.7	58.8	0.6	7.3	0.4	98.8	35.17	61.35	3.48	15.2
	7.5	24.4	60.6	0.6	6.1	0.4	99.7	29.99	66.29	3.72	12.0

[1] n.d. indicates FeO was not determined.

[2] Kd values were calculated using the CaO and Na_2O contents of the crystals and coexisting glass.

APPENDIX 2.B (continued)

Sample	Na_2O	Al_2O_3	SiO_2	K_2O	CaO	FeO[1]	total	An	Ab	Or	Kd[2]
11-1	7.1	24.9	56.8	0.3	7.4	0.4	96.9	35.65	62.36	1.99	15.1
	7.3	24.8	58.3	0.4	6.8	0.4	98.0	32.96	64.55	2.48	13.5
	7.5	24.3	59.2	0.4	6.5	0.3	98.2	31.92	65.72	2.36	12.9
	7.0	24.8	57.3	0.4	7.1	0.4	97.1	34.88	62.68	2.43	14.7
	7.3	24.3	58.9	0.7	6.3	0.4	97.9	30.84	65.11	4.05	12.5
12-1	7.4	25.4	59.0	0.3	7.1	n.d	99.2	33.91	64.10	1.98	3.4
	7.3	25.8	58.8	0.3	7.3	n.d	99.6	35.02	63.02	1.96	3.6
	6.3	27.1	56.9	0.2	8.9	n.d	99.5	43.10	55.48	1.42	5.0
	7.4	25.7	59.4	0.3	7.3	n.d	100.2	34.52	63.51	1.96	3.5
	7.7	25.4	59.6	0.4	6.8	n.d	99.8	32.31	65.71	1.98	3.1
	7.1	26.1	58.5	0.3	7.6	n.d	99.6	36.69	61.52	1.78	3.8
12-2	7.2	25.5	59.2	0.3	7.3	n.d	99.5	35.42	62.62	1.97	4.4
	7.5	25.6	59.6	0.3	7.0	n.d	99.9	33.48	64.68	1.84	4.1
	7.5	25.5	59.3	0.3	7.1	n.d	99.8	33.64	64.41	1.95	4.1
	7.1	25.8	58.7	0.3	7.7	n.d	99.7	36.70	61.54	1.76	4.7
	7.3	25.6	59.3	0.4	7.2	n.d	99.9	34.62	63.25	2.13	4.3
	7.5	25.0	59.9	0.4	6.8	n.d	99.5	32.51	65.28	2.22	3.9
	7.1	24.4	57.3	0.3	6.6	n.d	95.8	33.31	64.60	2.09	4.1
	7.1	24.2	58.0	0.4	6.4	n.d	96.0	32.42	65.26	2.32	3.9
	6.8	24.6	57.5	0.4	6.8	n.d	96.2	34.80	63.07	2.13	4.3
	7.1	24.3	58.1	0.4	6.5	n.d	96.4	32.84	64.87	2.29	4.0
	6.3	25.5	56.0	0.3	7.8	n.d	95.9	39.94	58.38	1.67	5.4
	7.2	24.6	58.0	0.4	6.6	n.d	96.8	33.03	64.78	2.20	4.0
	6.9	24.5	57.6	0.4	6.8	n.d	96.2	34.44	63.23	2.33	4.3
	7.1	24.5	57.3	0.3	6.6	n.d	95.9	33.13	64.82	2.05	4.0
	7.1	23.7	58.4	0.5	6.1	n.d	95.8	31.27	65.90	2.83	3.7
12-3	7.4	24.1	57.6	0.4	6.9	0.4	96.8	33.16	64.42	2.42	3.2
	6.7	26.0	58.0	0.3	8.0	0.4	99.3	39.33	58.85	1.82	4.2
	7.4	24.7	58.7	0.4	6.9	0.5	98.6	33.30	64.50	2.20	3.2
	7.3	25.1	57.7	0.4	7.2	0.4	98.1	34.58	63.20	2.22	3.4
13-1	7.2	25.2	59.3	0.4	7.0	0.4	99.5	34.19	63.52	2.29	10.9
	7.3	25.5	60.2	0.4	7.0	0.5	100.9	33.96	63.70	2.34	10.8
	7.9	22.3	62.2	0.8	4.7	0.4	98.3	23.71	71.26	5.02	6.8
	7.3	24.9	58.9	0.4	6.8	0.4	98.8	33.28	64.40	2.32	10.5
	7.5	24.2	58.7	0.5	6.5	0.4	97.7	31.39	65.77	2.84	9.7
	7.1	24.7	57.5	0.4	7.3	0.4	97.3	35.61	62.33	2.06	11.6
	7.9	24.0	59.2	0.5	6.1	0.5	98.2	28.89	68.10	3.01	8.6
	7.3	24.9	59.2	0.4	6.9	0.4	99.1	33.49	64.07	2.45	10.6
13-2	7.6	19.4	65.2	4.3	1.1	n.d	97.5	5.58	68.92	25.50	2.2
	7.6	22.9	61.7	1.5	5.0	n.d	98.7	24.31	67.03	8.65	10.1
	7.5	24.2	60.8	0.9	6.0	n.d	99.4	29.23	65.64	5.13	12.4
	7.4	24.5	60.1	0.9	6.3	n.d	99.1	30.38	64.61	5.01	13.1
	7.2	25.3	59.0	0.6	7.0	n.d	99.1	33.74	62.85	3.42	14.9
	7.9	23.5	61.4	1.2	5.1	n.d	99.1	24.31	68.69	7.00	9.8
	7.4	24.0	60.9	1.1	5.9	n.d	99.3	28.40	65.32	6.27	12.1
	8.2	22.6	62.3	1.7	4.3	n.d	99.1	20.32	70.17	9.51	8.0

[1] n.d. indicates FeO was not determined.

[2] Kd values were calculated using the CaO and Na_2O contents of the crystals and coexisting glass.

APPENDIX 2.B (continued)

Sample	Na_2O	Al_2O_3	SiO_2	K_2O	CaO	FeO[1]	total	An	Ab	Or	Kd[2]
13-2	7.6	24.4	60.0	0.6	6.4	n.d	98.9	30.52	66.16	3.32	12.8
	7.4	24.8	59.4	0.6	6.7	n.d	99.0	32.02	64.28	3.70	13.8
13-3	7.1	23.1	61.7	0.8	5.8	n.d.	98.6	29.63	65.22	5.15	11.9
	7.4	25.0	58.8	0.3	7.3	n.d.	98.9	34.65	63.44	1.91	14.3
	7.3	25.1	59.3	0.5	6.9	n.d.	99.1	33.64	63.70	2.66	13.8
	7.4	24.8	58.9	0.4	6.8	n.d.	98.3	32.73	65.05	2.22	13.2
	7.0	24.2	59.7	0.6	6.9	n.d.	98.4	34.06	62.70	3.24	14.2
	7.7	23.6	61.0	0.6	5.7	n.d.	98.7	28.07	68.27	3.67	10.8
	7.4	24.9	59.5	0.4	6.9	n.d.	99.0	33.29	64.48	2.23	13.5
	7.4	24.8	59.5	0.3	6.9	n.d.	98.9	33.53	64.48	1.99	13.6
	7.3	25.2	58.8	0.4	7.1	n.d.	98.8	34.26	63.69	2.05	14.1
14-1	7.1	25.1	59.0	0.4	7.0	n.d.	98.7	34.44	63.31	2.24	3.8
	7.1	25.4	58.5	0.4	7.2	n.d.	98.5	35.43	62.53	2.05	4.0
	6.9	25.8	58.4	0.4	7.4	n.d.	98.9	36.24	61.52	2.24	4.1
	7.1	25.5	58.7	0.3	7.3	n.d.	99.0	35.59	62.51	1.90	4.0
	7.5	24.8	60.0	0.4	6.5	n.d.	99.1	31.61	65.95	2.45	3.4
	7.1	25.3	59.2	0.3	7.3	n.d.	99.4	35.54	62.45	2.01	4.0
	7.0	25.5	59.3	0.3	7.3	n.d.	99.4	35.81	62.15	2.04	4.0
	7.3	24.9	59.9	0.4	6.8	n.d.	99.2	33.17	64.49	2.33	3.6
14-2	7.2	25.4	59.0	0.4	7.4	n.d.	99.4	35.19	62.67	2.14	4.2
	6.9	24.9	58.3	0.4	7.3	n.d.	97.8	36.08	61.81	2.12	4.3
	7.1	25.6	58.3	0.3	7.5	n.d.	98.9	36.33	61.81	1.85	4.4
	7.4	24.7	59.9	0.4	6.7	n.d.	99.1	32.41	65.26	2.32	3.7
	6.7	25.8	58.4	0.3	7.9	n.d.	99.1	38.43	59.65	1.92	4.8
	7.6	24.3	60.0	0.4	6.2	n.d.	98.6	30.07	67.42	2.51	3.3
	7.3	25.5	58.7	0.4	7.2	n.d.	98.9	34.59	63.35	2.06	4.0
	7.0	24.9	59.2	0.4	7.0	n.d.	98.6	34.45	63.00	2.54	4.1
	7.3	24.8	59.6	0.4	6.9	n.d.	99.0	33.40	64.40	2.20	3.8
	7.0	25.1	58.8	0.4	7.1	n.d.	98.4	35.17	62.20	2.63	4.2
15-1	6.6	25.6	58.6	0.3	8.3	n.d.	99.4	39.99	58.02	1.99	4.7
	6.8	25.9	59.1	0.3	7.7	n.d.	99.8	37.76	60.43	1.81	4.3
	7.1	25.1	59.8	0.4	7.2	n.d.	99.5	34.95	62.91	2.14	3.8
	6.8	25.8	59.1	0.3	7.7	n.d.	99.7	37.62	60.45	1.93	4.2
	7.4	24.8	60.6	0.3	6.8	n.d.	99.9	33.07	64.95	1.98	3.5
	7.0	25.6	59.9	0.4	7.3	n.d.	100.1	35.74	61.97	2.29	3.9
	7.2	25.0	60.1	0.4	7.0	n.d.	99.7	34.04	63.66	2.30	3.7
	7.6	24.5	60.1	0.4	6.6	n.d.	99.3	31.62	65.94	2.44	3.3
	7.7	23.9	61.6	0.5	5.8	n.d.	99.4	28.57	68.74	2.70	2.8
	7.0	25.7	59.4	0.3	7.5	n.d.	99.9	36.63	61.55	1.82	4.1
15-2	7.4	24.7	59.9	0.4	6.6	n.d.	99.1	32.31	65.40	2.29	7.4
	7.7	24.6	59.5	0.4	6.6	n.d.	98.9	31.60	65.88	2.52	7.2
	7.3	25.1	60.2	0.4	6.6	n.d.	99.7	32.34	65.10	2.56	7.4
	7.4	24.4	59.3	0.4	6.4	n.d.	97.9	31.51	66.01	2.48	7.1
	7.3	24.8	59.4	0.4	6.6	n.d.	98.6	32.57	64.91	2.52	7.5
	6.9	25.9	57.7	0.3	7.8	n.d.	98.7	37.88	60.19	1.92	9.4
	7.1	24.3	57.7	0.4	6.6	n.d.	96.0	33.12	64.49	2.39	7.7

[1] n.d. indicates FeO was not determined.

[2] Kd values were calculated using the CaO and Na_2O contents of the crystals and coexisting glass.

APPENDIX 2.B (continued)

Sample	Na_2O	Al_2O_3	SiO_2	K_2O	CaO	FeO[1]	total	An	Ab	Or	Kd[2]
15-3	7.7	24.5	62.2	0.4	6.4	n.d.	101.2	30.73	66.77	2.49	4.8
	7.5	24.8	62.9	0.4	6.7	n.d.	102.3	32.18	65.37	2.45	5.2
	6.9	25.5	61.9	0.3	7.6	n.d.	102.3	37.03	61.06	1.91	6.3
	6.8	25.0	62.0	0.4	7.5	n.d.	101.7	36.87	60.65	2.48	6.4
	7.1	25.5	62.3	0.3	7.6	n.d.	102.7	36.36	61.67	1.97	6.2
	7.6	24.8	62.8	0.4	6.3	n.d.	101.9	30.66	66.87	2.46	4.8
	7.2	24.8	62.2	0.4	6.9	n.d.	101.6	33.89	63.89	2.22	5.6
	7.7	24.5	63.1	0.5	6.2	n.d.	102.0	30.03	67.33	2.64	4.7
	7.8	24.0	64.1	0.5	5.9	n.d.	102.4	28.66	68.42	2.92	4.4
	7.9	23.6	64.6	0.6	5.3	n.d.	102.0	26.17	70.38	3.45	3.9
15-4	7.6	24.5	61.4	0.5	6.3	n.d.	100.2	30.55	66.73	2.71	4.8
	8.0	23.6	62.0	0.5	5.4	n.d.	99.6	26.18	70.72	3.09	3.9
	7.6	23.7	61.5	0.5	6.0	n.d.	99.3	29.63	67.57	2.79	4.6
	7.5	24.4	61.5	0.5	6.4	n.d.	100.3	31.02	66.28	2.71	4.9
	7.8	24.1	62.0	0.5	5.9	n.d.	100.2	28.91	68.37	2.72	4.4
	7.7	23.5	63.2	0.5	5.7	n.d.	100.6	28.17	68.70	3.13	4.3
	8.1	23.9	61.8	0.5	6.0	n.d.	100.3	28.40	68.89	2.72	4.3
	7.6	24.2	61.6	0.4	6.3	n.d.	100.1	30.50	67.25	2.24	4.8
	8.3	23.1	62.5	0.6	5.0	n.d.	99.4	24.25	72.43	3.32	3.5
	7.2	25.4	59.9	0.4	7.4	n.d.	100.3	35.68	62.30	2.02	6.0
	7.4	24.6	60.6	0.4	6.9	n.d.	99.8	33.20	64.61	2.19	5.4
15-5	6.9	25.6	60.3	0.3	7.6	n.d.	100.7	37.36	60.88	1.76	4.6
	7.1	25.3	60.5	0.4	7.3	n.d.	100.6	35.36	62.36	2.28	4.2
	7.0	25.5	60.0	0.4	7.5	n.d.	100.3	36.40	61.47	2.13	4.4
	7.2	25.1	60.1	0.4	6.9	n.d.	99.8	33.94	63.87	2.19	4.0
	6.8	25.5	60.0	0.4	7.0	n.d.	99.9	35.26	62.05	2.69	4.2
	7.0	25.4	59.9	0.4	7.3	n.d.	100.0	35.87	61.98	2.14	4.3
	7.4	25.0	60.7	0.4	6.5	n.d.	100.0	31.93	65.51	2.56	3.6
	7.1	25.4	59.8	0.4	7.2	n.d.	100.0	34.95	62.71	2.34	4.1
	7.3	25.3	60.2	0.4	7.1	n.d.	100.3	34.06	63.78	2.16	4.0
	7.3	25.2	60.4	0.4	7.0	n.d.	100.3	33.75	64.02	2.23	3.9
15-6	7.2	25.4	59.1	0.4	7.3	n.d.	99.4	35.08	62.55	2.37	7.2
	7.2	25.5	59.4	0.4	7.3	n.d.	99.7	35.01	62.97	2.02	7.1
	7.6	24.7	60.4	0.5	6.7	n.d.	99.8	31.84	65.46	2.70	6.2
	7.0	24.0	59.1	0.5	6.7	n.d.	97.3	33.69	63.53	2.78	6.8
	6.5	26.5	57.7	0.3	8.6	n.d.	99.6	41.46	57.06	1.49	9.3
	7.3	25.5	59.4	0.4	7.2	n.d.	99.8	34.50	63.15	2.35	7.0
	7.4	25.0	59.9	0.4	6.9	n.d.	99.5	33.16	64.76	2.08	6.6
	7.2	25.2	59.4	0.4	7.1	n.d.	99.4	34.38	63.08	2.54	7.0
	7.4	24.7	60.5	0.5	6.7	n.d.	99.8	32.47	64.87	2.67	6.4
15-7	7.5	24.5	60.5	0.7	6.0	n.d.	99.3	29.19	66.48	4.33	11.4
	7.3	24.8	58.6	0.5	6.8	n.d.	98.1	32.99	63.88	3.13	13.4
	7.8	24.5	60.3	0.6	6.3	n.d.	99.5	30.11	66.76	3.13	11.7
	8.2	22.8	62.5	1.0	4.9	n.d.	99.5	23.31	70.77	5.92	8.6
	7.9	20.8	64.7	2.4	2.4	n.d.	98.3	12.45	72.75	14.81	4.5
	8.2	22.6	62.6	1.3	4.5	n.d.	99.2	21.59	70.91	7.50	7.9

[1] n.d. indicates FeO was not determined.

[2] Kd values were calculated using the CaO and Na_2O contents of the crystals and coexisting glass.

APPENDIX 2.B (continued)

Sample	Na_2O	Al_2O_3	SiO_2	K_2O	CaO	FeO[1]	total	An	Ab	Or	Kd[2]
15-7	8.1	22.2	63.1	1.3	4.2	n.d.	98.9	20.36	71.80	7.84	7.4
	7.2	25.3	59.4	0.3	7.3	n.d.	99.6	35.07	63.05	1.88	14.5
16-1	7.2	24.7	61.7	0.5	6.6	0.4	101.1	32.78	64.34	2.89	3.5
	7.0	25.5	59.8	0.4	7.4	0.6	100.7	36.11	61.84	2.05	4.0
	7.2	25.3	58.8	0.4	7.4	0.6	99.6	35.37	62.49	2.14	3.9
	6.9	25.5	57.8	0.3	7.7	0.4	98.7	37.30	60.87	1.83	4.2
	7.2	24.9	59.0	0.4	6.8	0.5	98.8	33.75	64.02	2.22	3.6
	7.1	25.1	59.6	0.4	7.1	n.d.	99.3	34.71	63.15	2.14	3.8
	7.4	25.1	60.1	0.4	6.7	n.d.	99.8	32.60	65.15	2.24	3.4
	7.1	25.7	59.1	0.4	7.4	n.d.	99.7	35.81	62.14	2.05	3.9
	7.3	25.2	59.4	0.4	7.1	n.d.	99.4	34.18	63.71	2.12	3.7
	7.3	25.0	60.0	0.4	6.8	n.d.	99.4	33.17	64.42	2.41	3.5
	7.0	25.4	60.0	0.4	6.7	n.d.	99.6	33.80	63.66	2.53	3.6
	6.9	24.0	60.4	0.6	6.4	n.d.	98.3	32.82	63.52	3.66	3.5
	7.1	24.6	60.3	0.5	6.7	n.d.	99.1	33.19	63.72	3.08	3.6
	6.9	25.6	59.0	0.4	7.4	n.d.	99.3	36.37	61.54	2.09	4.0
	7.3	25.1	60.0	0.4	6.7	n.d.	99.5	32.66	65.02	2.32	3.4
16-2	7.3	25.1	59.8	0.4	6.9	0.5	100.0	33.36	64.45	2.19	4.9
	7.5	24.6	58.6	0.4	6.7	0.4	98.2	32.32	65.41	2.27	4.7
	7.3	24.6	58.3	0.4	7.2	0.5	98.2	34.70	63.05	2.25	5.3
	7.1	25.4	58.1	0.3	7.5	0.5	98.9	36.13	61.90	1.97	5.6
	6.5	26.5	58.3	0.3	8.4	0.5	100.5	40.79	57.54	1.68	6.8
	7.0	25.9	59.1	0.3	7.8	n.d.	100.1	37.55	60.76	1.69	5.9
	7.0	25.7	59.5	0.3	7.5	n.d.	100.0	36.52	61.52	1.96	5.7
	6.9	24.9	60.3	0.5	7.0	n.d.	99.7	34.84	62.19	2.97	5.4
	7.2	25.6	59.5	0.3	7.3	n.d.	99.9	35.42	62.60	1.98	5.4
	7.3	25.8	59.2	0.4	7.2	n.d.	99.9	34.64	63.30	2.06	5.2
	7.0	25.6	59.2	0.3	7.2	n.d.	99.5	35.43	62.54	2.04	5.4
	7.6	24.3	61.4	0.5	5.8	n.d.	99.6	28.86	67.92	3.22	4.1
	7.2	25.5	59.1	0.4	7.2	n.d.	99.3	34.60	63.34	2.05	5.2
	7.5	25.0	60.1	0.4	6.6	n.d.	99.5	32.01	65.66	2.33	4.7
17-3	6.9	25.2	58.7	0.4	7.2	0.5	98.9	35.76	62.18	2.06	19.6
	7.0	25.0	59.3	0.5	7.1	0.4	99.3	34.76	62.26	2.98	19.1
	6.6	26.0	56.5	0.3	8.2	0.4	98.0	40.22	57.95	1.83	23.7
	7.2	24.9	58.5	0.4	7.0	0.5	98.4	34.17	63.73	2.10	18.3
	6.5	22.0	63.0	0.7	6.0	0.5	98.6	32.14	63.51	4.36	17.3
18-1	7.7	24.4	59.5	0.4	6.6	0.6	99.1	31.53	66.29	2.17	3.5
	7.1	25.5	59.7	0.4	7.2	0.4	100.2	34.93	62.90	2.17	4.0
	7.8	23.8	59.7	0.5	5.7	0.6	98.1	27.75	69.25	3.01	2.9
	7.3	24.9	58.7	0.4	7.1	0.6	98.9	34.06	63.89	2.05	3.9
	7.5	24.7	59.8	0.4	6.6	0.4	99.4	31.94	65.83	2.23	3.5
	7.2	25.1	59.4	0.4	7.1	0.4	99.6	34.50	63.30	2.20	4.0
	7.3	24.9	58.3	0.4	7.1	0.4	98.5	34.29	63.55	2.16	3.9
	7.4	24.0	58.6	0.4	6.0	n.d.	96.3	30.46	67.13	2.41	3.1
	7.1	24.4	58.0	0.4	6.6	n.d.	96.5	33.32	64.57	2.11	3.5
	7.4	23.8	59.2	0.5	5.6	n.d.	96.5	28.85	68.32	2.83	2.9

[1] n.d. indicates FeO was not determined.

[2] Kd values were calculated using the CaO and Na_2O contents of the crystals and coexisting glass.

APPENDIX 2.B (continued)

Sample	Na_2O	Al_2O_3	SiO_2	K_2O	CaO	FeO[1]	total	An	Ab	Or	Kd[2]
18-1	6.9	24.7	57.4	0.4	6.8	n.d.	96.2	34.35	63.47	2.18	3.7
	7.4	23.9	59.0	0.4	5.9	n.d.	96.6	29.72	67.72	2.56	3.0
	6.8	24.6	57.6	0.3	6.8	n.d.	96.2	35.02	62.87	2.11	3.8
	6.6	25.1	57.0	0.3	7.3	n.d.	96.3	36.96	61.20	1.84	4.1
	7.4	23.9	58.7	0.4	5.9	n.d.	96.4	29.97	67.59	2.43	3.0
	7.2	24.7	57.6	0.3	6.9	n.d.	96.7	34.10	63.95	1.95	3.6
	7.2	24.6	57.8	0.3	6.8	n.d.	96.7	33.62	64.44	1.94	3.5
	6.8	25.1	57.4	0.3	6.8	n.d.	96.5	34.89	63.18	1.92	3.8
18-2	7.3	24.7	55.7	0.4	6.6	n.d.	94.7	32.73	65.21	2.06	6.3
	7.5	24.5	55.7	0.4	6.4	n.d.	94.4	31.23	66.41	2.36	5.9
	7.3	24.9	56.0	0.4	6.7	n.d.	95.3	32.98	64.69	2.32	6.4
	7.3	24.0	56.9	0.4	6.1	n.d.	94.7	30.63	66.78	2.58	5.7
	7.3	24.6	56.0	0.4	6.4	n.d.	94.7	32.19	65.64	2.17	6.1
	6.9	25.2	54.5	0.3	7.3	n.d.	94.2	36.46	61.76	1.78	7.4
18-3	7.5	25.0	60.1	0.4	6.6	n.d.	99.6	32.17	65.64	2.19	11.9
	7.4	24.0	60.6	0.6	6.2	n.d.	98.7	30.57	66.11	3.32	11.2
	7.2	23.5	61.7	0.7	6.0	n.d.	99.2	30.43	65.52	4.04	11.3
18-4	7.1	25.2	59.7	0.4	7.0	n.d.	99.4	34.74	63.06	2.21	4.4
	7.2	25.3	60.0	0.4	7.0	n.d.	99.9	34.45	63.26	2.29	4.4
	7.5	24.4	60.4	0.5	6.2	n.d.	98.9	30.38	66.98	2.64	3.6
	7.4	25.0	60.0	0.4	6.8	n.d.	99.5	32.95	64.90	2.15	4.1
	7.0	25.5	59.8	0.3	7.4	n.d.	100.0	36.33	61.81	1.86	4.7
	7.4	24.7	60.4	0.4	6.6	n.d.	99.5	32.12	65.56	2.32	3.9
	7.1	24.3	60.0	0.4	7.1	n.d.	98.9	34.61	62.92	2.47	4.4
	7.2	24.1	60.6	0.5	6.4	n.d.	98.8	31.91	65.10	2.99	3.9
18-5	7.8	23.8	59.9	0.4	5.6	n.d.	97.5	27.74	69.86	2.39	3.6
	7.6	24.1	59.1	0.5	5.7	n.d.	97.0	28.51	68.74	2.75	3.7
	7.8	23.6	59.9	0.5	5.6	n.d.	97.4	27.43	69.66	2.91	3.5
	6.8	25.6	57.1	0.3	7.5	n.d.	97.3	37.28	60.81	1.91	5.5
	7.7	24.0	59.3	0.5	5.6	n.d.	97.1	27.95	69.16	2.88	3.6
	7.9	23.4	60.2	0.5	5.2	n.d.	97.3	25.92	70.90	3.18	3.3
	6.8	25.5	57.1	0.3	7.4	n.d.	97.2	36.71	61.38	1.91	5.4
	7.3	25.2	56.7	0.4	6.7	n.d.	96.2	33.13	64.63	2.24	4.6
	7.6	23.7	58.5	0.6	5.5	n.d.	95.9	27.73	68.70	3.57	3.6
20-1	7.3	24.1	58.7	0.5	6.5	n.d.	97.0	32.06	65.20	2.74	4.5
	7.5	23.7	58.4	0.4	5.8	n.d.	95.8	29.09	68.26	2.65	3.9
	7.1	25.1	58.6	0.3	7.1	n.d.	98.2	34.88	63.12	2.00	5.1
	7.3	24.6	59.2	0.4	6.4	n.d.	97.9	32.08	65.83	2.09	4.5
	6.9	25.1	57.8	0.3	7.1	n.d.	97.1	35.76	62.38	1.85	5.3
	6.8	24.9	58.3	0.3	7.0	n.d.	97.3	35.38	62.64	1.98	5.2
	6.8	24.6	57.0	0.3	7.0	n.d.	95.6	35.53	62.54	1.93	5.2
	7.0	24.7	58.1	0.3	6.9	n.d.	96.9	34.63	63.45	1.92	5.0
	7.1	24.5	57.9	0.4	6.5	n.d.	96.4	32.92	64.95	2.14	4.6
	6.8	25.0	57.7	0.3	6.9	n.d.	96.7	35.51	62.78	1.71	5.2
	7.6	23.5	58.5	0.4	5.5	n.d.	95.6	27.89	69.43	2.67	3.7
	6.9	24.8	57.7	0.3	6.8	n.d.	96.5	34.71	63.22	2.07	5.0

[1] n.d. indicates FeO was not determined.

[2] Kd values were calculated using the CaO and Na_2O contents of the crystals and coexisting glass.

APPENDIX 2.B (continued)

Sample	Na_2O	Al_2O_3	SiO_2	K_2O	CaO	FeO[1]	total	An	Ab	Or	Kd[2]
20-2	7.1	25.4	60.5	0.4	7.1	n.d.	100.4	34.74	63.00	2.25	3.9
	7.1	25.4	60.9	0.4	7.2	n.d.	100.9	35.19	62.49	2.32	4.0
	7.1	25.3	60.2	0.3	7.4	n.d.	100.4	35.81	62.24	1.95	4.1
	6.5	26.5	59.2	0.3	8.3	n.d.	100.9	40.57	57.88	1.55	4.9
	6.5	26.4	59.1	0.3	8.3	n.d.	100.6	40.60	57.65	1.75	5.0
	6.5	26.4	59.5	0.3	8.4	n.d.	101.1	40.86	57.40	1.75	5.0
	7.1	24.8	60.8	0.5	6.6	n.d.	99.7	32.71	64.52	2.77	3.6
	7.2	25.2	60.1	0.4	7.0	n.d.	99.8	34.15	63.58	2.27	3.8
	7.0	25.8	58.4	0.3	7.6	n.d.	99.2	36.76	61.32	1.93	4.2
20-3	8.5	22.1	63.4	1.1	3.8	n.d.	98.8	18.53	75.10	6.37	3.8
	6.8	19.2	67.4	1.9	3.0	n.d.	98.2	16.89	70.08	13.04	3.7
	7.9	21.4	63.4	1.2	3.9	n.d.	97.8	20.05	72.41	7.54	4.3
	7.4	20.5	65.5	1.6	3.2	n.d.	98.1	17.44	72.49	10.08	3.7
	7.9	21.6	61.5	1.2	4.2	n.d.	96.4	21.07	71.82	7.10	4.5
	8.0	20.8	62.8	1.5	3.2	n.d.	96.3	16.54	74.41	9.05	3.4
	7.0	19.9	66.3	1.6	3.4	n.d.	98.2	18.68	70.43	10.88	4.1
	8.0	21.9	62.6	1.2	3.9	n.d.	97.6	19.79	73.10	7.12	4.2
	7.3	20.9	64.9	1.4	3.8	n.d.	98.5	20.20	70.75	9.05	4.4
	6.9	25.8	56.5	0.4	7.7	n.d.	97.2	37.55	60.37	2.08	9.6
21-1	6.9	24.9	57.4	0.3	6.9	n.d.	96.4	35.11	63.01	1.88	5.6
	6.5	25.7	56.8	0.3	7.9	n.d.	97.1	39.58	58.79	1.63	6.7
	7.2	24.5	58.2	0.3	6.5	n.d.	96.7	32.60	65.40	2.00	5.0
	7.2	24.7	59.5	0.4	6.3	n.d.	98.1	31.96	65.84	2.19	4.8
	7.0	24.6	57.4	0.3	6.8	n.d.	96.1	34.16	64.04	1.80	5.3
	7.0	24.4	57.8	0.4	6.7	n.d.	96.3	33.98	63.87	2.15	5.3
	6.9	23.7	58.9	0.5	6.3	n.d.	96.2	32.43	64.50	3.07	5.0
	6.7	24.6	57.3	0.3	7.0	n.d.	96.0	35.70	62.31	1.99	5.7
	7.1	24.3	57.7	0.3	6.6	n.d.	96.0	33.07	64.87	2.06	5.1
	6.9	25.1	56.6	0.3	7.1	n.d.	96.0	35.72	62.44	1.84	5.7
22-1	7.8	24.0	60.7	0.4	6.1	0.6	99.5	29.61	68.00	2.39	2.3
	7.5	22.9	62.2	0.6	5.6	0.6	99.4	28.15	68.34	3.52	2.2
	7.6	24.0	59.4	0.4	6.2	0.7	98.2	30.09	67.46	2.45	2.3
	7.5	24.7	60.6	0.4	6.6	0.5	100.4	31.80	65.96	2.24	2.5
	7.2	25.4	59.7	0.3	7.0	0.5	100.1	34.13	63.88	1.99	2.8
	7.0	25.5	59.6	0.4	7.4	0.4	100.2	36.05	61.84	2.11	3.1
	7.8	23.0	59.6	0.5	5.6	0.6	97.1	27.63	69.43	2.94	2.1
	7.7	23.9	60.4	0.5	5.9	0.6	98.9	29.05	68.22	2.73	2.2
	7.7	23.1	59.6	0.5	5.8	0.7	97.3	28.28	68.87	2.85	2.2
22-2	8.0	22.5	62.1	0.6	4.8	0.5	98.6	24.17	72.32	3.51	2.5
	8.1	22.4	62.1	0.6	4.8	0.5	98.5	23.66	72.66	3.68	2.4
	8.1	23.0	61.5	0.5	5.1	0.5	98.9	24.98	71.92	3.10	2.6
	8.2	22.2	62.4	0.6	4.7	0.5	98.5	23.12	73.45	3.42	2.3
	8.2	23.1	61.7	0.5	5.1	0.5	99.0	24.88	72.07	3.05	2.5
	7.3	20.2	65.3	1.0	3.7	0.6	98.1	20.60	73.05	6.35	2.1
	8.3	22.5	61.4	0.5	5.1	0.6	98.5	24.57	72.32	3.12	2.5
	7.9	23.1	60.3	0.5	5.7	0.6	98.1	27.88	69.36	2.76	3.0

[1] n.d. indicates FeO was not determined.

[2] Kd values were calculated using the CaO and Na_2O contents of the crystals and coexisting glass.

APPENDIX 2.B (continued)

Sample	Na_2O	Al_2O_3	SiO_2	K_2O	CaO	FeO[1]	total	An	Ab	Or	Kd[2]
22-2	6.3	19.4	65.5	1.1	4.4	0.8	97.5	25.38	66.72	7.90	2.8
23-2	7.0	25.1	57.0	0.3	7.4	0.4	97.1	36.09	62.00	1.90	3.2
	7.0	25.2	56.8	0.3	7.5	0.5	97.2	36.56	61.60	1.84	3.2
	7.0	25.3	58.2	0.3	7.3	0.4	98.6	35.99	62.12	1.90	3.1
	6.9	25.5	57.9	0.3	7.6	0.4	98.6	36.97	61.24	1.79	3.3
BJ3	7.0	24.4	57.9	0.5	6.3	n.d.	96.1	32.10	64.77	3.12	8.7
	7.3	24.3	58.1	0.5	6.0	n.d.	96.2	30.38	66.87	2.75	7.9
	7.3	23.1	59.4	0.7	5.4	n.d.	95.8	27.58	67.92	4.50	7.1

[1] n.d. indicates FeO was not determined.

[2] Kd values were calculated using the CaO and Na_2O contents of the crystals and coexisting glass.

CHAPTER 3.

CRYSTAL SIZE DISTRIBUTION ANALYSIS OF PLAGIOCLASE IN EXPERIMENTALLY DECOMPRESSED HYDROUS RHYODACITE MAGMA

Published in its present form as Brugger, C.R. and Hammer, J.E. (2010) Earth and Planetary Science Letters, 300, 246-254, doi:10.1016/j.epsl.2010.09.046.

ABSTRACT

This study presents crystal size distributions (CSD) of plagioclase forming during decompression experiments of hydrous rhyodacite magma. Samples were annealed at 130 MPa, subjected to continuous decompression at either 2 MPa h^{-1} or 0.5 MPa h^{-1}, and then quenched along their respective decompression paths at ~20 MPa intervals. Samples display concave-up curved CSD plots which result from a combination of two crystal populations: those which formed during the anneal period and those which formed during decompression. The CSDs also display a decrease in crystal number density at 3-7 μm, a size range that is easily resolvable with the imaging strategy employed. The downturn at small sizes is presumably due to insufficient compensation for the intersection probability effect in converting 2D measurements to 3D size distributions. Crystal nucleation and growth rates derived from CSDs using standard assumptions are compared with values obtained using 2D measurements of bulk crystal populations (batch methods). CSD-calculated nucleation rates are substantially low relative to the batch values; in fact, CSD-derived volumetric nucleation rates may underestimate actual nucleation rates by up to two orders of magnitude. In contrast, growth rates from CSDs are consistently higher than batch rates. Although plagioclase growth rates are relatively constant during decompression at a given rate, the average growth rate in the rapidly decompressed series is approximately five times faster than the crystal growth rate in the slowly decompressed series. Because crystal growth rate depends on decompression rate, CSDs are incapable of revealing decompression timescales or magma ascent rates without independent knowledge of crystal growth rate.

INTRODUCTION

Crystal size and number density are intricately linked to the rates of crystal growth and nucleation, which change in response to variations in magma temperature, vapor pressure, and melt composition. Thus, temporally-constrained studies of crystal textures provide insight into magma crystallization kinetics under changing thermobarometric conditions such as those imposed during magma transport, ascent, and eruption. The most commonly used quantitative measure of crystal textures is the crystal size distribution (CSD) technique, initially developed to study industrial crystallization in chemical engineering by Randolph & Larsen (1971), and subsequently popularized for use in magmatic systems by Marsh (1988) and Cashman & Marsh (1988). Although it is possible to adopt any of a variety of models describing the time-, crystal size-, or even melt composition-dependence of crystal growth rate (e.g., Jancic & Garside, 1976; Janse & deJong, 1976; Marsh, 1998; Eberl *et al*., 2002; Kile & Eberl, 2003) in order to extract kinetic information from a CSD, the vast majority of practitioners (e.g., Cashman, 1988, 1992; Hammer *et al*., 1999; Lentz & McSween, 2000; Bindeman, 2003; Cashman & McConnell, 2005; Piochi *et al*., 2005; Resmini, 20007; Armienti, 2008; Blundy & Cashman, 2008; Salisbury *et al*., 2008) assume constant crystal growth rate. This simplifying assumption allows nucleation rate and characteristic crystal size to be extracted directly from the y-intercept and slope, respectively, of a plot of the natural log of the population density (n) versus crystal size (L). Additionally, when magma residence time (τ) is independently known, CSDs may be used to determine crystal growth rates (G). Volcanological applications of CSDs include determining crystal growth mechanisms (Kile *et al*., 2000; Kile & Eberl, 2003), magma cooling rates (Cashman,

1993; Lentz & McSween, 2000; Garrido *et al*., 2001), and the timing of magma mixing events (Higgins, 1996b). CSDs have also been used as evidence to support models of magmatic processes such as polybaric crystallization (Armienti *et al*., 1994), crystal settling (Bindeman, 2003), textural coarsening (Higgins, 1998, 1999; Higgins & Roberge, 2003), and mixing of distinct crystal populations in a batch of magma (Higgins, 1996b; Bindeman, 2003). Recent applications of CSDs have employed fixed growth rates to calculate magma ascent time and/or residence time in a magma chamber (Mangan, 1990; Resmini & Marsh, 1995; Higgins, 1996a; Turner *et al*., 2003; Piochi *et al*., 2005; Noguchi *et al*., 2006; Salisbury *et al*., 2008).

Despite the widespread use of CSDs to answer fundamental questions about volcanic processes, few experimental studies constrain the link between textural measurements and known chemical, thermal, or barometric histories. Several recent experimental studies employing CSD analysis focus on textural development in cooling basalts. Zieg & Lofgren (2006) examine the textural evolution of olivine during continuous cooling of porphyritic olivine chondrules, and Pupier *et al*. (2008) use basaltic cooling experiments to constrain the effects of thermal history on plagioclase CSDs. However, we are unaware of any previous experimental studies of crystallization in silicic magmas that incorporate CSD analysis of crystal population evolution during ascent and decompression.

An important potential contribution of laboratory studies is the ability to constrain the crystallization time scale and thus explicitly determine rates of crystal nucleation and growth. Crystal growth rates have been determined experimentally in three ways: by measuring the largest 4-10 crystals observed in a charge and dividing by experimental

duration (L_{max}; Walker *et al*., 1976; Gardner *et al*., 1998; Lesher *et al*., 1999; Marsh, 1998; Hammer & Rutherford, 2002), by averaging 2D bulk population characteristics (batch method; Hammer & Rutherford, 2002; Couch *et al*., 2003; Larsen, 2005; Blundy & Cashman, 2008; Brugger & Hammer, 2010a), and using *in situ* observations of growing crystals (Means & Park, 1994; Gonde *et al*., 2006; Schiavi *et al*., 2009). A potential concern surrounding this diversity of approaches is that growth rates obtained using these methods may not be suitable for adoption in volcanological studies, which, lacking explicit time information, employ CSD analysis—and myriad assumptions—to interpret magmatic processes. This study is the first attempt to make comparisons between batch calculations commonly used by experimentalists and the CSD calculations widely used in volcanological studies. Batch calculations of plagioclase nucleation and growth rates in experimental samples reported in a previous contribution (Brugger & Hammer, 2010a) are compared with crystallization kinetics extracted from CSDs, analyzed in concert with broadly-applied assumptions. We also evaluate the efficacy of the CSD-based methodology in the specific case of magma ascent rate determination.

METHODS

Decompression Experiments

A complete description of experimental methods is provided in Brugger & Hammer (2010a). In summary, the starting material for decompression experiments consisted of crystal-poor (~2 vol%) rhyodacite pyroclasts from the 3430 years BP caldera-forming ignimbrite of Aniakchak Volcano in the Aleutian Arc. Charges were held at the magma reservoir equilibrium conditions (adopted from Larsen, 2006) of 880°C and 130 MPa for

25-55 hours prior to commencement of decompression. All experiments were run water-saturated with oxygen fugacity held 0.5-1.0 log units above the nickel-nickel oxide solid buffering assemblage using short nickel filler rods and were quenched upon inversion of the vessel. Continuous decompression experiments were run at two different rates, 2 and 0.5 MPa h^{-1}. Six experiments were decompressed at each rate, quenched at progressively decreasing pressures: 109, 87, 68, 45, 26, and 5 MPa (Table 3.1). One sample (2 MPa h^{-1} quenched at 26 MPa) was lost in a polishing mishap and could not be included in the present study.

Table 3.1. Run table and bulk characterization

sample	quench pressure	decompression rate[a]	anneal time (hrs)	decompression time (hrs)	N_A [b] (mm^{-2})	ϕ [b]	L_{max} [b] (mm)
18-3	5	2 MPa hr^{-1}	29	64.9	27126 (6400)	0.256 (0.006)	0.15 (0.06)
18-2	45	2 MPa hr^{-1}	29	44.4	15238 (7800)	0.148 (0.005)	0.11 (0.04)
18-1	68	2 MPa hr^{-1}	29	32.3	223 (118)	0.044 (0.002)	0.085 (0.009)
14-2	87	2 MPa hr^{-1}	26.4	22.4	991 (307)	0.055 (0.004)	0.082 (0.011)
14-1	109	2 MPa hr^{-1}	26.4	10.8	138 (16)	0.034 (0.001)	0.091 (0.007)
13-3	5	0.5 MPa hr^{-1}	55.7	279.30	7029 (593)	0.248 (0.006)	0.12 (0.05)
13-1	26	0.5 MPa hr^{-1}	55.7	230.95	15262 (3924)	0.238 (0.007)	0.13 (0.05)
8-1	45	0.5 MPa hr^{-1}	24.9	197.68	8437 (2541)	0.141 (0.007)	0.097 (0.024)
21-1	68	0.5 MPa hr^{-1}	26.8	144.0	3349 (2100)	0.109 (0.004)	0.089 (0.009)
7-2	87	0.5 MPa hr^{-1}	42.0	99.9	12706 (6100)	0.106 (0.005)	0.098 (0.017)
7-1	109	0.5 MPa hr^{-1}	42.0	48.5	13513 (5564)	0.101 (0.004)	0.072 (0.011)
9-1	130	N/A	24.5	N/A	189 (13)	0.009 (0.003)	0.054 (0.022)

[a] The true decompression rate is slightly faster than the programmed rate shown here.

[b] One sigma error bars given in parentheses.

Batch Textural Characterization

Back-scatter electron (BSE) images (Figure 3.1) were collected from polished thin sections of experimental charges with a JEOL-5900LV scanning electron microscope (SEM) at University of Hawaii Manoa using an acceleration voltage of 15 kV. A total of

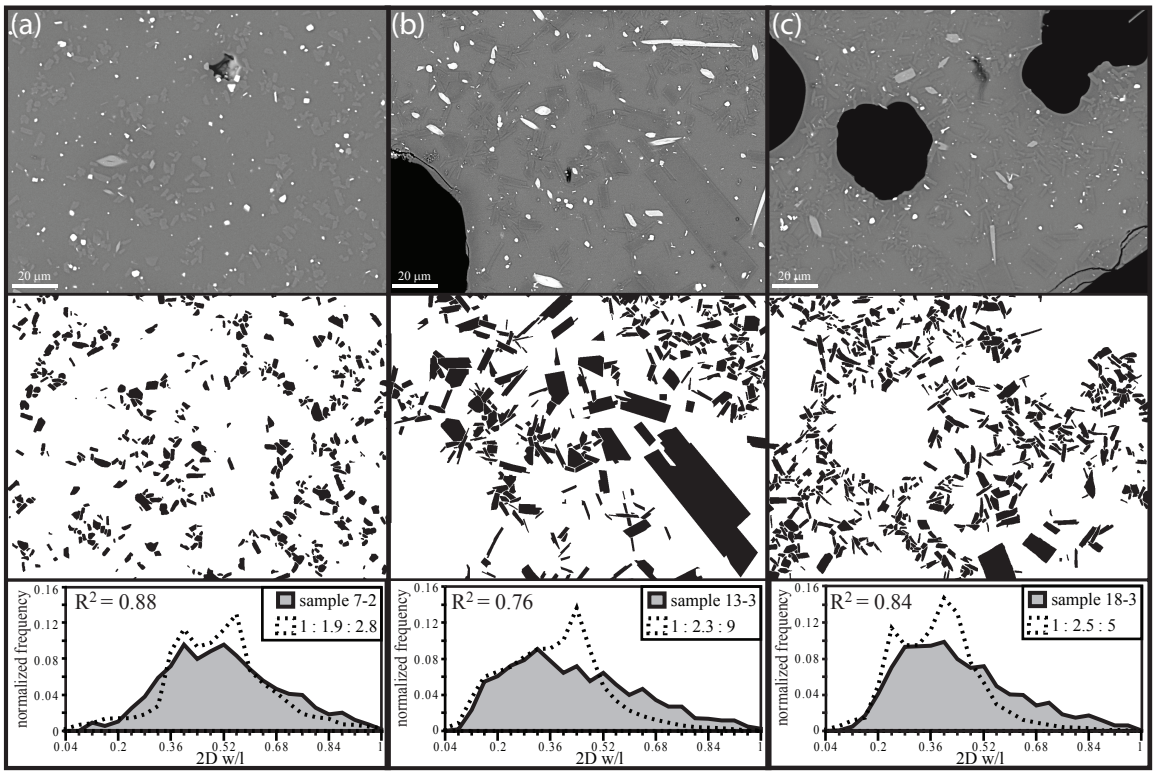

Fig. 3.1. Examples of BSE and binary images from the decompression experiments. Two dimensional width/length distributions for each sample are shown along with their best-fit crystal habit as determined by CSDSlice (Morgan & Jerram, 2006). (a) Sample 7-2 decompressed at 0.5 MPa h^{-1} and quenched at 87 MPa. (b) Sample 13-3 decompressed at 0.5 MPa h^{-1} and quenched at 5 MPa. (c) Sample 18-3 decompressed at 2 MPa hr^{-1} and quenched at 5 MPa.

11-24 BSE images of each sample were obtained at magnifications of 250x and 750x. Plagioclase crystals were manually outlined in these images using Adobe Photoshop, and then converted to binary images (Figure 3.1). The smallest digitized crystals were 3-5 pixels in width/length, corresponding to sub-micron sized crystals. Boundaries between touching crystals were assigned based on visual inspection of crystal shapes. Uncertainty introduced by this method is not considered significant due to the large number of crystals examined (n=342-2688 per sample) and proportionately small number of touching crystals. Unless otherwise noted, measurement uncertainty is depicted in figures and tables using 1σ variation obtained from multiple images, and thus represent sample heterogeneity rather than error associated with the technique. The long and short axes of best-fitting ellipses and the area of 2D crystals were ascertained with ImageJ freeware (NIH; http://rsbweb.nih.gov/ij/).

Plagioclase area fraction (ϕ) and area number density (N_A, mm^{-2}) on a vesicle-free basis were determined by thresholding and counting crystals in each image (e.g., Hammer *et al.*, 1999). Because the samples contain no discernible fabric, the area fraction of plagioclase is equivalent to the volume fraction (Delesse, 1847; DeHoff & Rhines, 1968). Number density and area fraction measurements were then used to calculate a characteristic crystal size,

$$S_N = (\phi / N_A)^{1/2}, \quad \text{Eq. (1)}$$

and volumetric number density,

$$N_V = N_A / S_N \quad \text{Eq. (2)}$$

(Cheng & Lemlich, 1983; Blundy & Cashman, 2008). Batch nucleation rates,

$$I = N_V / t, \quad \text{Eq. (3)}$$

and growth rates,

$$G = S_N / t \,, \qquad \text{Eq. (4)}$$

were calculated using time (t) equal to the decompression interval (e.g., Hammer & Rutherford, 2002; Couch *et al.*, 2003; Larsen, 2005; Blundy & Cashman, 2008). All growth rates cited and calculated in this study involve total crystal length, and are thus double the advance rate of pinacoid faces. The batch methods described above are used extensively in microtextural studies of crystallization kinetics in experimental and natural systems (e.g., Hammer *et al.*, 1999; Hammer & Rutherford, 2002; Couch *et al.*, 2003; Larsen, 2005; Szramek *et al.*, 2006; Blundy & Cashman, 2008; Genareau *et al.*, 2010; Wong & Larsen, 2010). These equations are simple by design and easy to apply, which enables rapid characterization of first order textural parameters and crystallization mechanisms. The strength of their application is in providing a means of comparison among samples in a suite. However, as far as we know, calculations of batch nucleation and growth rates have never been compared to values calculated using CSDs.

Crystal Size Distributions

A limitation of grain sizes measured in thin sections is that the data represent 2D apparent crystal dimensions rather than 3D crystal shapes. Two primary problems with computing 3D values from 2D measurements are the cut-section effect, because a grain is rarely cut exactly through its center and thus one grain can produce different sized sections depending on its orientation, and the intersection-probability effect, arising because a random 2D slice is more likely to intersect a large grain than a small one (Underwood,

1970; Royet, 1991). These problems and stereological solutions are discussed in detail by Saltikov (1967), Peterson (1996), Sahagian & Proussevitch (1998), and Higgins (2000).

The program CSDCorrections (Higgins, 2000) was developed to convert two dimensional intersection data to true three dimensional crystal size distributions by incorporating corrections for the intersection probability effect and cut section effect. Users may upload length, width and area measurements for up to two data sets, which may be necessary if data are collected at two different scales on the same sample. If the volumetric abundance of the phase of interest is assessed independently, then the program can also correct the CSD to the known volume percent (Higgins, 2006). CSDCorrections version 1.39 was used in this study to convert 2D measurements of the long axis of the best fitting ellipse to 3D crystal size distributions on a vesicle-free basis, and except where noted, the volumetric phase abundance correction was used. Logarithmic length intervals were used such that each bin is 1.6 times larger than the next smallest bin. Utilization of CSDCorrections requires estimation of the sample fabric, grain roundness and 3D crystal shapes. Samples were assumed to contain no fabric, which is considered valid because they were subjected to hydrostatic pressure and show no evidence of flow or crystal settling. Based on visual inspection of the samples, a roundness factor of 0.1 was chosen. The 3D shapes of crystals (Table 3.2) were determined using CSDSlice version 5 (Morgan & Jerram, 2006), which compares the distribution of 2D size measurements to a database of shape curves for random sections through 703 different crystal shapes. The program determines a best fit 3D crystal habit based on regression calculations and fitting to the database (e.g., Figure 3.1). The effects

of shape selection on quantitative assessments of crystal volume fraction are considered below in the section titled “Effect of crystal shape on CSDs.”

Table 3.2. Crystal size distribution results

		Crystal Shape		CSD minus overturn		anneal crystals only		dP/dt crystals only			
sample	n[a]	I_d[b]	L_d[b]	slope	intercept	slope	intercept	slope	intercept	ϕ[c]	N_A[d] (mm^{-2})
18-3	2688	2.5	5	-41.7	15.3	-15.4	7.9	-188.5	20.2	0.25(0.03)	21600
18-2	1344	2.5	5	-45.6	15.7	-18.3	8.6	-184.1	19.5	0.17(0.03)	10152
18-1	831	1.8	8	-28.9	12.2	-28.9	12.2	n.a.	n.a.	0.10(0.01)	234
14-2	717	3.6	10	-52.7	14.9	-52.7	14.9	n.a.	n.a.	0.11(0.02)	1053
14-1	342	1.5	3.8	-45.0	12.6	-45.0	12.6	n.a.	n.a.	0.06(0.02)	167
13-3	1340	2.3	9	-21.0	14.0	-12.6	9.8	-63.2	16.7	0.31(0.06)	4653
13-1	2112	2.3	3.6	-51.8	16.1	-20.7	8.9	-197.6	19.7	0.19(0.03)	10814
8-1	836	2.8	4.5	-72.5	16.6	-31.6	10.5	-182.8	18.9	0.13(0.02)	5233
21-1	833	2.7	8	-47.2	15.4	-22.9	11.2	-87.8	16.6	0.12(0.02)	2310
7-2	1327	1.9	2.8	-88.6	16.9	-34.6	10.3	-249.5	19.6	0.13(0.02)	6741
7-1	1361	1.9	2.8	-113.6	16.9	-47.6	11.2	-360.5	20.8	0.10(0.01)	6344

[a] number of crystals measured for CSD analyses.

[b] Crystal shape determined by CSDSlice (Morgan and Jerram, 2006). Short axis=1 for all samples.

[c] Volume fraction and one sigma error given by CSDCorrections (Higgins, 2000). Not corrected to known phase abundance.

[d] Calculated using Eq. 9. CSD was corrected to the known phase abundance. Error cannot be calculated from CSD.

Crystal size distributions are plotted as the number of crystals per unit length per unit volume ($n(L)$; mm^{-4}) as a function of crystal length (L; mm). Linear least-squares regression of ln(n) vs. L was used to calculate slope and intercept values (Table 3.2); crystal growth rates (G) and nucleation rates (I) were calculated using

$$\text{slope} = \frac{-1}{G\tau} \text{ , and} \qquad \text{Eq. (5)}$$

$$\text{intercept} = I/G \qquad \text{Eq. (6)}$$

by assuming constant G (Marsh, 1988; Cashman, 1988; Armienti, 2008). Crystal volume fractions are calculated from the third moment of the crystal population distribution by

incorporating a shape factor to account for the departure of grain shape from a cube (Cashman, 1990; Higgins, 2006; after Marsh, 1988) as

$$\phi = \sigma \sum n_V(L_j) L_j^3 W_j \,, \qquad \text{Eq. (7)}$$

where W_j is the width of interval j, L_j is the length of crystals in interval j, and $n_v(L_j)$ is the number density of crystals in the size interval. The shape factor, σ, is given by

$$\sigma = [1 - \Omega(1 - \pi/6)] I_d S_d / {L_d}^2 \,, \qquad \text{Eq. (8)}$$

where Ω is the roundness factor, which varies from 0 for a rectangular parallelepipeds to 1 for a triaxial ellipsoid (Higgins, 2000), L_d is the long dimension, I_d is the intermediate dimension, and S_d is the short dimension.

For this study we use the most commonly applied assumptions and methods in recent textural studies of natural volcanic rocks (e.g., Piochi *et al*., 2005; Noguchi *et al*., 2006; Toothill *et al*., 2007; Salisbury *et al*., 2008; Field *et al*., 2009; Magee *et al*., 2010; Jerram *et al*., 2009; Mattsson, 2010; Moss *et al*., 2010). Firstly, crystal growth rates are assumed constant during the entire crystallization interval, thus Equations 5 and 6 can be used to calculate plagioclase nucleation and growth rates from the CSDs. Secondly, CSDSlice is used to convert 2D width to length ratios to 3D aspect ratios. Lastly, CSDCorrections is used to generate crystal size distribution plots from 2D crystal lengths. We do not evaluate the validity of these assumptions and methods; rather, our goal is to use the most commonly applied CSD-based methodology to calculate crystal nucleation and growth rates using the known decompression timescales and to make comparisons between these values and those calculated using batch methods.

RESULTS

Nearly all of the experiments in this study produce concave-up curved CSD plots (Figure 3.2). Samples 14-1, 14-2 and 18-1, which were decompressed at 2 MPa h^{-1} and quenched at 109, 87, and 68 MPa respectively, produce nearly straight crystal size distribution plots. The reason for this difference in shape is explained in the context of known crystallization history of these samples (Brugger & Hammer, 2010a; see section "Interpretations of crystal size distribution shapes" below). In addition, all the samples in this study display a CSD decrease at small crystal sizes (~3-7 μm; Figure 3.2). In some cases, this overturn involves only one point and is slight (e.g., samples 14-2 and 18-3), but in other samples there is a larger decrease affecting several size bins (e.g., BJ3, 13-1, 8-1).

DISCUSSION

Effect of Crystal Shape on CSDs

Conversion of 2D crystal measurements into 3D crystal habits requires the assumption that all crystals in a particular sample have the same shape, a key condition that is nevertheless highly unlikely because a typical batch of magma contains crystals that formed at various degrees of undercooling (or effective undercooling), which is known to strongly affect crystal shapes (Lofgren, 1974; Hammer & Rutherford, 2002). To evaluate the effect of shape selection on the resulting CSD, we compare batch estimates of ϕ with CSD-calculated values (Eq. 7, Figure 3.3). As mentioned earlier, CSDCorrections can correct for the volumetric abundance of the phase of interest; however, for evaluative purposes the CSDs shown here are uncorrected. CSD-calculated volume fractions range

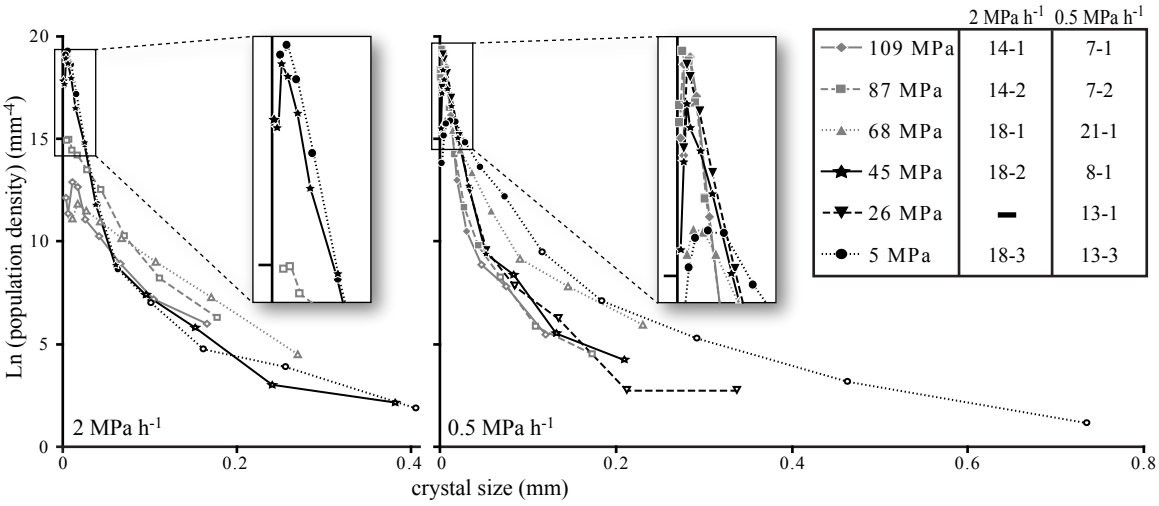

Fig. 3.2. Crystal size distributions calculated using CSDCorrections (Higgins, 2000). The 2 MPa h^{-1} series is on the left, 0.5 MPa h^{-1} series is on the right. For each CSD, samples are divided into two sets of symbols; open symbols represent crystals that formed during the anneal period and closed symbols represent crystals that nucleated during decompression. Three samples (109, 87, and 68 MPa in the 2 MPa hr^{-1} series) contain only anneal crystals (Brugger & Hammer, 2010), because these experiments were shorter than the delay associated with decompression-driven plagioclase nucleation. Sample numbers for all runs are given in the legend.

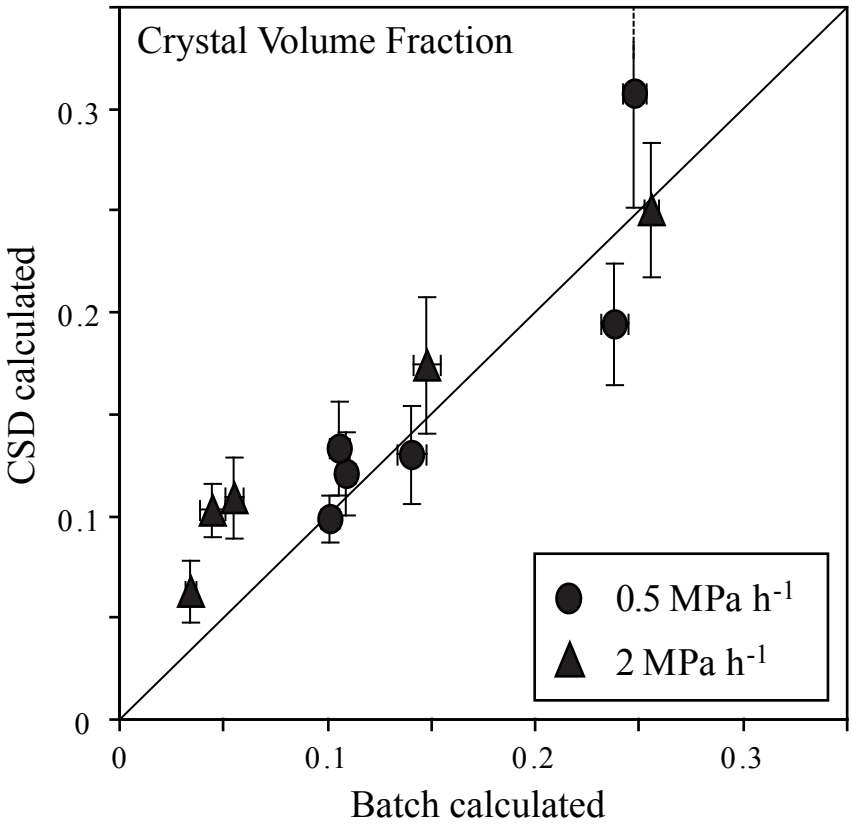

Fig. 3.3. Batch plagioclase volume fraction plotted against values calculated from crystal size distributions. Volume fraction is calculated without the volumetric phase abundance correction. The 2 MPa h^{-1} series are triangles, the 0.5 MPa h^{-1} series are circles. The solid line represents a 1:1 correlation.

from 82 to 232% of the values determined with batch methods, and in all cases, the two methods produce values within 2σ. Batch and CSD-derived data are highly correlated: a line of slope equal to one fits the data with $R^2 = 0.73$. Thus, the crystal shapes ascertained by CSDSlice for the sample distributions and incorporated into the CSD calculations performed by CSDCorrections, adequately recover the known volume fraction of crystals.

Interpretations of Crystal Size Distribution Shapes

The experimental samples have simple, known magmatic histories which are used to interpret crystal size distributions. All samples were annealed at the starting temperature and pressure for 24-55 hours prior to decompression. During this anneal period, a small population of crystals nucleated and grew, as evidenced by experiments quenched immediately following the anneal period (sample 9-1, Table 3.1). Repeat experiments demonstrate constant crystallinity at the end of the anneal period irrespective of anneal times >24 hours. Thus, with respect to crystal volume fraction, all samples reached a steady state prior to commencement of decompression. During decompression, this population of "anneal crystals" continued to grow as shown by the size increase of the largest crystals with progressive decompression (Table 3.1, Figure 3.2). In addition, all experiments decompressed longer than 35 hours contain "decompression crystals" which nucleated and grew after the anneal period. Lack of decompression crystals in the three samples (14-1, 14-2 and 18-1) decompressed for the shortest period of time reveals a lag time for nucleation of new plagioclase crystals (Brugger & Hammer, 2010a).

A first-order feature of nearly all the CSDs obtained here is pronounced upward curvature (Figure 3.2). The known experimental context indicates that this curvature is not a result of changes in the magma cooling rate, crystal aggregation, magma mixing, or textural coarsening, as has been suggested to explain curvature in the CSDs of many natural magmas (e.g., Marsh *et al*., 1991; Armienti *et al*., 1994; Higgins, 1996a, 1998, 1999, 2002; Marsh, 1998; Zieg & Marsh, 2002; Bindeman, 2003; Higgins & Roberge, 2003). Rather, this curvature is an artifact caused by the presence of two populations of crystals, those formed during the anneal period and those formed during decompression, associated with separate nucleation regimes. Consequently, we follow convention (e.g., Cashman, 1988; Armienti *et al*., 1994; Piochi *et al*., 2005; Salisbury *et al*., 2008) and divide our plots into two segments representing the two known crystal populations. Using the growth rate of the largest crystals (L_{max}; see section 4.3 below), the segment of the CSD corresponding to the anneal crystals is determined for each sample (Figure 3.2). When this portion of the CSD is fitted to a separate least squares regression line representing the anneal crystals, the remaining crystals form a fairly well-constrained straight line (R^2 is always >0.97) corresponding to the decompression crystals. The three samples lacking decompression crystals, 14-1, 14-2 and 18-1, contain only one population of crystals and are thus fit with only one regression line.

A population density decrease at small crystal sizes is a ubiquitous feature in all of the samples in this study (Figure 3.2), and is also common in natural samples. An overturn at small sizes in natural rocks is typically interpreted as either a result of ripening (e.g., Congdon *et al*., 1993; Waters & Boudreau, 1996; Higgins, 1998; Higgins & Roberge, 2003; Shea *et al*., 2009), or inadequate spatial resolution (e.g., Cashman &

Ferry, 1988; Resmini & Marsh, 1995; Marsh, 1998; Hammer *et al*., 1999). Neither of these explanations is satisfactory in this case. Ripening is typically associated with very low undercooling and extended time scales (Voorhees, 1992; Cabane *et al*., 2005; Higgins & Roberge, 2007). These samples were decompressed continuously and sustained relatively high effective undercooling (Brugger & Hammer, 2010a), consistent with microtextures characterized by large crystal number densities and rapid growth (Figure 3.1). Thus, it seems unlikely that crystallization was affected significantly by ripening, which redistributes mass from small to larger crystals to minimize crystal-melt interfacial area. Inadequate spatial resolution is also rejected to explain the downturn: at the highest magnification utilized, one micron is represented by 7 pixels and thus submicron crystals are well within detection limits. The fact that the overturn in size frequency occurs in each sample and is not propagated into larger bin sizes for samples undergoing progressive decompression suggests that this is not an authentic characteristic of the CSD. Rather, we infer that it results from intersection probability effects, and if so, indicates that CSDCorrections does not boost small crystal sizes enough to compensate for this stereological problem.

Calculations of Nucleation and Growth Rates

CSD-based determination of 3D nucleation rates (I; Eq. 6) fall significantly below rates calculated using the batch method (Eq. 3; Figure 3.4). When the entire CSD is used to calculate nucleation rates (I), values are 1-2 orders of magnitude lower in all of the samples that contain decompression crystals. However, this is consistent with the largest crystals in each CSD having actually nucleated during the initial anneal period prior to

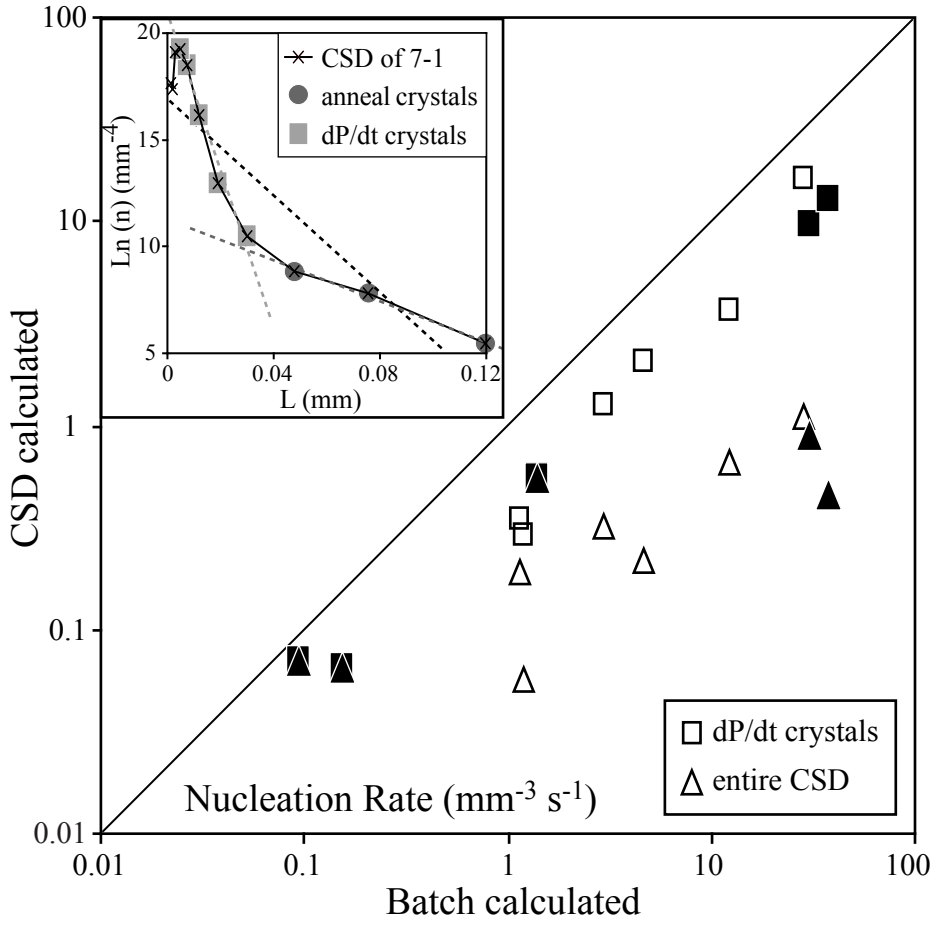

Fig. 3.4. Nucleation rates calculated from CSDs are always less than nucleation rates determined by the batch method. Triangles represent nucleation rates calculated using the entire CSD (minus the overturn at small sizes) and squares represent calculations using only decompression crystals. Open symbols represent the 0.5 MPa h^{-1} series and closed symbols represent the 2 MPa h^{-1} series. Decompression time is used to determine nucleation rates in all samples except the three samples which contain no decompression crystals, anneal time is used instead for these three samples. Inset shows the CSD for sample 7-1 which has been divided into two populations of crystals, anneal crystals (circles) and decompression crystals (squares). The best fit linear regression lines (dashed) are shown for the entire CSD, and the two separate crystal populations.

commencement of decompression. Including these crystals in nucleation rate estimates would tend to artificially lower the calculated rates, because *I* is a function of CSD intercept and slope (Eq. 5 and 6). When nucleation rates are calculated using only the decompression-nucleated crystals (see Figure 3.4 inset for example), estimates increase but are still 30-77% lower than nucleation rates calculated using the batch method.

Plagioclase growth rates are calculated for each sample using crystal size distributions (Eq. 5), the batch method (Eq. 4), and the L_{max} method (Figure 3.5). The L_{max} method always produces the highest growth rates, which range from 2 to 32 times faster than rates calculated with the batch method. When the entire CSD is used, calculated growth rates fall somewhere between the L_{max} and batch methods. However, a large range of growth rates can be generated from one CSD plot by using different parts of the distribution. If the steepest portion of the CSD is used (arbitrarily defined by defined by 3 points), calculated growth rates are quite low and similar to those obtained using the batch method. If however, large crystals from the shallowest part of the CSD are used, calculated growth rates are similar to those of the L_{max} method. The close agreement with bracketing growth rates suggests that image processing time may be saved by using the batch and L_{max} methods, which unlike CSD analysis do not require measuring hundreds of crystals .

Despite small variations in the L_{max} growth rates with progressive decompression, each series maintains a distinct and fairly constant growth rate (Figure 3.6). The average growth rate in the 2 MPa h^{-1} series is approximately five times higher than in the 0.5 MPa h^{-1} series. The two series contain similarly sized crystals, despite representing crystallization time scales that differ by a factor of ~4 (Table 3.1). Thus, crystal sizes

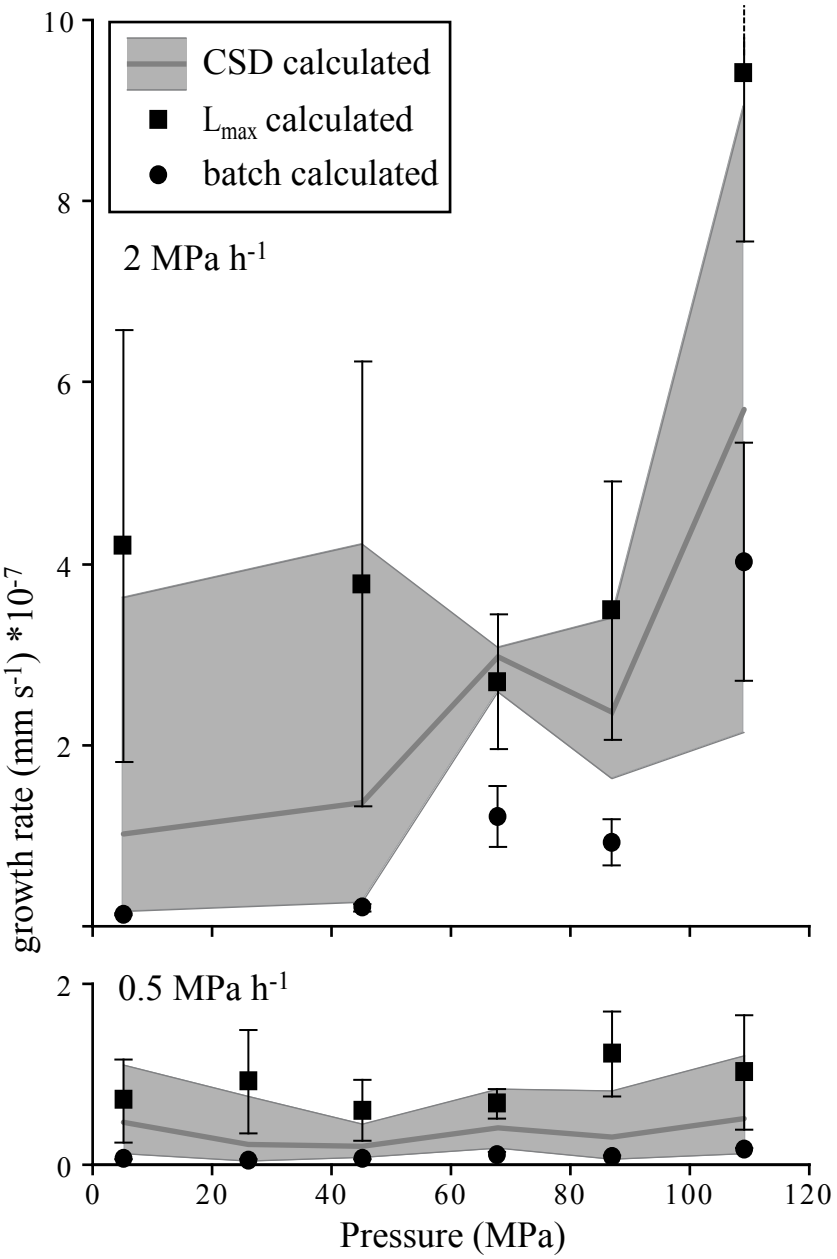

Fig. 3.5. Calculated crystal growth rates; the top boundaries of shaded regions are calculated using the shallowest part of the CSD (as defined by 3 points at the largest bin sizes), while the bottom boundaries are calculated using the steepest part. The solid gray line inside the shaded region represents the calculated growth rate when the entire CSD is used. Crystal growth rates calculated using the L_{max} (squares) and batch (circles) methods are also shown. For each method, the time used to calculate growth rate is decompression time, which starts after the anneal period concludes. However, the largest crystals in each sample (those used in the L_{max} method) likely nucleated during the anneal period. Thus the L_{max} size at the end of the anneal period (sample 9-1) was subtracted from the L_{max} size of each experiment so that the size used in calculations represents only the growth during decompression. Error bars for the L_{max} method reflect propagation of one sigma of the average length of the 5 largest crystals in each sample through the growth rate calculation. In contrast, the one sigma error bars for the batch method reflect sample heterogeneity as assessed from multiple BSE images. Thus, these error bars are not directly comparable because they represent different types of measurement uncertainty.

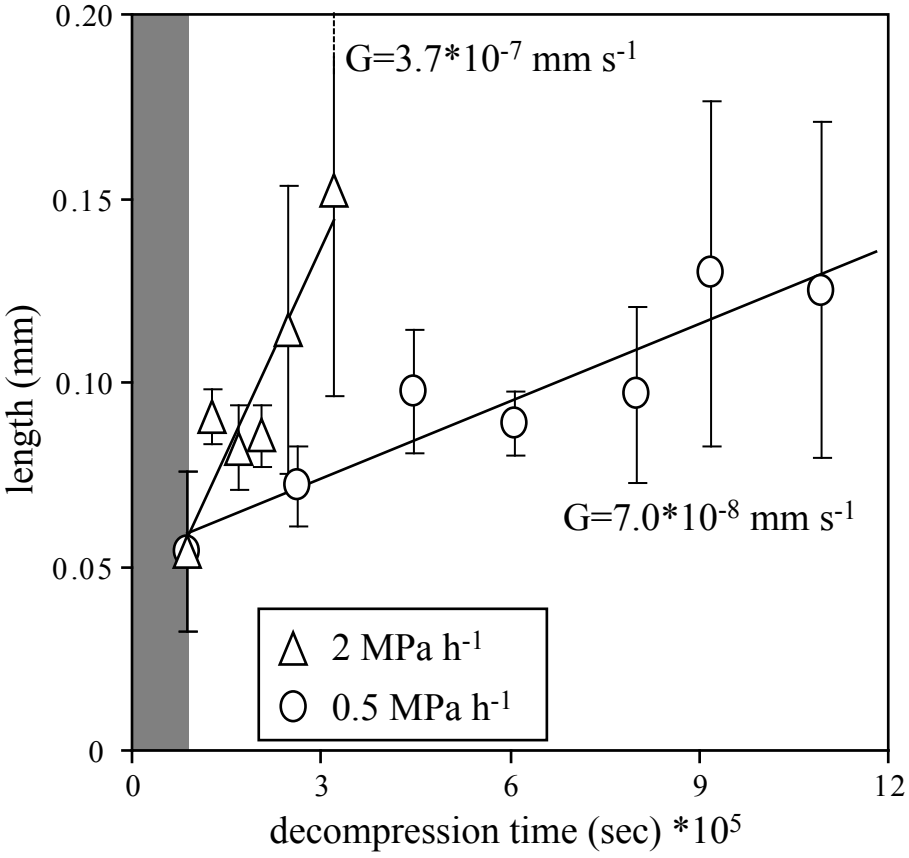

Fig. 3.6. Plot of crystal length (L_{max}) versus decompression time for each series. The average crystal growth rate (G) is determined for each series from the slope of the best-fitting linear relationship between time and length. The shaded zone on the left represents the anneal period which is not included in calculations.

appear to correlate with pressure, and consequently the amount of decompression ($P_{liquidus}$-P_{sample}), rather than the time available for crystallization. Since growth rate is calculated using experiment duration, it appears that growth rates are dependent on decompression rate. Cashman (1993) reports an analogous result for crystals growing in cooling magma: faster cooling produces faster crystal growth. This correlation underscores a key result of this comparative analysis. The practice of using CSD-based methods to calculate magma ascent rates may be fundamentally flawed if crystal growth rates vary as a function of decompression rate, as shown here. The analyst's dilemma is that an accurate ascent rate estimate depends upon adoption of the appropriate crystal growth rate, and yet crystallization time (the product of magma ascent rate and ascent distance) must be known in order to select an appropriate crystal growth rate.

Calculating Magmatic Timescales

In the majority of volcanological studies aimed at determining the timescales of magmatic processes, Eq. 5 is rearranged to solve for τ, the slope of the population distribution is found from the CSD, and a value of crystal growth rate (G) is drawn from the literature. Cashman (1990) suggested that crystal growth rates under most magmatic cooling conditions are fairly uniform between 10^{-9} and 10^{-10} mm s^{-1}, and these rates have been used in conjunction with CSDs to calculate residence times in many volcanic systems (e.g., Mangan, 1990; Resmini & Marsh, 1995; Higgins, 1996a, 1996b; Turner *et al*., 2003; Jerram *et al*., 2003; Sen *et al*., 2006; Higgins & Chandrasekharem, 2007; Higgins & Roberge, 2007; Pappalardo *et al*., 2007; Cigolini *et al*., 2008; Salisbury *et al*., 2008). However, subsequent studies have found that microlite growth rates may be as

high as 10^{-7} to 10^{-6} mm s^{-1} in ascending magmas where crystallization is driven by decompression and water exsolution (Geschwind & Rutherford, 1995; Gardner *et al*., 1998; Hammer *et al*., 1999; Couch *et al*., 2003). Thus plagioclase growth rates in magmatic systems vary over ~5 orders of magnitude. As noted above, computation of magma residence time requires accurate assessment of crystal growth rate. However, five orders of magnitude variation in possible crystal growth rate yields a five order of magnitude range in calculated residence time. So what considerations inform the selection of growth rate to use in CSD-based calculations of residence time?

In reviewing a large number of CSD studies, it appears that crystal growth rates are typically chosen based on contextual information. If crystals are thought to have formed as a result of slow cooling in a magma chamber, regardless of the magma's composition, then slower growth rates in the range of 10^{-8} to 10^{-10} mm s^{-1} are used (e.g., Resmini & Marsh, 1995; Higgins, 1996a, 1996b; Turner *et al*., 2003; Pappalardo *et al*., 2007; Cigolini *et al*., 2008; Salisbury *et al*., 2008; Renzulli *et al*., 2009). If crystals likely resulted from rapid decompression and water exsolution, these crystals are assigned rates between 10^{-6} and 10^{-8} mm s^{-1} (e.g., Piochi *et al*., 2005; Mastrolorenzo & Pappalardo, 2006; Noguchi *et al*., 2006; McCanta *et al*., 2007; Cigolini *et al*., 2008; Salisbury *et al*., 2008; Genareau, 2009).

Using the range of crystal growth rates cited in the literature as potentially appropriate for ascent-driven growth of plagioclase, Equation 5 is used in conjunction with CSD slopes to calculate an estimated "residence time," or decompression duration, for our samples (Figure 3.7). Each of the three growth rates produces a broad, but exclusive field of residence times. As expected, calculated residence time depends on the

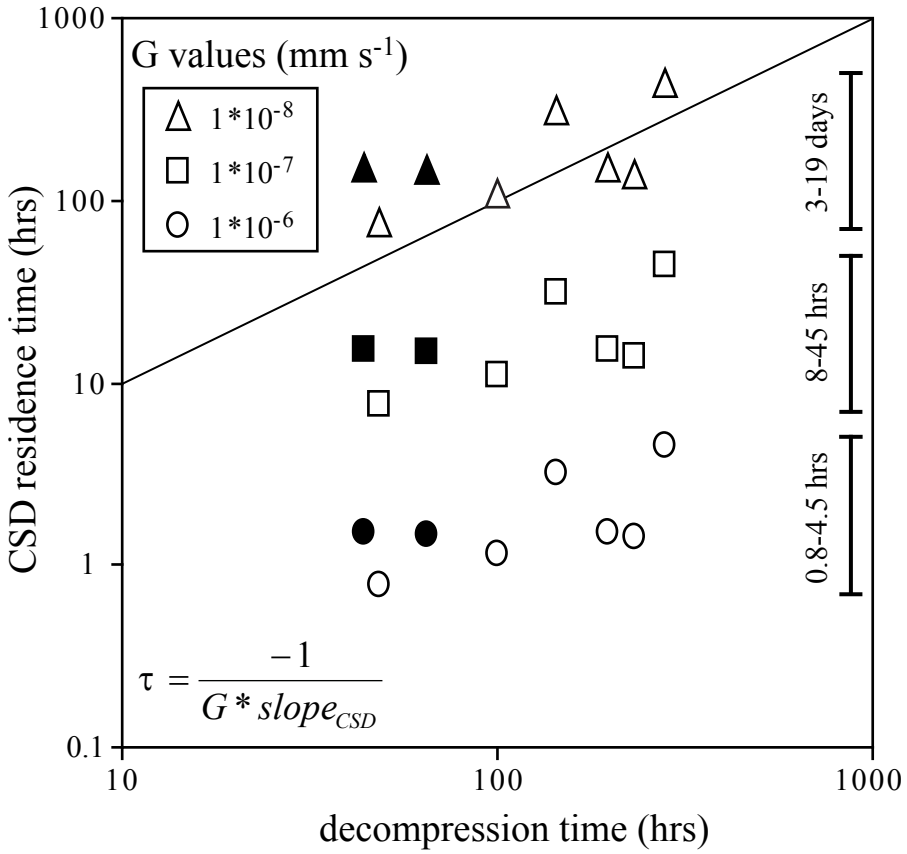

Fig. 3.7. Experimental decompression interval (known crystallization time) versus CSD-calculated "residence" time. Timescales are calculated using Eq. (5) and a range of growth rates previously associated with decompression-induced plagioclase growth: 10^{-6} mm s^{-1} (circles), 10^{-7} mm s^{-1} (squares), and 10^{-8} mm s^{-1} (triangles). The CSD slopes used in the calculations only correspond to the portions of the CSDs representing crystals formed during decompression. The 0.5 MPa h^{-1} series is represented by open symbols, the 2 MPa h^{-1} series is shown with closed symbols (only two points are shown because the other three samples did not contain decompression crystals). The 1:1 correlation line is shown for reference.

selected growth rate. The fastest growth rate generates timescales ranging from 0.8 hours to 4.5 hours, the intermediate growth rate produces timescales of 8-45 hours, and the slowest growth rate leads to magma residence times of 3-19 days. The actual range of timescales for all experiments containing decompression crystals is 1.8-11.6 days, and thus the slowest growth rate generates the most accurate time estimates. However, in studies of natural volcanic rocks the slowest crystal growth rate is selected in a minority of cases (e.g., McCanta *et al*., 2007; Genareau, 2009). The most commonly chosen growth rate for plagioclase in an ascending andesite or dacite is 10^{-7} mm s^{-1} (e.g., Mastrolorenzo & Pappalardo, 2006; Salisbury *et al*., 2008). Adoption of this value for interpretation of crystallization timescale in the experimental samples would underestimate the actual decompression interval by an order of magnitude.

Given the range of growth rates that have been deemed appropriate for syn-eruptive plagioclase microlite crystallization (10^{-6} to 10^{-8} mm s^{-1}), and the wide array of timescales (e.g., <5 hours to nearly 19 days for just one sample) calculated from these rates, the choice of crystal growth rate is clearly of paramount importance for calculating an accurate magma crystallization timescale. We question the efficacy of calculating crystallization time using a growth rate value chosen solely on the inference that the crystals in question grew during decompression. By assuming that a particular population of crystals has formed during magma ascent and picking a corresponding growth rate, the analyst has already constrained the timescale that will result. In other words, the resolution of calculated timescales is a function of the chosen growth rate rather than the microtexture.

CONCLUSIONS

In the earliest CSD studies, crystal growth rates were calculated for systems in which independent knowledge of the crystallization timescales was available (e.g., Cashman 1988; Cashman & Marsh, 1988). After publication of numerous studies involving crystallization in magma chambers, dikes, and lava lakes, Cashman (1990, 1993) concluded that plagioclase growth rates are not particularly sensitive to melt composition (except for extremely low melt viscosities; e.g., Peterson, 1990), and they are approximately constant at 10^{-9} to 10^{-10} mm s^{-1} under most magmatic cooling conditions because most crystallization in shallow volcanic systems occurs at very small effective undercoolings. These conclusions led numerous subsequent authors to employ constant growth rates to calculate magmatic timescales, such as magma chamber residence times, timing of magma mixing events, and cooling rates of lava flows or shallow intrusions (e.g., Mangan, 1990; Resmini & Marsh, 1995; Higgins, 1996a, 1996b; Turner *et al*., 2003; Jerram *et al*., 2003; Sen *et al*., 2006; Higgins & Chandrasekharem, 2007; Higgins & Roberge, 2007; Pappalardo *et al*., 2007; Cigolini *et al*., 2008; Salisbury *et al*., 2008).

Degassing as a driving force for crystallization in H_2O-saturated magmas gained wide acceptance toward the end of the 1990's (Lipman & Banks, 1987; Geschwind & Rutherford, 1995; Gardner *et al*., 1998; Hammer *et al*., 1999). While growth rates may in fact be limited to one order of magnitude variation in shallow volcanic systems where crystallization is driven by cooling (Cashman, 1990), the same does not appear to be true with decompression-induced crystallization. Rather, crystal growth rates during magma ascent can vary over three orders of magnitude and are highly dependent upon decompression rates (Geschwind & Rutherford, 1995; Gardner *et al*., 1998; Hammer *et*

al., 1999; Couch *et al*., 2003). Thus, paradoxically, magma ascent rate and the crystallization timescale must be known before an appropriate growth rate can be chosen for CSD calculations. Consideration of the entire range of plausible decompression-induced crystal growth rates yields variation in the calculated timescales large enough to preclude meaningful volcanological interpretation. Thus, we conclude that crystal size distributions may be used in conjunction with slow crystal growth rates to constrain timescales of long-duration processes, such as magma chamber residence times or lava lake solidification duration, but they are not useful for determining magma ascent rates in the absence of an independent constraint on crystal growth rates.

Experimental studies linking crystal morphologies (e.g., euhedral, swallowtail, hopper, dendritic) with degree of undercooling and decompression rate may be more useful as calibration for estimating magma ascent rates in natural magmas than quantitative CSD-based methods performed in isolation from such textural information. When applied in conjunction with storage chamber depths, such comparisons can be used to calculate crystallization timescales. Moreover, even in systems where the magmatic timescales are known, CSDs may not provide the most efficient method for determining crystal growth rates. We report that CSD-calculated growth rates for the largest crystals in the sample are very similar to growth rates calculated using the L_{max} method. Taking measurements of only the largest crystals in a sample requires a small fraction of the time necessary to quantify the entire population and calculate the CSD. The L_{max} method is suggested as a practical means of obtaining crystal growth rates in instances where timescales are well constrained.

ACKNOWLEDGEMENTS

Thanks to M. May for assistance with image processing. This work was supported by the NSF CAREER program [EAR04-49888 to J.E.H.]. Reviews by B. Marsh and M. Higgins aided tremendously in improving and clarifying the manuscript.

CHAPTER 4.

PREVALENCE OF GROWTH TWINS AMONG ANHEDRAL CRYSTALS REVEALED BY EBSD ANALYSIS

ABSTRACT

This study utilizes electron backscatter diffraction (EBSD) to examine the incipient stages of plagioclase crystallization in hydrous rhyodacite magma. Two experimental samples were investigated, one representing near-equilibrium conditions and the other far-from equilibrium conditions. EBSD investigation affirms a common assumption invoked in textural studies of crystal number density: contiguous crystals with parallel faces are crystallographically continuous, whereas contiguous crystals with non-parallel faces have unrelated internal structures and as such, represent separate crystals. Using EBSD, twinning was identified in approximately 87% of the crystals examined in the highly undercooled sample compared to only 38% in the near-equilibrium sample. This twinning is not the result of deformation, transformation, or synneusis, but rather a result of growth defects introduced during the incipient stages of crystallization. In addition, this study finds that internal structural defects (twins) control macroscopic morphological defects (embayments, swallowtails, and melt inclusions) as a result of the high energy boundary along twin planes. Formation of twins during the incipient stages of plagioclase crystallization is the single most important factor contributing to anhedral morphologies of microlites, and contributes to the development of some plagioclase-hosted melt inclusions.

INTRODUCTION

Motivation

Crystal textures provide insights into processes involved in magma storage and ascent. Metrics such as crystal sizes, shapes, number densities, and spatial distributions or

preferred orientations are used to characterize samples and correlate microtexture with volcanic events (e.g., Cashman, 1990, 1992, 1993; Hammer *et al*., 1999, 2000; Castro *et al*., 2002; Martel & Poussineau, 2007; Genareu *et al*., 2010). As a result of widespread availability and relatively low cost, reflected and transmitted light microscopy are the tools of choice for initial characterization of igneous rock texture. These instruments not only allow rapid assessment of crystal sizes and shapes, but also provide information about a wealth of intra-crystal characteristics such as zoning, twinning, dissolution and overgrowth. In addition, vertical adjustments of stage position allow limited visualizations of crystals and textures in three dimensions (e.g., Castro *et al*., 2002).

In recent decades emphasis has shifted away from phenocrysts and toward examination of microlites (crystals <30 μm) to study the details of magma ascent processes (e.g., Cashman, 1990, 1992; Geschwind & Rutherford, 1995; Hammer *et al*., 1999; Noguchi *et al*., 2006, 2008). The extent of textural data that can be obtained for microlites using petrographic microscopes is very limited because microlites are either too small to resolve or mutually occluded, as they typically occur at high number density. Therefore, scanning electron microscope (SEM) imaging in back-scatter mode has ascended in prominence for studying microlite textures, especially for determining crystal number densities and size distributions (Blundy & Cashman, 2008).

Crystals that form and grow in highly undercooled environments have characteristic morphologies (hopper, skeletal, dendritic, swallowtailed, and irregular), which may hamper quantitative determination of crystal size and number density because these metrics require unambiguous identification of individual crystals. Distinguishing between impinging crystals and a single crystal with anhedral morphology, for example,

can be difficult. Contiguous particles with parallel faces are typically considered to be the anhedral continuations of one crystal and are thus counted as a single grain. In contrast, touching grains with non-parallel faces are considered and counted as separate grains (e.g., Pupier *et al*., 2008; Brugger & Hammer, 2010b). Although widely applied for many years (cf. Hammer *et al*., 1999), this criterion for crystal recognition in textural studies has never been corroborated by independent assessment of the crystallographic orientations of grains. Electron backscatter diffraction (EBSD; see below for details), allows evaluation of this assumption. Using a standard petrographic thin section and SEM, it is possible to map *in situ* three dimensional crystallographic orientations of minerals or portions of minerals as small as 0.5 μm and reliably identify >10° variations in crystallographic orientation in adjacent grains or regions within grains (Prior *et al*., 1999). Thus the EBSD technique adds crystallographic orientation characterization to the arsenal of techniques now routinely used to investigate microlite textures.

In this study we examine the crystallographic structure and orientation of microlites in two experimental samples that formed under known conditions of thermodynamic undercooling with the goal of understanding the early development of crystal morphologies commonly encountered in igneous rocks. Our specific objectives are two-fold: 1) to critically evaluate the assumption that contiguous crystals with non-parallel faces are separate crystals, which is commonly invoked in number density determination, and 2) to examine the relationship between the internal crystallographic structure of plagioclase grains and their external morphologies and evaluate whether anhedral crystals exhibit a higher incidence of internal disorder than do euhedral, faceted crystals (e.g., Welsch *et al*., in review).

Electron Backscatter Diffraction

Electron backscatter diffraction (EBSD) is a technique that allows *in situ* examination of crystallographic orientation of known minerals and identification of unknown phases. The stationary beam of high energy electrons in a scanning electron microscope (SEM) is used to generate backscatter diffraction patterns (EBSPs) on a phosphor screen. To capture some of the backscattered electrons generated within the sample, specimens are tilted within the chamber to a high angle. The high energy electrons, which penetrate the sample to a maximum depth of approximately 2 μm (Prior *et al*., 1999), simultaneously diffract off all lattice planes within the interaction volume. The backscattered electrons escaping from the specimen form a diffraction pattern (Kikuchi pattern) that is imaged on a phosphor screen located adjacent to the sample (Figure 4.1a). In contrast to a transmission electron microscope (TEM) pattern of diffraction spots, an EBSD Kikuchi pattern is a regular arrangement of parallel bright bands (Figure 4.1b). The geometry of Kikuchi bands represent a projection of the internal structure of the crystal lattice onto the flat phosphor screen. Angles between bands represent angles between lattice planes, and the intersections of these bands form bright areas on the screen that represent crystal zone axes.

If the phase of interest is known, the observed Kikuchi pattern can be compared to calculated patterns generated by all possible orientations of that phase. This process, called indexing, determines the three dimensional crystallographic orientation of the analyzed portion of the grain. If the phase of interest is unknown, the Kikuchi pattern gives the symmetry and structure of the mineral. In combination with energy dispersive X-ray spectroscopy (EDS) to constrain an unknown's chemical composition, this

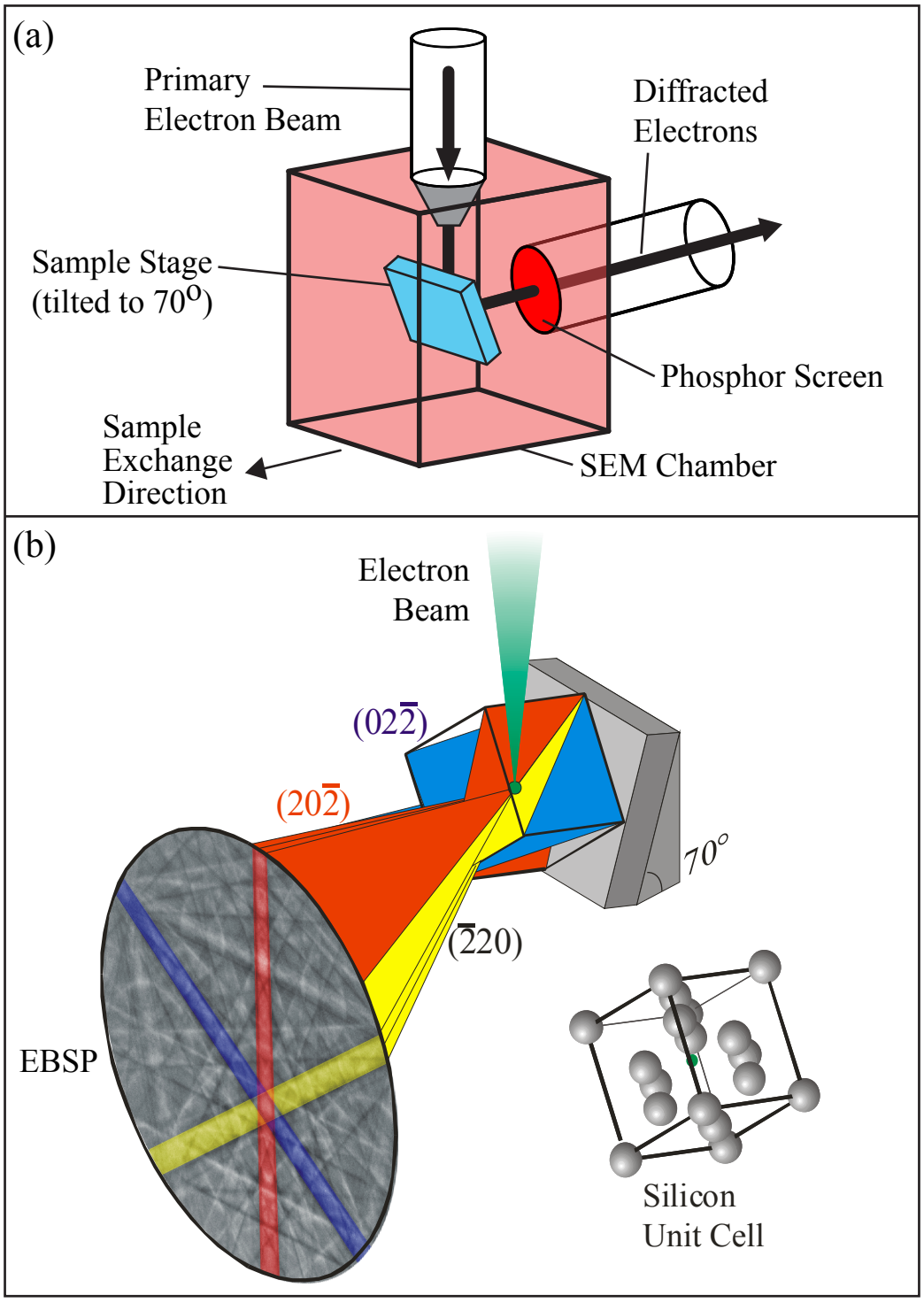

Fig. 4.1. Electron backscatter diffraction (EBSD) set-up. (a) Internal geometry of the sample and phosphor screen inside the University of Hawaii Manoa scanning electron microscope (SEM). (b) Schematic illustration of electron backscatter diffraction pattern (EBSPs) generation. When the electron beam enters the crystal (silicon in this example), electrons diffract off the internal lattice planes (blue, red, and yellow) and form bands on the phosphor screen. (used by permission, from Oxford/HKL Channel 5 user manual).

technique is now used to identify and characterize newly discovered minerals (e.g., Ma & Rossman, 2009; Mikouchi *et al*., 2009). Detailed description of the steps involved in collecting and indexing electron backscatter diffraction patterns (EBSP) are provided in Prior *et al*. (1999) and Schwartz *et al*. (2009).

Electron backscatter diffraction has advantages over x-ray diffraction because the orientation of grains can be determined *in situ* with a focused electron beam, and advantages over TEM because much larger samples can be analyzed. In addition, sample preparation is relatively easy for EBSD. Natural or broken surfaces can be exploited, although polished thin sections are most commonly used (Prior *et al*., 2009). EBSD is also relatively inexpensive in that the detector can be attached to an existing SEM.

While electron backscatter diffraction is only beginning to be exploited by igneous petrologists (e.g., Costa & Chakraborty, 2004), the earliest geological uses of EBSD date back approximately 13 years (Prior *et al*., 2009). Metallurgy and the materials science industry began using EBSD in the late 80's and early 90's to study metals, alloys, ceramics, superconductors and semiconductors. The first commercial EBSD systems were available on the market in 1994 (Schwartz *et al*., 2009). By the late 1990's petrologists began recognizing the uses and geologic applications of EBSD (Prior *et al*., 1999), and since then the number of studies has been steadily increasing (Prior *et al*., 2009). However, most geological applications of EBSD to date are in metamorphic petrology, where EBSD is used to evaluate deformation mechanisms and quantify deformation microstructures (e.g., Boyle *et al*., 1998; Trimby *et al*., 1998; Fliervoet *et al*., 1999; Prior, 1999; Spiess *et al*., 2001; Freitag *et al*., 2004). Recent igneous petrology applications of EBSD include studies of crystal zoning and anisotropic diffusion and

partition coefficients (e.g., Costa & Chakraborty, 2004; Spandler & O'Neill, 2010), examination of epitaxial relationships and heterogeneous nucleation in magmatic minerals (e.g., Hammer *et al*., 2010), and interpretations of deformation structures within magma chambers (Force, 2011). In the future, EBSD may prove useful for understanding the interactions of crystals in flowing media and identification of magmatic flow regimes (Prior *et al*., 1999). EBSD also has potential for contributing to studies of crystallization kinetics, melt inclusion formation, and the fundamental understanding of crystal growth at the incipient stages of crystallization. Petrologists have long relied upon external crystal morphology to make inferences about magmatic processes. We show here that with the aid of EBSD, we can critically evaluate the canonical understanding of links between internal structure and external morphology, and between environmental conditions and crystal defect structure.

METHODS

Sample Selection

This study utilizes two samples, both of which were experimental runs from the suite described in full by Brugger and Hammer (2010a). Each sample has the same bulk composition, rhyodacite from the 3430 yBP eruption of Aniakchak Volcano in Alaska, and each experiment was water-saturated. The first sample (1-3) represents near-equilibrium conditions. This sample was held for 25 hours at the pre-eruptive storage conditions of this rhyodacite magma, 880°C and 130 MPa, as determined by Larsen (2006). All of the crystals in this higher pressure sample are euhedral and characterized by faceted, convex morphologies. The second sample (15-4) was decompressed from 130

to 5 MPa at a rate of 1 MPa hr^{-1} and quenched immediately upon reaching 5 MPa. Comparisons of plagioclase crystal content and glass chemistry between this sample and long duration dwell experiments at four pressures between 87 and 5 MPa indicate an increasing degree of undercooling during decompression (Figures 2.5 and 2.7). Thus, this sample represents a highly supercooled melt with a population of rapidly-formed plagioclase crystals (Brugger & Hammer, 2010a). Euhedral laths are a rarity in this sample. Most grains have anhedral morphologies: irregular faces with irregular indentations, hopper cavities, or swallowtail morphologies. Melt inclusions are also common in these crystals.

EBSD Approach

Chips from each experimental sample were mounted to thin section slides, then ground and polished to a finish appropriate for microprobe analysis following standard abrasion techniques. To obtain clear diffraction patterns, the EBSD technique requires an undisturbed crystal lattice at the sample surface. To remove structurally damaged material left behind by polishing abrasives, samples were subjected to a three-hour final treatment on a Buehler VibroMet® 2 Vibratory Polisher using Buehler Mastermet 2, a non-crystallizing colloidal silica polishing suspension. No electrically conductive coating was applied to the samples as this interferes with the acquisition of EBSPs. After the target crystals were mapped with EBSD, a carbon coat was applied to the surface and BSE (backscatter electron) images of the crystals were acquired.

Electron Backscatter Diffraction (EBSD) maps (e.g., Figure 4.2) were generated on the JEOL 5900LV Scanning Electron Microscope (SEM) at the University of Hawaii

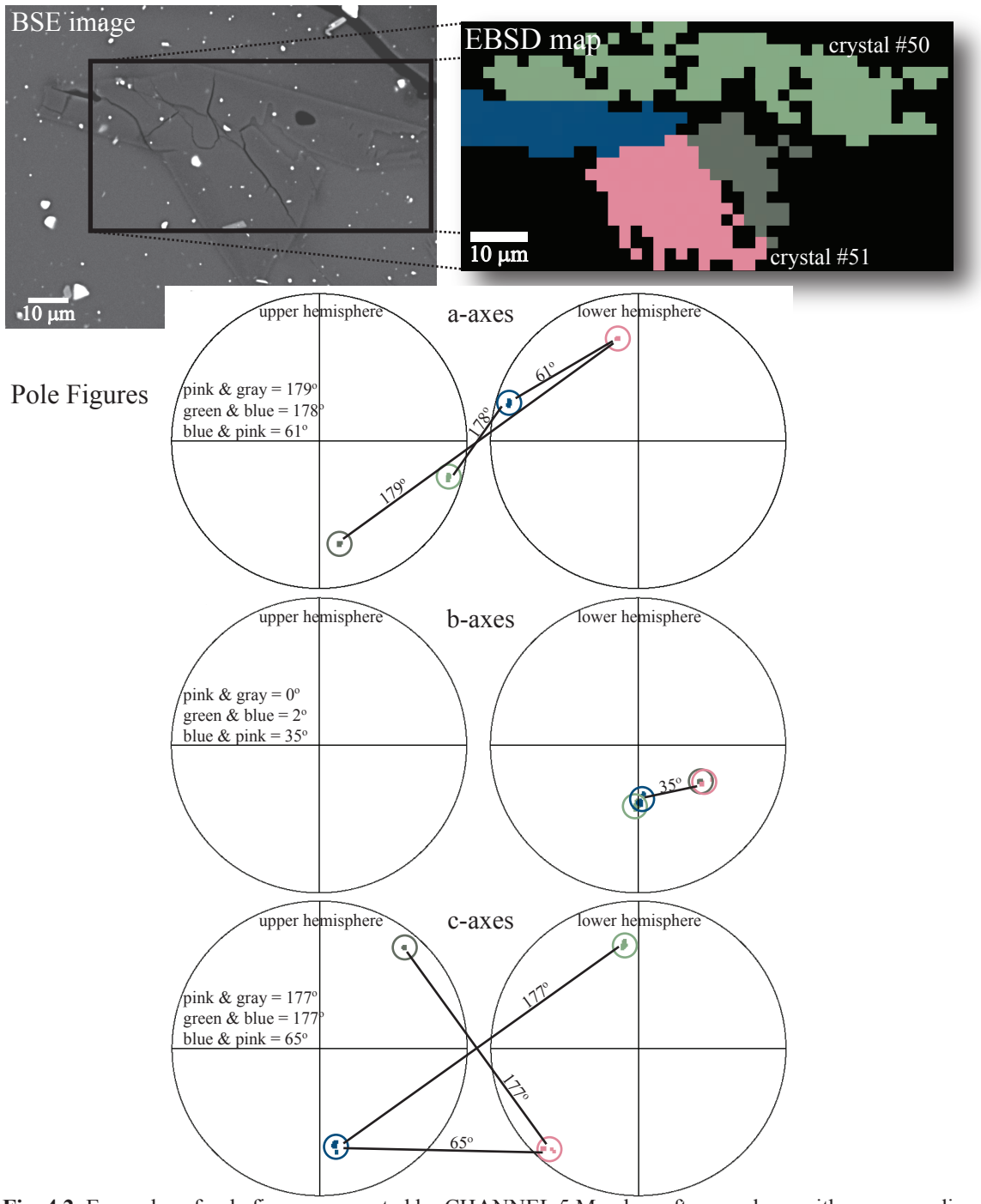

Fig. 4.2. Examples of pole figures generated by CHANNEL 5 Mambo software, along with corresponding EBSD map and BSE image. Each color in the map respresents a different crystallographic orientation, which is keyed to the corresponding colored pixels in the pole figures. Within each colored region on the EBSD map there are slight variations in orientation, thus pole figures contain clusters of similarly colored dots (circled) rather than a single point. Each pair of pole figures represents the upper (left) and lower (right) hemisphere for the a-axes (top), b-axes (middle), and c-axes (bottom). Because plagioclase is triclinic, there is only one pole for each crystallographic direction (i.e. the positive and negative directions are distinct). Angular relationships between poles is assessed with the measurement tool (represented by black lines connecting clusters of colored dots). The relationship between the pink and gray regions is: a-axis=179°, b-axis=0°, c-axis=177°, which represents a pericline twin relationship. The same relationship exists between the blue and green regions. However, there is no twin relationship that matches the angular relationships between the blue+green and pink+gray crystals.

Manoa utilizing a Nordlys Detector from Oxford Instruments and the HKL CHANNEL 5 acquisition software Flamenco. To prevent electrical charging on the sample surface the SEM was operated at low vacuum pressure (15 Pa). Samples were tilted to 70° to maximize exposure of the phosphor screen to the back-scattered electrons generated within the sample. EBSD patterns were collected with an accelerating voltage of 15 keV, a spot size of 70, working distances of 13-16 mm, 4x4 binning, and high gain (Appendix 4.A). These parameters were determined by trial and error to optimize pattern quality and acquisition time in mapping mode.

In the higher pressure sample, mapped crystals ranged in size from 40-340 microns in length, while mapped crystals in the lower pressure sample were 20-120 μm long. Due to the small size of crystals and the relative abundance of glass and vesicles between grains, separate maps were created for individual feldspar crystals or groups of crystals rather than mapping the entire sample. Because small areas of the sample were mapped individually, it was not necessary to apply a correction factor to minimize distortion away from the image center. Mapped areas ranged in size from 24x16 microns up to 176x288 μm, and the step size between each analysis ranged from 1-10 μm, depending on the size of the target crystal. In some cases the entire crystal was not mapped, corners or edges of crystals were omitted in some maps in the interest of saving time during mapping and indexing.

It is particularly difficult to index feldspar EBSPs due to the poor pattern quality associated with low-symmetry materials, compared with metals and high-symmetry minerals such as oxides. Therefore, indexing was not automated during mapping. After each map was completed and all EBSPs saved, the first few rows of electron backscatter

patterns (EBSP) were manually indexed to optimize the indexing conditions (number of bands, Hough resolution, and band centers or edges; Appendix 4.A). Once the indexing conditions were optimized, the remaining EBSPs in each EBSD map underwent automated indexing using the Flamenco software from HKL Technology. All samples were indexed with the same "anorthite" match unit from the American Mineralogist Crystal Structure Database (Angel *et al*., 1990) where a = 8.1796 Å, b = 12.8747 Å, c = 14.1720 Å, $\alpha = 93.13°$, $\beta = 115.89°$, $\gamma = 91.24°$, and space group 2. The software computes the mean angular deviation (MAD) between the unknown EBSP and the best-fitting solution as a measure of confidence that the solution is correct. Indexed patterns with MAD-values greater than 1.1 degrees were discarded, although average MAD values were much lower, closer to 0.3-0.7. During a post-processing noise reduction step, all isolated map pixels (EBSPs) with an indexed orientation different from the eight surrounding EBSPs, were removed from the map. If the pixel was surrounded by at least six neighboring pixels with the same orientation, that EBSP was changed to match the surrounding values. If less than six of the neighboring pixels were the same, then the isolated pixel was changed to a zero solution, which appear black in the EBSD maps.

For each electron backscatter diffraction map, pole figures were generated with the HKL CHANNEL 5 program Mambo. Angular relationships between corresponding crystallographic axes in neighboring crystals, or across twin boundaries within crystals, were assessed manually using the measurement tool (e.g., Figure 4.2). Replicate measurements of the same pair of poles indicate measurement errors on the order of ~1-8 degrees.

Twinning

A twin is a symmetrical intergrowth of two or more crystals of the same mineral (Nesse, 2000). The low (triclinic) symmetry of plagioclase means that twin operators are limited to 180° rotations about one of the crystallographic axes, or reflections across crystal faces (Smith, 1974b). Each of the recognized feldspar twin relationships (e.g., Deer *et al*., 1992; page 407) were simulated using SHAPE (version 7.2.3) software (Dowty, 1980a, 2008) and the a, b, and c crystallographic axial lengths and the α, β, and γ angular relationships for the plagioclase match unit (see above) used in indexing (Figure 4.3). In addition, the angular relationships between corresponding crystallographic axes (e.g., a^a) were determined for each twin law (Figure 4.3) by visual examination. Crystal twinning was identified in samples by comparing the angular relationships measured in the CHANNEL 5 pole figure module, Mambo (Figure 4.2), with expected twin relationships determined using SHAPE.

RESULTS

EBSD orientation maps were generated for 16 plagioclase crystals in the higher pressure (130 MPa) sample and 79 crystals in the lower pressure (5 MPa) sample. The higher pressure sample crystallized at conditions near the liquidus and contains very few crystals, thus approximately 95% of all plagioclase crystals longer than 20 microns were mapped. The lower pressure sample contains significantly more crystals, thus the mapped crystals represent ~ 35% of all plagioclase crystals ≥20 μm in length in this sample.

EBSD mapping reveals random single-pixel variations in crystallographic orientation (<5°) across individual grains that likely correspond to slight differences in

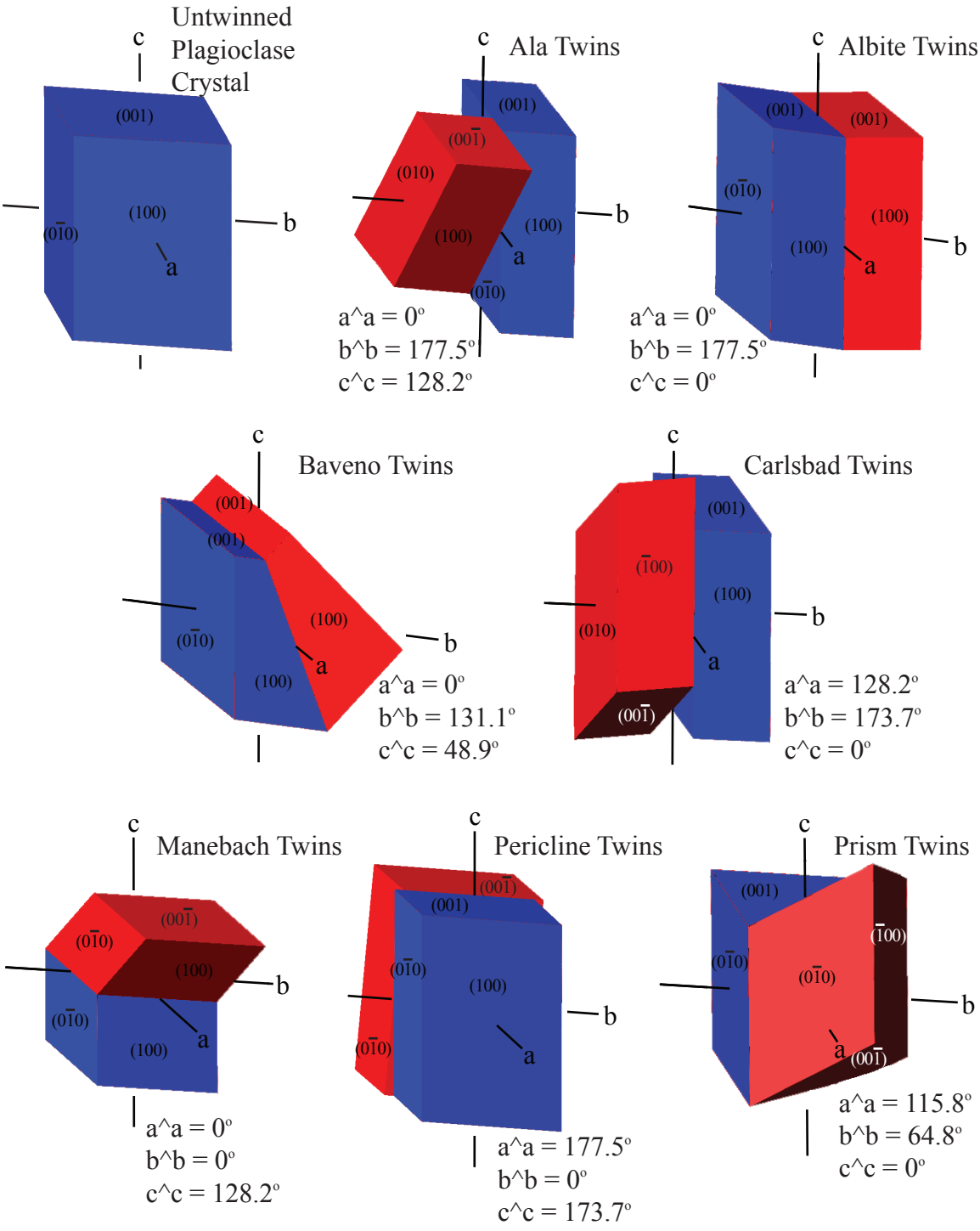

Fig. 4.3. Examples of some of the most common twin laws examined using SHAPE software and the resulting angular relationships between the crystallographic axes of twinned crystals. The blue crystal represents the original crystal and it is in approximately the same orientation in each example (the a-, b-, and c- crystallographic axes shown correspond to the blue crystal only). The red crystal represents the twin that results from the given law. Visible crystal faces are labeled with the appropriate Miller Indicies. Given the two dimensional slices and anhedral morphologies, these particular habits are not likely to be realized in the BSE images. These are models showing only the {100}, {010}, and {001} crystal forms for the specific plagioclase match unit used in this study.

EBSP indexing rather than genuine variations in crystallographic orientation (Prior *et al*., 1999). Mapping also exposes abundant twinning according to common plagioclase twin laws (Figure 4.3), as described in more detail below. Conspicuous by their absence were incremental rotations of the crystal lattice within grains and subgrain boundaries defining small angle lattice misorientation. Such features have been described in igneous crystals having formed by diffusion-limited growth and are associated with dendritic crystal morphologies (Hammer *et al*., 2010; Welsch *et al*., in review).

Crystallographic relationships between contiguous plagioclase crystals

In this study, 35 pairs of contiguous plagioclase crystals with non-parallel faces were examined in the lower pressure sample (Table 4.1); there were no touching crystals to investigate in the higher pressure sample. EBSD orientation mapping reveals that such crystals are unrelated by any twin law (e.g., Figure 4.4a). In contrast, all mapped contiguous crystals with parallel faces (e.g., Figure 4.4b) are related by twin laws.

Twinning

Near-equilibrium sample

In the higher pressure sample, 10 of the 16 (62.5%) mapped crystals contain no twinning. Of the six crystals that are twinned, five display Pericline twinning and one crystal is twinned according to the Ala twin law (Table 4.2 & 4.3, Figure 4.3). Half of the twinned crystals display simple twins, while three of the crystals with pericline twinning contain multiple twins, 2-4 changes in crystallographic orientation across the exposed crystal face.

Table 4.1. Angular relationships between corresponding axes in contiguous non-related crystals in sample 15-4

crystal numbers[a]		a-axis	b-axis	c-axis
1	2	19	30	34
6	7	89	107	77
6	8	100	120	49
9	–	50	8	50
10	11	18	25	13
11	12	30	160	152
15	16	25	40	18
18	19	52	110	120
20	21	84	99	123
26	30	13	164	120
27	75	56	152	152
27	28	3	131	111
27	29	43	168	166
27	30	58	153	158
30	76	64	165	68
31	32	22	33	35
35	36	64	52	70
36	37	8	32	32
38	39	4	61	57
40	41	88	55	80
42	43	151	28	170
42	73	134	121	46
43	73	115	73	148
44	–	8	22	22
45	–	9	25	24
47	48	77	122	44
49	72	81	147	47
50	51	61	35	65
54	55	16	125	116
58	–	135	70	136
61	70	153	148	47
61	62	37	39	44
64	65	31	43	19
66	67	25	55	58
67	68	44	18	44

[a]Mapped crystals were each assigned a unique number. Occasionally, when only a small portion of an adjacent crystal was mapped, it was not assigned a number and was not included as one of the 79 mapped crystals in this study.

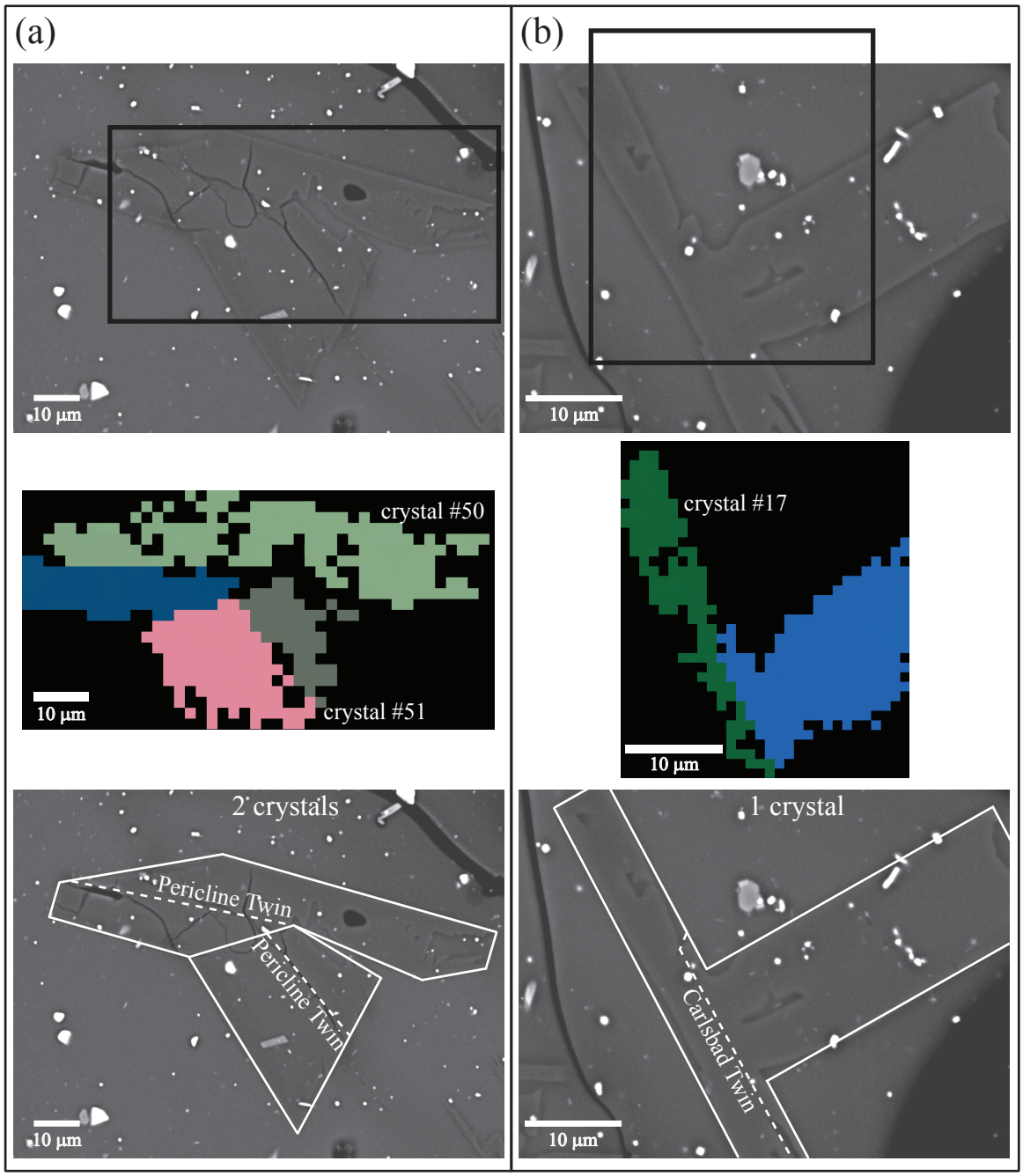

Fig. 4.4. (a) Example of contiguous crystals unrelated by a twin law, but each twinned internally. (b) Example of a twinned crystal that appears to be two laths at a 90 degree angle. Top: BSE images with black boxes representing the area mapped by EBSD. Middle: EBSD maps, each color represents a different crystallographic orientation. The map on the left has a step size of 2 microns, the map on the right has a step size of 1 micron. The crystal numbers correspond to the numbers used in Tables 4.1 and 4.2. Bottom: Interpretation of the crystal(s) based on the EBSD map. Solid white lines outline each crystal, dashed white lines delineate twin boundaries.

Table 4.2. Angular relationships between corresponding axes across twin planes

Sample	Crystal number	Type of twin	a-axes	b-axes	c-axes	simple or multiple twin
1-3	2	pericline twin	179	7	176	simple
1-3	7	Ala twin	0	179	127	simple
1-3	8	pericline twin	179	7	179	multiple
1-3	9	pericline twin	179	7	180	multiple
1-3	10	pericline twin	179	8	178	multiple
1-3	12	pericline twin	178	5	179	simple
15-4	1	carlsbad twin	129	175	0	simple
15-4	2	pericline + carlsbad	52	179	179	multiple
15-4	2	pericline twin	178	7	179	simple
15-4	3	pericline twin	179	2	178	simple
15-4	4	pericline + carlsbad	50	180	180	simple
15-4	4	pericline twin	180	6	180	simple
15-4	4	carlsbad twin	130	174	0	simple
15-4	5	Ala twin	0	180	130	multiple
15-4	6	pericline twin	178	8	179	simple
15-4	6	carlsbad twin	129	174	0	simple
15-4	7	pericline twin	179	7	177	simple
15-4	8	pericline + carlsbad	52	177	178	simple
15-4	8	pericline twin	179	5	178	simple
15-4	9	carlsbad twin	130	180	0	simple
15-4	9	pericline twin	180	3	180	simple
15-4	10	carlsbad twin	129	178	0	simple
15-4	10	pericline twin	179	7	177	simple
15-4	11	pericline + carlsbad	52	175	176	simple
15-4	12	pericline twin	179	4	179	simple
15-4	13	pericline twin	178	0	178	multiple
15-4	14	pericline twin	178	5	178	simple
15-4	14	carlsbad twin	128	175	0	simple
15-4	15	pericline + carlsbad	51	178	179	simple
15-4	16	pericline + carlsbad	51	176	179	simple
15-4	17	carlsbad twin	130	175	0	simple
15-4	18	carlsbad twin	130	175	0	simple
15-4	19	pericline twin	179	3	180	simple
15-4	20	pericline twin	179	5	178	simple
15-4	21	pericline twin	178	8	179	simple
15-4	22	pericline + carlsbad	51	168	180	simple
15-4	22	pericline twin	178	7	178	simple
15-4	23	pericline twin	180	3	180	simple
15-4	24	pericline twin	180	2	180	simple
15-4	25	pericline twin	179	0	178	simple
15-4	26	pericline + carlsbad	51	178	178	simple
15-4	27	pericline twin	178	5	179	simple
15-4	27	carlsbad twin	129	175	0	simple
15-4	28	pericline twin	178	2	176	simple
15-4	28	carlsbad twin	127	174	0	simple
15-4	29	carlsbad twin	128	174	0	simple
15-4	30	pericline + carlsbad	50	176	179	simple

Table 4.2. (continued) Angular relationships between corresponding axes across twin planes

Sample	Crystal number	Type of twin	a-axes	b-axes	c-axes	simple or multiple twin
15-4	31	carlsbad twin	131	175	0	simple
15-4	32	pericline + carlsbad	51	176	179	simple
15-4	32	pericline twin	179	7	179	simple
15-4	33	pericline twin	178	6	180	simple
15-4	34	pericline twin	179	6	179	multiple
15-4	35	carlsbad twin	128	173	0	simple
15-4	36	carlsbad twin	130	174	0	simple
15-4	37	carlsbad twin	130	174	0	simple
15-4	38	pericline twin	178	6	179	simple
15-4	39	pericline twin	178	7	179	simple
15-4	40	pericline twin	179	4	179	simple
15-4	40	carlsbad twin	129	174	0	simple
15-4	41	pericline twin	180	2	178	simple
15-4	41	carlsbad twin	128	179	2	simple
15-4	42	pericline twin	178	2	178	simple
15-4	43	pericline twin	179	7	179	simple
15-4	43	Ala twin	0	178	127	simple
15-4	44	pericline twin	179	0	173	simple
15-4	45	Ala + Pericline	179	179	51	simple
15-4	45	pericline twin	177	0	176	simple
15-4	46	pericline twin	178	0	178	simple
15-4	47	pericline twin	177	6	180	simple
15-4	47	pericline + carlsbad	52	176	180	simple
15-4	48	pericline twin	178	7	179	simple
15-4	49	pericline + carlsbad	51	178	180	simple
15-4	50	pericline twin	178	2	177	simple
15-4	51	pericline twin	179	0	177	simple
15-4	52	pericline twin	179	4	179	simple
15-4	52	carlsbad twin	130	174	0	simple
15-4	52	pericline + carlsbad	51	176	179	simple
15-4	53	pericline twin	179	0	175	simple
15-4	54	carlsbad twin	128	173	0	simple
15-4	55	pericline twin	179	7	180	simple
15-4	56	pericline + carlsbad	51	175	180	simple
15-4	56	pericline twin	179	8	180	simple
15-4	56	pericline twin	178	7	180	simple
15-4	57	pericline twin	178	6	179	multiple
15-4	58	pericline + carlsbad	52	175	179	simple
15-4	58	pericline twin	178	8	179	simple
15-4	59	pericline twin	178	8	178	multiple
15-4	60	pericline twin	178	6	179	simple
15-4	61	carlsbad twin	128	175	0	simple
15-4	62	carlsbad twin	128	173	0	simple
15-4	62	pericline twin	176	5	178	simple
15-4	62	pericline + carlsbad	51	179	179	simple
15-4	63	pericline twin	178	8	177	multiple

Table 4.2. (continued) Angular relationships between corresponding axes across twin planes

Sample	Crystal number	Type of twin	a-axes	b-axes	c-axes	simple or multiple twin
15-4	64	pericline + carlsbad	51	175	180	simple
15-4	65	pericline + carlsbad	51	174	180	simple
15-4	66	pericline + carlsbad	51	177	178	simple
15-4	67	pericline twin	177	7	179	simple
15-4	68	pericline twin	178	0	174	multiple
15-4	69	pericline twin	179	9	179	simple

Table 4.3. Frequency and type of twinning found in each sample

Sample	n[a]	total twinned crystals	Ala twin	Pericline twin	Carlsbad twin	Pericline + Carlsbad	Pericline + Ala
1-3	16	6	1	5	0	0	0
15-4	79	69	2	50	21	19	1

[a] total number of mapped crystals

Highly undercooled sample

Of the 79 mapped crystals in the lower pressure sample, only 10 crystals (13%) are untwinned. Of the 69 crystals that are twinned, 49 display only one type of twinning and 20 contain more than one type (Table 4.2). Pericline and Carlsbad twins are the two most commonly observed twin laws, with 50 and 21 examples of each, respectively (Table 4.3). There are also 19 examples of twinning that involve a combination of the Pericline and the Carlsbad twin laws. In addition, two crystals contain Ala twins and one crystal has a combination Ala-Pericline twin. In natural plagioclase crystals, polysynthetic Albite and Pericline twinning is common (Nesse, 2000). However, in these experimentally produced crystals, no polysynthetic twinning is observable at the resolution of the EBSD mapping. Nearly all the observed twins are simple twins, although nine crystals contain multiple twins which consist of 2-3 changes in orientation across the crystal face. The twin planes are commonly parallel to the crystal faces. Some crystals contain internal defects (holes) that are entirely surrounded by the same crystallographic orientation (Figure 4.5a), but the vast majority of internal and external defects (e.g., hopper cavities and swallowtails, respectively) lie along twin boundaries (Figure 4.5b-f).

DISCUSSION

Type of Twinning

Twinning in plagioclase can be categorized as a result of deformation, transformation, or growth (Buerger, 1945). Carlsbad, Manebach, and Baveno twins are produced only by growth, whereas Pericline and Albite twins can be produced by deformation, transformation, or growth (Nesse, 2000). For the reasons outlined below, we argue that

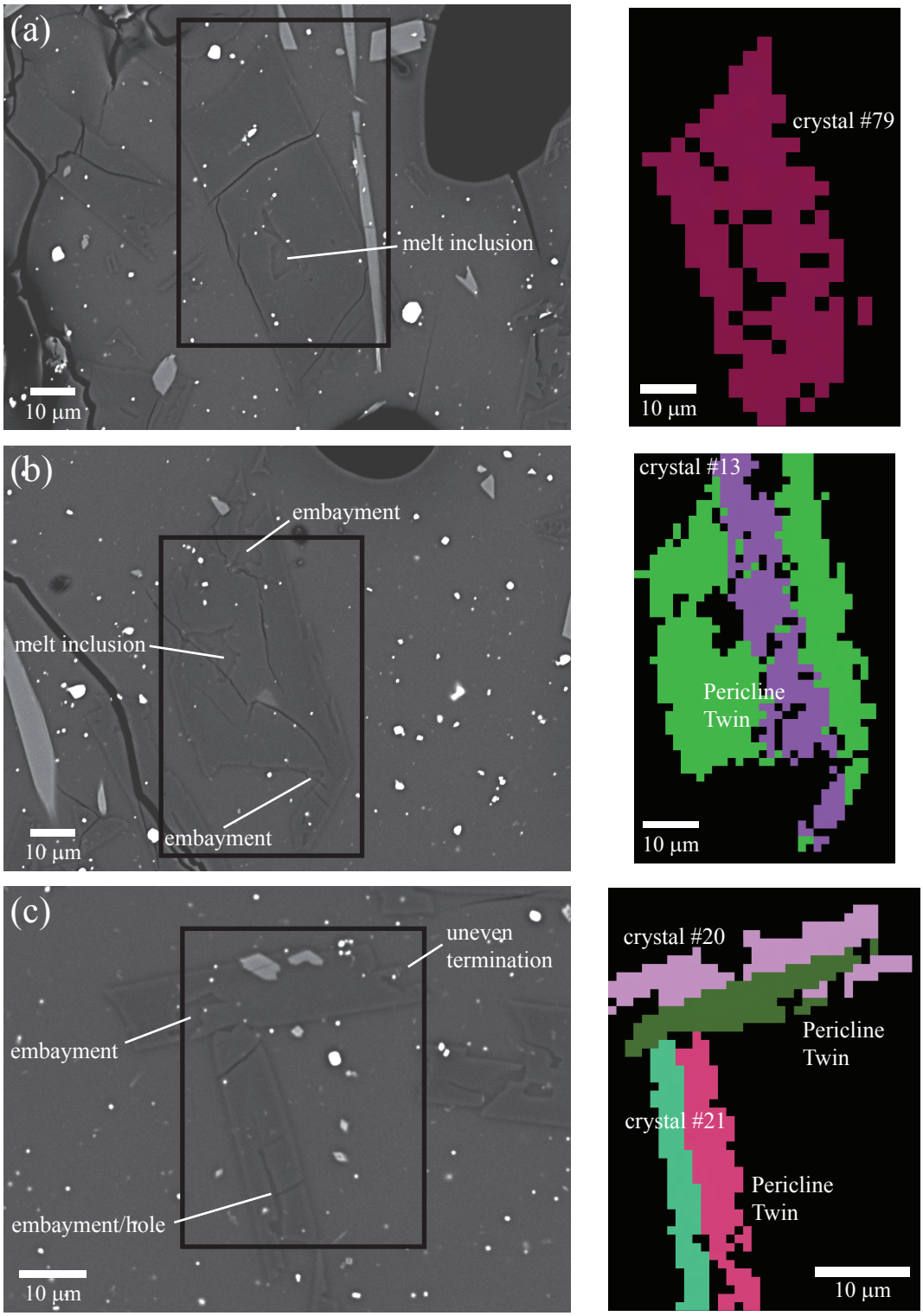

Fig. 4.5. BSE images and corresponding EBSD maps for select grains in sample 15-4. Black boxes in BSE images correspond to the area mapped in the EBSD images. The crystal numbers correspond to the numbers used in Tables 4.1 and 4.2. (a) Morphological defect entirely within one crystallographic orientation. (b-f) Morphological defects (embayments, swallowtails, uneven terminations, and melt inclusions) often lie along twin boundaries, as shown in these images.

(continued)

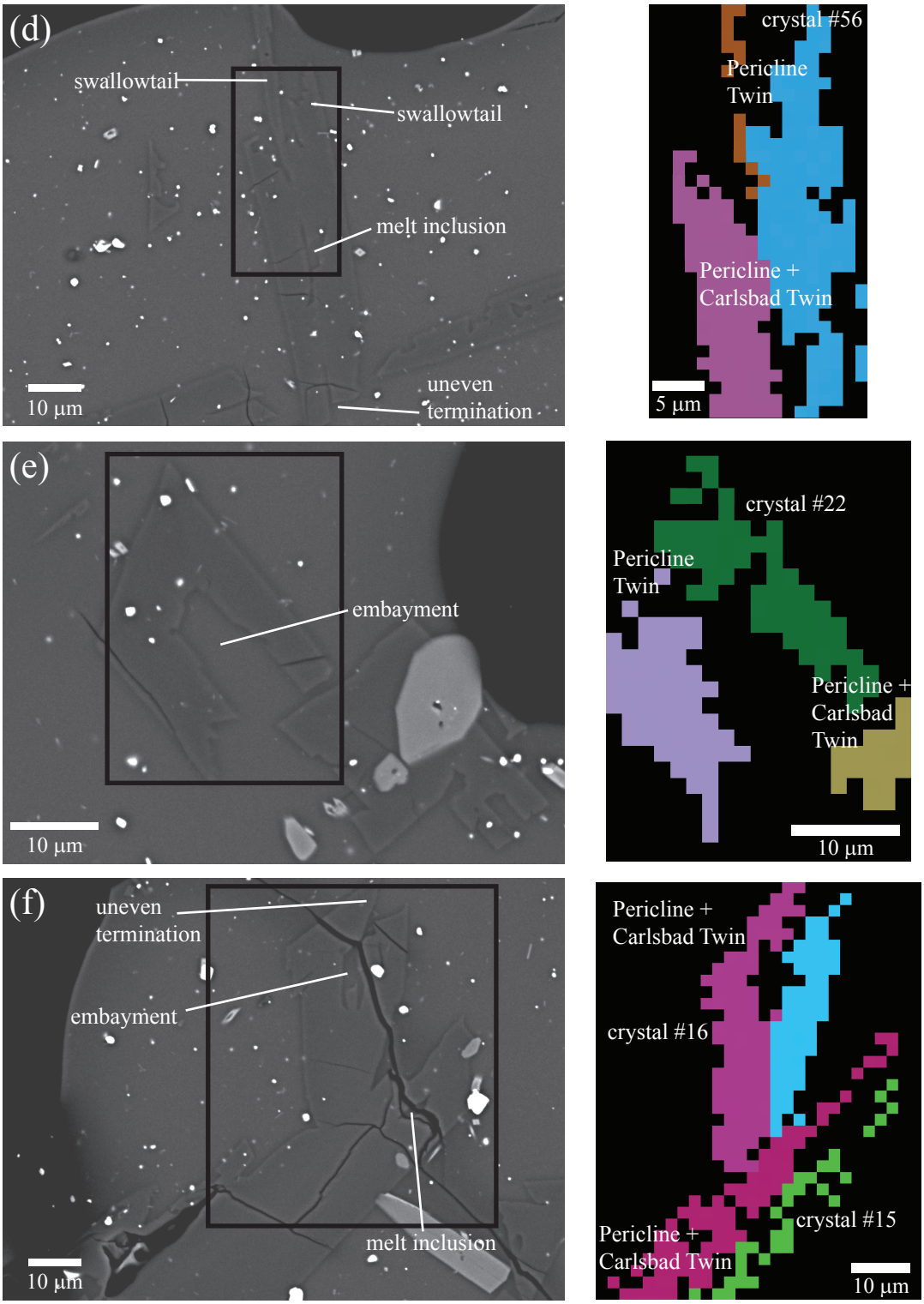

Fig. 4.5. Continued.

all of the twinned crystals in these samples are examples of growth twins. Furthermore, energetic considerations explain the prevalence of twinned crystals in the lower pressure sample and relative scarcity in the higher pressure sample.

Mechanical twinning, also known as deformation or glide twinning, is the result of applied shearing stress (Buerger, 1945) or an external force applied from a preferred direction (Sunagawa, 2005). This stress can result from regional deformation of the rock or by interference of crystals growing in a liquid (Smith, 1974b); however, in plagioclase crystals of intermediate compositions such as our samples (An_{24-33}), production of mechanical twins requires "very large forces" at elevated temperatures (Borg & Handin, 1966; Borg & Heard, 1969; Punin *et al*., 2009). Neither sample displays significant crystal impingement, thus interference of neighboring crystals is not a probable candidate for the formation of twins. Samples in this study were subjected to high pressure during the experiments, however, the external applied stress was equal in all directions and thus did not cause differential strain. Therefore, mechanical twinning is not a likely cause of the twinning in these samples.

Transformation twinning is the result of structural changes that occur when a crystal changes symmetry (Nesse, 2000). The best known example of this is when monoclinic high albite converts to triclinic low albite during cooling. As suggested by Smith (1974b), natural plagioclase will never display transformation twinning because plagioclase in volcanic rocks contains at least 10% calcium and/or potassium and thus never crystallizes with monoclinic symmetry. Pure albite (Ab_{100}) converts from monoclinic to triclinic symmetry at 980°C, and the temperature of this conversion increases as the amount of anorthite (An) and/or orthoclase (Or) increases (Smith,

1974a). For the narrow range of plagioclase compositions found in these samples ($Or_{2.2}Ab_{65}An_{32.8}$ to $Or_{3.3}Ab_{72.4}An_{24.3}$; Brugger & Hammer, 2010a), the monoclinic-triclinic inversion occurs at temperatures above 1100°C at one atmosphere pressure (Figure 7-60 in Smith, 1974a). At the higher pressures (130-5 MPa) used during the synthesis of these crystals, we would expect this inversion temperature to be even higher. The experiments were conducted at a constant temperature of 880°C, and thus significantly below the inversion temperature at all pressures studied. Therefore, the crystals in these samples were always triclinic and the twinning was not caused by monoclinic-triclinic inversion.

Growth twinning is caused by an accidental, yet non-random, misalignment of atoms attaching to a crystalline substrate during growth. This type of twinning typically begins early in the growth history, especially under conditions of supersaturation (Buerger, 1945; Nespolo & Ferraris, 2004; Sunagawa, 2005). During crystal growth, when a new atom or cluster of atoms is added to the crystal face it takes a position that maximizes its coordination with the preexisting atoms and minimizes the surficial free energy of that crystal. However, when the crystal is very small and atoms are rapidly attaching to the crystal face, the chance of errors increases. This type of error during crystal growth is deemed the most likely cause of twinning in the lower pressure sample due to the rapidity of crystal nucleation, short time available for growth, and the high supersaturation.

Crystal growth

Crystallization of a liquid melt is energetically favorable when atoms in the liquid occupy a higher energy state than if those same atoms were part of a solid structure (Nesse, 2000). Atoms or groups of atoms will attach to the surface of a growing crystal in order to minimize the free energy of the system (Nesse, 2000). When this atom or cluster of atoms arrives at the crystal-melt interface, it will assume a position where it is in contact with a maximum number of other atoms (Buerger, 1945). If the atom is the first to arrive at a planar surface, then all locations are equal, and it can attach at any location along the surface in a process called layer nucleation growth (Figure 4.6a). When the next atom attaches, it will assume a position that coordinates with the first atom, which results in more energy loss than occupying a position on the planar surface away from the first atom (Figure 4.6b). Each new atom will attach to the crystal face in an effort to maximize its coordination with preexisting atoms along the crystal-melt margin and minimize the total energy of the crystal (Buerger, 1945). Until a new layer is complete, there is always a corner, or step, in the atomic structure to which new atoms are most attracted because it offers the greatest coordination and greatest energy loss (Cahn, 1954). Thus the process of crystal growth consists of atoms attaching to the old crystal face and spreading across that face until a new layer of atoms covers the old layer.

Energetics of attachment at low effective undercooling

When a natural magmatic melt is near equilibrium, such as sample 1-3, there is a low effective undercooling and a small driving force for crystallization. A small portion of the atoms in the melt have the potential to occupy a lower energy state if they attach to the

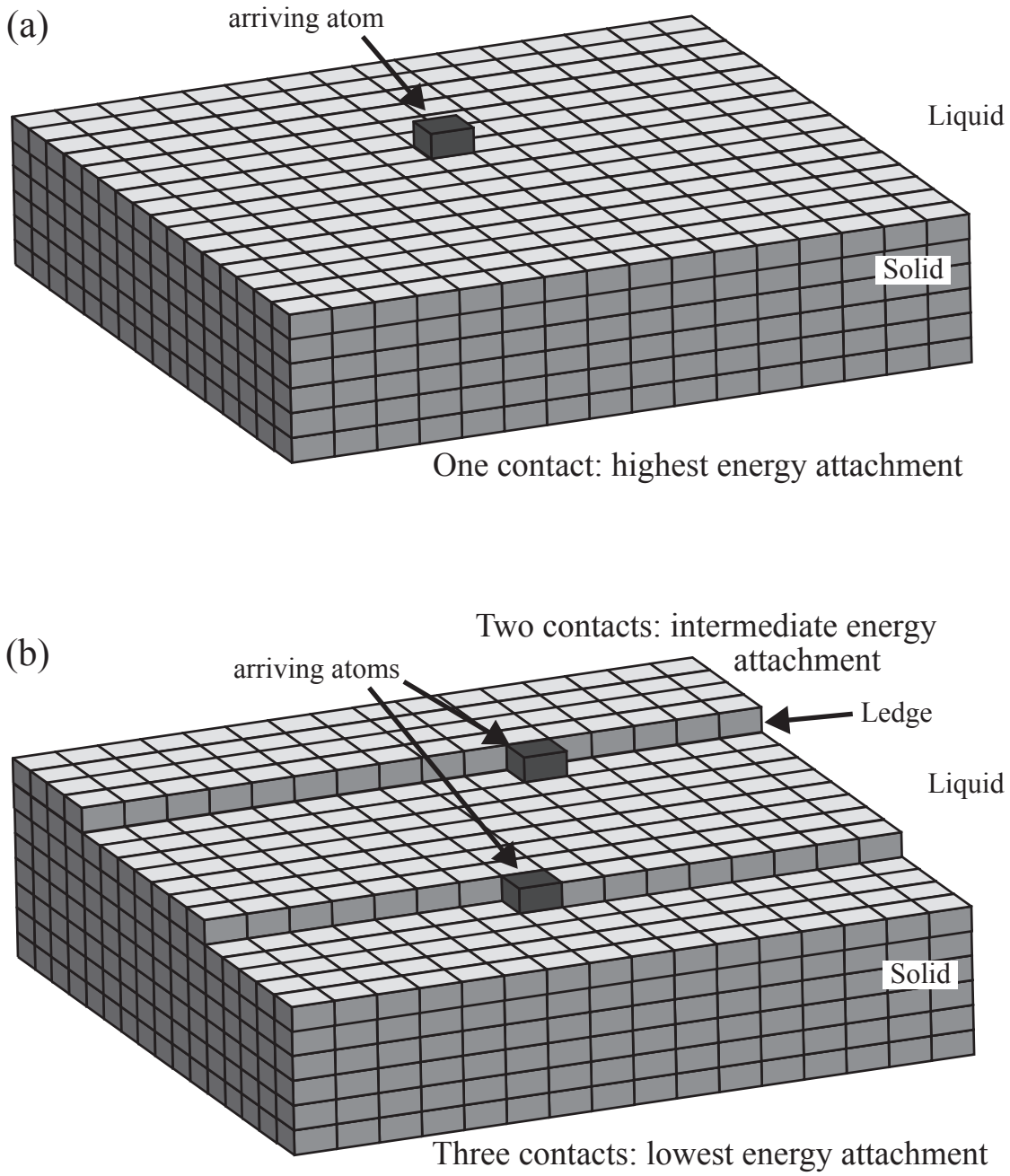

Fig. 4.6. Diagram of layer nucleation growth. Each cube represents an atom or cluster of atoms. (a) When the first atom arrives at a planar crystal face, all positions represent an equal reduction in energy. Thus all positions on the surface are equally probable attachment sites. (b) When there is a ledge or step at the crystal surface, the newly arriving atoms are most attracted to these areas because they offer higher coordination and a greater reduction in energy.

crystal, but once they attach, the resulting change in melt composition may be sufficient to bring the system back to equilibrium. Additional atoms do not attach to the crystal face until there is another perturbation in the system (i.e. a drop in temperature or pressure in a water-saturated melt). This results in a relatively slow rate of atom attachment and correspondingly slow growth rate.

Under near-equilibrium conditions, a new layer of atoms will not start to form until the previous layer is completed across the entire crystal face (Buerger, 1945). Continued growth in this manner results in the formation of planar crystal faces and euhedral crystals. If an atom attaches to the crystal surface in a position that does not continue the normal pattern of the crystal, then it is in a subminimal energy state. Under near-equilibrium conditions, this subminimal energy state may actually be a position of higher energy than in the liquid state. This atom will therefore detach and then reattach in a lower energy position (Buerger, 1945). Thus, at near-equilibrium conditions, the likelihood of growth defects persisting in the crystal structure is quite low. Since growth twinning is an example of such a defect, it follows that crystal growth at low effective undercooling should rarely result in the formation of twinned crystals, which is consistent with the results of this study (Table 4.3).

Energetics of attachment at high effective undercooling

A magmatic melt far from equilibrium, such as sample 15-4, has a high effective undercooling and a high driving force of crystallization. In contrast to the atom attachment process described above, at high effective undercooling atoms are attaching to the crystal face more rapidly and the difference in energy between the melt and the

crystal is much greater (Porter & Easterling, 1997). Under these conditions, the probability of twin formation increases because there is a higher probability of attachment errors and atoms that adhere to the crystal face in positions of subminimal energy are more likely to remain attached (Buerger, 1945; Cahn, 1954). Although they do not occupy the lowest possible energy state, these atoms are in a lower energy position attached to the crystal than they would be in the melt (Smith, 1974b; Sunagawa, 2005). The higher energy state of the twin compared to the single crystal is offset by the higher driving force of crystallization under high-supersaturation conditions (Sunagawa, 2005). In addition, the rapid movement of additional atoms to the crystal-melt interface may lead to the simultaneous arrival of additional atoms that will improve the coordination and lower the energy of the first misplaced atom, thus increasing the likelihood that a twin will persist (Buerger, 1945; Nespolo & Ferraris, 2004).

Another factor that may contribute to the formation of twins at high effective undercooling is the structure of the melt itself. Classical nucleation theory suggests that highly undercooled melts contain more clusters of atoms than melts near equilibrium, and each cluster is composed of a larger number of atoms (Porter & Easterling, 1997; Kelton, 2004). Thus, if a cluster of atoms in such a melt arrives at the crystal surface in a twin position, the twin is more likely to persist because the atoms are already coordinated with one another (Buerger, 1945).

The formation of growth twins is most likely to occur during the earliest nucleation stages of crystallization (Buerger, 1945; Cahn, 1954; Smith, 1974b; Sunagawa, 2005) because there is no preexisting long-range order to act as a template for new atoms. In addition, melt supersaturation is high and the energy of a crystal is

relatively high because it has a large number of unsatisfied bonds compared to its volume. Thus conditions are less unfavorable, and possibly even favorable, to the formation of twins. If a melt reaches and maintains near-equilibrium conditions soon after the nucleation stage, a small twinned crystal with higher energy may dissolve and then reprecipitate on an untwined crystal (Cahn, 1954). However, if the melt continues crystallizing under conditions of supersaturation, as experienced by sample 15-4 during continuous decompression (Brugger & Hammer, 2010a), then continued growth of the twin will persist (Emmons & Gates, 1943; Buerger, 1945). In fact, twinned nuclei have been observed to grow faster than single crystal nuclei once they have become established (Cahn, 1954).

Growth twinning as a result of supersaturation occasionally reoccurs, as evidenced by the presence of some crystals with multiple twin planes. However, the vast majority of crystals in our samples contain simple twins which likely formed as the result of one error during the earliest stages of crystal growth because energetically, this would be the most likely time for an error to occur. Polysynthetic twinning is not present in any of our samples. This is in agreement with previous research which indicates that this type of twinning is not caused by growth, but rather by mechanical deformation or sub-solidus structural inversion during cooling late in the growth history (Emmons & Gates, 1943; Cahn, 1954).

Contribution of Synneusis?

Synneusis refers to the “swimming together” of crystals (Vogt, 1921). In the context of twinning, it has been described as a process by which two crystals suspended in a melt

may float together and join along external faces in a twin orientation (Smith, 1974b; Vance, 1969; Nespolo & Ferraris, 2004). For this process to occur, the crystals must be in an environment that favors their motion and casual interaction so that they may come into random contact (Nespolo & Ferraris, 2004). Occasionally, when two crystals come into casual contact the interatomic forces attracting like faces are sufficient to overcome viscous forces exerted by the liquid, and move or rotate the crystals into structural alignment (Cahn, 1954; Spiess *et al*., 2001; Ikeda *et al*., 2002; Ohfugi *et al*., 2005). Alternatively, the interatomic forces may not be strong enough to rotate crystals, but rather they arrest the movement of neighboring crystals when they reach an alignment position by chance (Cahn, 1954). Some authors consider this a sub-type of growth twinning (e.g., Smith, 1974b; Punin *et al*., 2009) even though it occurs once the crystals are of observable size (Vance, 1969). We consider growth twinning to involve errors in the attachment of a small group of atoms to a crystal face, and thus consider synneusis here as a separate potential mechanism of twin formation.

Synneusis has been observed *in situ* in laboratory experiments of plagioclase crystals suspended in heavy liquids (Viola, 1902), plus saturated solutions of lead nitrate, lithium sulphate, alum and cadmium iodide (Gaubert, 1896; Johnsen, 1907; Schaskolsy & Schubnikow, 1933; Kitazawa *et al*., 1971). Synneusis was observed when solutions were shaken, stirred, or otherwise agitated; when the same liquids were left to crystallize undisturbed, synneusis was less common or did not occur at all. Based on evidence from zoning patterns and/or blocky crystal outlines, synneusis has been recognized in glomeroporphyritic aggregates of plagioclase, quartz, and chromite in natural volcanic and plutonic rocks ranging in composition from dunite to granodiorite (Vogt, 1921; Ross,

1957; Vance & Gilreath, 1967; Vance, 1969). Visual inspection of olivine crystal aggregates from Kilauea Iki has also been interpreted as synneusis during crystal settling in liquid-rich basaltic magma (Schwindinger & Anderson, 1989). In many recent studies, the process of synneusis has been invoked to explain decreases in plagioclase and olivine crystal number densities in basaltic magmas even without visual evidence that this process occurred (Higgins & Chandrasekharam, 2007; Pupier *et al*., 2008; Vinet & Higgins, 2010). The first *in situ* observations of plagioclase synneusis in basaltic-andesite melt were reported by Schiavi *et al*. (2009) during experiments at 900°C and 1 bar pressure.

Even though synneusis may occur in natural volcanic rocks, this process is not likely responsible for the greater abundance of twinning in the lower pressure sample compared to the higher pressure sample. Unequivocal verification of synneusis requires *in situ* observations during crystallization; this process cannot be explicitly determined by examining final crystal textures (Dowty, 1980b). Although "*in situ*" experiments have been performed at high temperatures (e.g., Schiavi *et al*., 2009), there is no technology available at present that allows surveillance of high pressure crystal growth (Hammer, 2009). However, we do not believe that synneusis is responsible for the abundance of twinning observed at lower pressure in our rhyodacite magma for three reasons:
(1) Textural analyses of crystal along the 1 MPa h^{-1} decompression path and conversion of two dimensional shapes into three dimensions (e.g., Brugger & Hammer, 2010b) does not suggest an evolution of crystal shapes from elongate to more blocky as expected by synneusis (Duchêne *et al*., 2008; Pupier *et al*., 2008). The crystal aspect ratios appear

completely unrelated to quench pressure and thus the evolution along the decompression path.

(2) Synneusis requires the movement of crystals and it occurs during crystal settling or as a result of magma flowage (Ross, 1957; Schwindinger & Anderson, 1989; Schwindinger, 1999; Nespolo & Ferraris, 2004). There is no evidence of magma flow or crystal settling/floating in these samples (Brugger & Hammer, 2010a). The distribution of crystals and their textures are homogeneous throughout each sample, and crystal orientations appear random which suggests there is no alignment of grains. Thermal gradients driving convection are almost certainly absent in our experiments because phase abundances and compositions are constant throughout the charges.

(3) Synneusis twins can only form in a medium that is sufficiently fluid to allow extensive differential movement of crystals (Ross, 1957). Nearly all documented examples of synneusis are in basaltic magmas and occasionally in andesitic magmas (Vogt, 1921; Ross, 1957; Vance & Gilreath, 1967; Vance, 1969; Vance & Gildreath, 1967). In silicic samples with very low crystal fractions, such as the ones in this study (see Brugger & Hammer, 2010a), the total viscosity of the suspension is determined almost entirely by the viscosity of the interstitial liquid (Ryerson *et al*., 1988; Stevenson et al., 1996) which is calculated to be $2.6*10^4$ Pa s in the higher pressure sample and $1.0*10^7$ Pa s in the lower pressure sample (Giordano *et al*., 2008). Thus the viscosity of these samples is approximately 2-5 orders of magnitude higher than the basalts that have shown evidence of synneusis. High melt viscosity reduces the number of times that crystals accidentally come into contact. If crystals are moving about in a melt due to external forces (i.e. the host magma is flowing), then crystals may occasionally come into

random contact. However, even if there is a reduction in the free energy of the system afforded by a twin alignment of crystals, the energy barrier preventing spontaneous rotation of a crystal through highly viscous melt is implausibly high. Moreover, in the few cases where two crystals are arbitrarily touching, there appears to be no crystallographic relationship between them (see section “crystallographic relationships between contiguous plagioclase crystals” above).

IMPLICATIONS

Twinning is nearly 2.4 times more common in the lower pressure sample (15-4) than the higher pressure sample (1-3). Because sample 15-4 was annealed at the same pressure and temperature conditions as sample 1-3 prior to the commencement of decompression, the increase in twinning frequency occurred during the decompression of sample 15-4. As shown above, this twinning is not the result of deformation, transformation, or synneusis. This is growth twinning caused by atom attachment errors occurring during the incipient stages of crystallization as a result of a high degree of undercooling and supersaturation during the decompression of this sample. Recognition of growth twinning in these synthetic plagioclase crystals may have important implications for interpreting the growth history of natural crystals and the conditions under which they formed.

Twin boundaries in sample 15-4 are associated with crystal morphological defects. Swallowtails, irregular crystal terminations, embayments, and melt inclusions commonly occur along twin boundaries (Figure 4.5b-f). The association between swallowtails and twins has been previously recognized in olivine crystals by Faure *et al*. (2003). In addition, Punin *et al*. (2009) documented the presence of melt inclusions along

twin boundaries in plagioclase and noted differences in crystal length on either side of twin boundaries. Some studies attribute linear bands of melt inclusions to result from synneusis or agglomeration of crystals (Goldstein & Luth, 2006; Renner *et al*., 2002) or as the result of new hopper crystal growth on an older preexisting crystal (Kohut & Nielsen, 2004). However, the strong correlation between morphological defects and twin boundaries observed in this study suggests that these defects are the direct result of the higher energy boundary between twins. The twinning initially forms as a result of a high degree of undercooling at the incipient stages of crystal growth, but once the twins are established, they will persist even after the degree of undercooling lessens (Buerger, 1945). The energy barrier across the twin plane is greater than within a simple crystal (Cahn, 1954; Smith 1974b), thus atom attachment along the twin plane leads to less energy reduction than attachment on either side of the boundary within an individual twin. It follows that atoms may preferentially attach to areas of the growing crystal that do not lie along the twin boundary. This leads to the formation of hopper crystals, embayments, swallowtails, and uneven crystal terminations, and may eventually lead to the formation of melt inclusions when overgrowths of the outer crystal faces seal off and trap melt (Roedder, 1984; Kohut & Nielsen, 2004; Faure & Schiano, 2005).

Crystal growth rates are in part controlled by the removal of the latent heat of crystallization from the crystal melt boundary and the diffusion of crystal-forming atoms toward the boundary. At near-equilibrium conditions, these two processes are slower than the rate of atom attachment to the crystal face and the crystal growth mechanism is said to be “interface controlled.” The resulting crystals are typically planar-faceted, convex, and euhedral (Lofgren, 1974; Kirkpatrick, 1975). Under conditions of high effective

undercooling and high supersaturation, the rate of atom attachment is faster than the diffusion of chemical constituents to the crystal-melt boundary and the growth mechanism is “diffusion controlled” (Lofgren, 1974; Kirkpatrick, 1975). Plagioclase crystals that arise from diffusion controlled growth display characteristic anhedral crystal morphologies such as embayments, internal hopper cavities, or swallowtail protrusions (Lofgren, 1974; Corrigan, 1982; Hammer & Rutherford, 2002). When such anhedral morphologies are observed in volcanic rocks, the presumption is that they formed by diffusion controlled growth in an environment where a boundary layer of incompatible elements developed around the growing crystal, and protuberances on the corners and edges of the crystal penetrated through the boundary layer into melt that was richer in crystal-forming components (Lofgren, 1974; Philpotts, 1990; Hammer, 2005, 2008).

Our results suggest that the presence of boundary layers are not required for the formation of swallowtail and hopper textures and melt inclusions, and these textures do not necessarily denote diffusion controlled growth. Rather, these textures may form as a result of the high energy boundary between twins. We show that rapid nucleation and growth during the incipient stages of crystallization leads to growth twinning defects in the crystal structures of plagioclase. Diffusion controlled growth and twin defect formation both occur at conditions favoring rapid crystal growth at high undercooling. However, we suggest that the structural defects (twins) established very early in the crystal’s growth history may go on to play a greater role in controlling the resulting crystal morphology than the crystal growth mechanism.

ACKNOWLEDGEMENTS

Thanks go to Scott Sitzman for setting up our EBSD and teaching us how to use it, and for countless hours answering questions. Additional thanks to Kazuhide Nagashima and Gary Huss for assistance with the SEM. This work was also improved through insightful discussions with Benoît Welsch. This work was supported by National Science Foundation CAREER award (EAR04-49888 to J.E.H.).

APPENDIX. EBSD acquisition and indexing parameters

JEOL 5900LV Scanning Electron Microscope Operating Conditions

Acceleration voltage:	15 keV
Stage position:	Y=20-25, Z=28, Tilt=69.99
Working distance:	13-16 mm
Spot Size:	70

Flamenco Acquisition Parameters and Background Correction

Binning:	4x4
Gain:	High
Background number of frames:	64
Timing per frame:	120-180
Noise reduction number of frames:	9-14

Flamenco Band Detection and Indexing Conditions

Number of bands:	6-7 bands
Band Edges or Centers:	sometimes edges, sometimes centers
Hough resolution:	50-65
Maximum MAD value:	1.1

CHAPTER 5.

CONCLUSIONS

SUMMARY

All the studies presented in this dissertation utilize samples produced in water-saturated continuous decompression experiments with Aniakchak rhyodacite pumice starting material from the 3430 BP caldera-forming eruption. Prior to decompression, all experiments began with an initial anneal period at 130 MPa and 880°C, the pre-eruptive storage conditions for this rhyodacite magma as determined by Larsen (2006) using phase equilibria experiments.

Chapter 2 summaries the compositional and textural evolution of samples during decompression and compares results from four different decompression rates. This chapter also compares results of decompression experiments with equilibrium experiments. Plagioclase nucleation and growth rates are found to be strongly dependent on decompression rate. However, at each quench pressure, every sample has crystallized approximately equal volumes of plagioclase regardless of the decompression rate, even though this observed crystallinity is lower than the equilibrium crystallinity. Apparently, a constant degree of solidification is maintained by a crystallization mechanism striking a shifting balance between nuclei formation and growth of existing crystals. This chapter also explores the efficacy with which experimental results allow interpretation of the decompression histories of natural rocks. Feldspar microlites do not maintain chemical equilibrium with melt. They are more anorthite-rich than equilibrium plagioclase, which suggests that interpretations of magma ascent processes from natural samples require comparisons with dynamic rather than static (phase equilibrium) experiments. Although decompression rate is an important element controlling final textures in volcanic rocks, no single compositional or textural parameter uniquely records this rate. Of the criteria

examined, microlite number density and morphology are the best indicators of magma decompression rate. Chapter 2 also presents comparisons between multi-step decompression (MSD) experiments and continuous decompression (CD) experiments at the same time-integrated decompression rate of 1 MPa h^{-1}. These comparisons reveal that decompression path influences crystal textures, with stepwise decompression yielding textures correlative with faster decompression than indicated by the time-integrated decompression rate. Thus, considerations of magma ascent style, in addition to rate, will undoubtedly strengthen the interpretive power of experimental studies for constraining natural magma ascent processes.

Chapter 3 presents crystal size distributions (CSD) of plagioclase forming along two decompression paths, 2 MPa h^{-1} and 0.5 MPa h^{-1}. Samples display concave-up curved CSD plots resulting from two crystal populations: those formed during the anneal period and those formed during decompression. The CSDs also display a decrease in crystal number density at 3–7 μm, a size range that is easily resolvable with the SEM imaging employed in this study. This downturn at small sizes is presumably due to insufficient compensation for the intersection probability effect in converting two dimensional measurements to three dimensional size distributions. In this chapter, crystal nucleation and growth rates derived from CSDs using standard assumptions were compared with values obtained using two dimensional measurements of bulk crystal populations (batch methods). CSD-calculated nucleation rates are substantially low relative to the batch values. Indeed, CSD-derived volumetric nucleation rates may underestimate actual nucleation rates by up to two orders of magnitude. In contrast, growth rates from CSDs are consistently higher than batch rates. Although plagioclase

growth rates are relatively constant during decompression at a given rate, the average growth rate in the rapidly decompressed series is approximately five times faster than the crystal growth rate in the slowly decompressed series. Because crystal growth rate depends on decompression rate, CSDs are incapable of revealing decompression timescales or magma ascent rates without independent knowledge of crystal growth rate.

Chapter 4 presents results from electron backscatter diffraction studies of plagioclase crystallography and twinning in two experimental samples. One sample crystallized at constant temperature and pressure under near-equilibrium conditions and contains a population of euhedral faceted crystals and a low incidence of crystal twinning. The second sample crystallized during rapid (1 MPa hr^{-1}) decompression and conditions of increasing undercooling as the total amount of crystallization lagged further and further behind equilibrium crystallization along the decompression path. Crystals in this sample display abundant anhedral morphologies such as embayments, swallowtails, melt inclusions, and uneven crystal terminations, and twinning is abundant. This twinning is not the result of deformation, transformation, or synneusis, but rather growth defects introduced during the incipient stages of crystallization. The macroscopic morphological defects in these crystals (embayments, swallowtails, and melt inclusions) are dominated by the internal structure defects because of the high energy boundary along the twin planes. Thus, formation of twins during the incipient stages of crystallization has significant implications for the growth history of plagioclase crystals and the development of anhedral crystal morphologies. This chapter also affirms common crystal counting techniques used in textural studies of crystal number density. Contiguous crystals with parallel faces are crystallographically continuous crystals. In contrast,

contiguous crystals with non-parallel faces have unrelated internal structures and therefore represent separate crystals.

POTENTIAL FUTURE WORK

There are many potential future directions of inquiry into experimental studies of crystallization kinetics in silicic magmas. I consider one of the most important of these to be an exploration of the variation in textural differences between multi-step and continuous decompression samples as the size of the step and the total experimental duration varies. All previous decompression experiments are predicated on the assumption that stepwise decompression produces crystallization histories that are identical to continuous decompression. My preliminary comparison, documented in Chapter 2, illustrates the dramatic outcome of varying decompression style on nuclei density, crystal volume fraction, and crystal morphology. I suggest this finding calls into question the application of stepwise experiments to the interpretation of natural rocks, as the steps in MSD experiments are typically selected for the convenience of experimentalists. Alternatively, some scientists have suggested the opposite: that because magma ascent is intermittent in several documented instances (e.g., MSH; Cashman, 1992; Cashman & McConnell, 2005), my findings validate the use of MSD over CD experiments in the interpretation of natural rock textures. Sorting out whether MSD or CD experiments more closely approximate natural magma ascent is imperative.

I further recommend that future experimental studies examine the relationship between various pressure step sizes and the differences in textural results of MSD and CD experiments at the same integrated decompression rate. As the size of pressure steps

decrease, MSD samples are expected to become increasingly similar to CD samples performed at the same integrated decompression rate. That is, at the limit of infinitesimally small pressure drops, there would be no difference between MSD and CD experiments. For researchers without access to a programmable pressure controller, it would be useful to know at what maximum step size are MSD results indistinguishable from CD. Similarly, as total experimental duration increases, I expect the magnitude of the pressure steps to be less important compared with the duration of dwell time at each step. Thus, future studies should also determine the differences between MSD and CD experiments as a function of total experimental duration and establish which integrated decompression rates produce the most similar and dissimilar textural results.

A second potential focus of future experimental inquiry is to design experiments that more closely resemble natural magma ascent processes. While continuously decreasing pressure may be more similar to natural magma ascent than stepwise decompression, magma ascent is not a constant-*rate* process (Rutherford, 2008). Explosive eruptions result from magma ascent rate that increases as magma ascends, while effusive eruptions occur when magma ascent rate progressively decreases and volatiles are able to decouple from the melt. Thus experimental studies involving variable rate decompression may provide further insights into crystallization processes during natural magma ascent as they more closely mimic natural magma ascent.

REFERENCES

Angel, R.J., Carpenter, M.A., & Finger, L.W. (1990). Structural variation associated with compositional variation and order-disorder behavior in anorthite-rich feldspars. *American Mineralogist* **75**, 150-162.

Armienti, P. (2008). Decryption of igneous rock textures: crystal size distribution tools. In: Minerals, Inclusions and Volcanic Processes. *Reviews in Mineralogy and Geochemistry* **69**, 623-648.

Armienti, P., Pareschi, M.T., Innocenti, F. & Pompilio, M. (1994). Effects of magma storage and ascent on the kinetics of crystal growth: the case of the 1991-1993 Mt. Etna eruption. *Contributions to Mineralogy and Petrology* **115**, 402-414.

Asimow, P.D. & Ghiorso, M.S. (1998). Algorithmic Modifications Extending MELTS to Calculate Subsolidus Phase Relations. *American Mineralogist* **83**, 1127-1131.

Bindeman, I.N. (2003). Crystal sizes in evolving silicic magma chambers. *Geology* **31**, 367-370.

Blundy, J. & Cashman, K.V. (2001). Ascent-driven crystallization of dacite magmas at Mount St Helens, 1980-1986. *Contributions to Mineralogy and Petrology* **140**, 631-650.

Blundy, J. & Cashman, K.V. (2008). *Petrologic reconstruction of magmatic system variables and processes*. In: Putirka, K.D. & Tepley III, F.J. (eds.) *Minerals, Inclusions and Volcanic Processes*, **69**. Chantilly, Virginia: The Mineralogical Society of America, 179-239.

Borg, I.Y. & Handin, J. (1966). Experimental deformation of crystalline rocks. *Tectonophysics* **3**, 249-368.

Borg, I.Y. & Heard, H.C. (1969). Mechanical twinning and slip in experimentally deformed plagioclases. *Contributions to Mineralology and Petrology* **23**, 128-135.

Boyle, A.P., Prior, D.J., Banham, M.H. & Timms, N.E. (1998). Plastic deformation of metamorphic pyrite: new evidence from electron backscatter diffraction and forescatter orientation contrast imaging. *Mineralium Deposita* **34**, 71–81.

Browne, B.L. & Gardner, J.E. (2006). The influence of magma ascent path on the texture, mineralogy, and formation of hornblende reaction rims. *Earth and Planetary Science Letters* **246**, 161-176.

Brugger, C.R. & Hammer, J.E. (2010a) Crystallization Kinetics in Continuous Decompression Experiments: Implications for Interpreting Natural Magma Ascent Processes. *Journal of Petrology* **51**, 1941-1956.

Brugger, C.R. & Hammer, J.E. (2010b). Crystal size distribution analysis of plagioclase in experimentally decompressed hydrous rhyodacite magma. *Earth and Planetary Science Letters* **300**, 246-254.

Brugger, C.R., Johnston, A.D. & Cashman, K.V. (2003). Phase relations in silicic systems at one-atmosphere pressure. *Contributions to Mineralogy and Petrology* **146**, 356-369.

Buerger, M.J. (1945). The genesis of twin crystals. *American Mineralogist* **30**, 469-482.

Burnham, C.W. & Davis, N.F. (1971). The role of H_2O in silicate melts: 1. P-V-T relations in the system $NaAlSi_3O_8$-H_2O to 10 kilobars and 1000˚C. *American Journal of Science* **270**, 54-79.

Cabane, H., Laporte, D. & Provost, A. (2005). An experimental study of Ostwald ripening of olivine and plagioclase in silicate melts: implications for the growth and size of crystals in magmas. *Contributions to Mineralogy and Petrology* **150**, 37-53.

Cahn, R.W. (1954). Twinned crystals. *Advances in Physics* **3**, 202-445.

Cashman, K.V. (1988). Crystallization of Mount St. Helens 1980-1986 dacite: a quantitative textural approach. *Bulletin of Volcanology* **50**, 194-209.

Cashman, K.V. (1990). Textural constraints on the kinetics of crystallization of igneous rocks. In: Nicholls, J. & Russell, J. K. (eds) *Modern Methods of Igneous Petrology: Understanding Magmatic Processes. Mineralogical Society of America, Reviews in Mineralogy* **24**, 259-314.

Cashman, K.V. (1992). Groundmass crystallization of Mount St. Helens dacite 1980-1986: a tool for interpreting shallow magmatic processes. *Contributions to Mineralogy and Petrology* **109**, 431-449.

Cashman, K.V. (1993). Relationship between plagioclase crystallization and cooling rate in basaltic melts. *Contributions to Mineralogy and Petrology* **113**, 126-142.

Cashman, K.V. & Blundy, J. (2000). Degassing and crystallization of ascending andesite and dacite. *Philosophical Transactions of the Royal Society of London Series a-Mathematical Physical and Engineering Sciences* **358**, 1487-1513.

Cashman, K.V. & Ferry, J.M. (1988). Crystal size distribution (CSD) in rocks and the kinetics and dynamics of crystallization. *Contributions to Mineralogy and Petrology* **99**, 401-415.

Cashman, K.V. & Marsh, B.D. (1988). Crystal size distribution (CSD) in rocks and the kinetics and dynamics of crystallization – II: Makaopuhi lava lake. *Contributions to Mineralogy and Petrology* **99**, 292-305.

Cashman, K.V. & McConnell, S.M. (2005). Multiple levels of magma storage during the 1980 summer eruptions of Mount St. Helens, WA. *Bulletin of Volcanology* **68**, 57–75.

Cashman, K.V., Thornber, C. & Kauahikaua, J.P. (1999). Cooling and crystallization of lava in open channels, and the transition of Pahoehoe lava to ‘a’a. *Bulletin of Volcanology* **61**, 306-323.

Castro, J.M. & Gardner, J.E. (2008). Did magma ascent rate control the explosive-effusive transition at the Inyo volcanic chain, California? *Geology* **36**, 279-282.

Castro, J., Manga, M. & Cashman, K. (2002). Dynamics of obsidian flows inferred from microstructures: insights from microlite preferred orientations. *Earth and Planetary Science Letters* **199**, 211-226.

Cheng, H. & Lemlich, R. (1983). Errors in measurement of bubble size distribution in foam. *Industrial and Engineering Chemistry Fundamentals* **22**, 105-109.

Cigolini, C., Laiolo, M. & Bertolino, S. (2008). Probing Stromboli Volcano from the mantle to paroxysmal eruptions. In: Annen, C., Zellmer, G.F. (Eds.), Dynamics of Crustal Magma Transfer. *Geological Society of London Special Publication* **304**, Bath, UK, pp. 33-70.

Clarke, A.B., Stephens, S., Teasdale, R., Sparks, R.S.J. & Diller, K. (2007). Petrologic constraints on the decompression history of magma prior to Vulcanian explosions at the Soufriére Hills volcano, Montserrat. *Journal of Volcanology and Geothermal Research* **161**, 261-274.

Congdon, R.D., Resmini, R.G. & Marsh, B.D. (1993). Differentiation style in the Box Elder and Shonkin Sag Laccoliths; dependence on initial conditions. *EOS Transactions American Geophysical Union* **73**, 336.

Conte, A.M., Perinelli, C. & Trigila, R. (2006). Cooling kinetics experiments on different Stromboli lavas: Effects on crystal morphologies and phases composition. *Journal of Volcanology and Geothermal Research* **155**, 179-200.

Coombs, M.L., Eichelberger, J.C. & Rutherford, M.J. (2003). Experimental and textural constraints on mafic enclave formation in volcanic rocks. *Journal of Volcanology and Geothermal Research* **119**, 125-144.

Corrigan, G.M. (1982). The crystal morphology of plagioclase feldspar produced during isothermal supercooling and constant rate cooling experiments. *Mineralogical Magazine* **46**, 433-439.

Costa, F. & Chakraborty, S. (2004). Decadal time gaps between mafic intrusion and silicic eruption obtained from chemical zoning patterns in olivine. *Earth and Planetary Science Letters* **227**, 517-530.

Couch, S., Harford, C.L., Sparks, R.S.J. & Carroll, M.R. (2003a). Experimental constraints on the conditions of formation of highly calcic plagioclase microlites at Soufriere Hills Volcano, Montserrat. *Journal of Petrology* **44**, 1455-1475.

Couch, S., Sparks, R.S.J. & Carroll, M.R. (2003b). The kinetics of degassing-induced crystallization at Soufriere Hills Volcano, Montserrat. *Journal of Petrology* **44**, 1477-1502.

Crisp, J., Cashman, K.V., Bonini, J.A., Hougen, S.B. & Pieri, D.C. (1994). Crystallization history of the 1984 Mauna Loa Lava flow. *Journal of Geophysical Research* **99**, 7177-7198.

Deer, W.A., Howie, R.A. & Zussman, J. (1992). *An Introduction to the Rock-Forming Minerals, 2nd edition*. Hong Kong: Addison Wesley Longman Limited, pp. 407.

DeHoff, R.T. & Rhines, F.N. (1968) *Quantitative Microscopy*. New York: McGraw-Hill Book Co.

Delesse, M.A. (1847). Procedé mécanique pour déterminer la composition des roches. *Comptes rendus de l'académie des sciences* **25**, Paris, pp. 544-545.

Devine, J.D., Gardner, J.E., Brack, H.P., Layne, G.D. & Rutherford, M.J. (1995). Comparison of microanalytical methods for estimating H2O contents of silicic volcanic glasses. *American Mineralogist* **80**, 319–328.

Dowty, E. (1980a). Computing and drawing crystal shapes. *American Mineralogist* **65**, 465-471.

Dowty, E. (1980b). Synneusis reconsidered. *Contributions to Mineralogy and Petrology* **74**, 75-84.

Dowty, E. (2008). SHAPE. Version 7.2.3. Shape Software, Kingsport, Tennessee, USA. http://www.shapesoftware.com.

Dreher, S.T. (2002). The physical volcanology and petrology of the 3400 YBP caldera-forming eruption of Aniakchak Volcano, Alaska. Ph.D. thesis, University of Alaska Fairbanks, Fairbanks, AK, 174 pp.

Dreher, S.T., Eichelberger, J.C. & Larsen, J.F. (2005). The petrology and geochemistry of the Aniakchak caldera-forming ignimbrite, Aleutian Arc, Alaska. *Journal of Petrology* **46**, 1747-1768.

Duchêne, S., Pupier, E., Le Carlier de Veslud, C. & Toplis, M.J. (2008). A 3D reconstruction of plagioclase crystals in a synthetic basalt. *American Mineralogist* **93**, 893-901.

Eason, D. & Sinton, J. (2006) Origin of high-Al N-MORB by fractional crystallization in the upper mantle beneath the Galapagos spreading center. *Earth and Planetary Science Letters* **252**, 423-436.

Ebadi, A. & Johannes, W. (1991). Beginning of melting and composition of first melts in the system Qz-Ab-Or-H_2O-CO_2. *Contributions to Mineralogy and Petrology* **106**, 286-295.

Eberl, D.D., Kile, D.E. & Drits, V.A. (2002). On geological interpretations of crystal size distributions: Constant vs. proportionate growth. *American Mineralogist* **87**, 1235-1241.

Eichelberger, J.C. (1995) Silicic volcanism: ascent of viscous magmas from crustal reservoirs. *Annual Review of Earth and Planetary Sciences* **23**, 41-63.

Emmons, R.C. & Gates, R.M. (1943). Plagioclase Twinning. *Bulletin of the Geological Society of America* **54**, 287-304.

Endo, E.T., Dzurisin, D. & Swanson, D.A. (1990). Geophysical and observational constraints for shallow ascent rates of dacitic magma at Mount St. Helens. In: Ryan, M.P. (ed.) *Magma Transport and Storage*. New York: Wiley, pp. 317-334.

Faure, F. & Schiano, P. (2005). Experimental investigation of equilibration conditions during forsterite growth and melt inclusion formation. *Earth and Planetary Science Letters* **236**, 882-898.

Faure, F., Trolliard, G., Nicollet, C. & Montel, J-M. (2003). A developmental model of olivine morphology as a function of the cooling rate and the degree of undercooling. *Contributions to Mineralogy and Petrology* **145**, 251-263.

Field, M., Gernon, T.M., Mock, A., Walters, A., Sparks, R.S.J. & Jerram, D.A. (2009). Variations of olivine abundance and grain size in the Snap Lake kimberlite intrusion, Northwest Territories, Canada: A possible proxy for diamonds. *Lithos* **112**, 23-35.

Fliervoet, T.F., Drury, M.R. & Chopra, P.N. (1999). Crystallographic preferred orientations and misorientations in some olivine rocks deformed by diffusion or dislocation creep. *Tectonophysics* **303**, 1–27.

Fokin, V.M., Kalinina, A.M. & Filipovich, V.N. (1981). Nucleation in silicate glasses and effect of preliminary heat treatment on it. *Journal of Crystal Growth* **52**, 115-121.

Force, B.D. (2011). Schlieren structures in the Mount Waldo granitic pluton, Maine; implications for magma chamber processes. *Geological Society of America Abstracts with Programs* **43**, 78.

Fowler, S.J, Spera, F.J, Bohron, W.A., Belkin, H.E. & De Vivo, B. (2007). Phase equilibria constraints on the chemical and physical evolution of the Campanian ignimbrite. *Journal of Petrology* **48**, 459-493.

Freitag, K., Boyle, A.P., Nelson, E., Hitzman, M., Churchill, J. & Lopez-Pedrosa, M. (2004). The use of electron backscatter diffraction and orientation contrast imaging as tools for sulphide textural studies: example from the Greens Creek deposit (Alaska). *Mineralium D**eposita*** **39**, 103–113.

Gardner, C.A., Cashman, K.V. & Neal, C.A. (1998). Tephra fall deposits from the 1992 eruption of Crater Peak, Alaska: implications of clast textures for eruptive products. *Bulletin of Volcanology* **59**, 537–555.

Gardner, J.E., Hilton, M. & Carroll, M.R. (1999). Experimental constraints on degassing of magma; isothermal bubble growth during continuous decompression from high pressure. *Earth and Planetary Science Letters* **168**, 201-218.

Gardner, J.E., Rutherford, M., Carey, S. & Sigurdsson, H. (1995). Experimental constraints on pre-eruptive water contents and changing magma storage prior to explosive eruptions of Mount St Helens volcano. *Bulletin of Volcanology* **57**, 1-17.

Garrido, C.J., Keleman, P.B. & Hirth, G. (2001). Variation of cooling rate with depth in lower crust formed at an oceanic spreading ridge: Plagioclase crystal size distributions in gabbros from the Oman ophiolite. *Geochemistry Geophysics Geosystems* **2(10)**, 2000GC000136.

Gaubert, P. (1896). Sur la production artificielle de la macle des spinelles dans les cristaux d'azotate de plomb. *Bulletin de la Societe Francaise de Mineralogie* **19**, 431-434.

Genareau, K., Clarke, A.B. & Hervig, R.L. (2009). New insight into explosive volcanic eruptions: connecting crystal-scale chemical change with conduit-scale dynamics. *Geology* **37**, 367-370.

Genareu, K., Valentine, G.A., Moore, G. & Hervig, R.L. (2010). Mechanisms for transition in eruptive style at a monogenetic scoria cone revealed by microtextural analyses (Lathrop Wells volcano, Nevada, U.S.A.). *Bulletin of Volcanology* **72**, 593-607.

Geschwind, C-H. & Rutherford, M.J. (1992). Cummingtonite and the evolution of the Mount St. Helens magma system: an experimental study. *Geology* **20**, 1011-1014.

Geschwind, C-H. & Rutherford, M.J. (1995). Crystallization of microlites during magma ascent: the fluid mechanics of 1980-1986 eruptions at Mount St Helens. *Bulletin of Volcanology* **57**, 356-370.

Ghiorso, M.S. & Sack, R.O. (1995). Chemical Mass Transfer in Magmatic Processes. IV. A Revised and Internally Consistent Thermodynamic Model for the Interpolation and Extrapolation of Liquid-Solid Equilibria in Magmatic Systems at Elevated Temperatures and Pressures. *Contributions to Mineralogy and Petrology* **119**, 197-212.

Giordano, D., Russell, J.K. & Dingwell, D.B. (2008). Viscosity of magmatic liquids: A model. *Earth and Planetary Science Letters* **271**, 123-134.

Goldstein, S.B. & Luth, R.W. (2006). The importance of cooling regime in the formation of melt inclusions in olivine crystals in haplobasaltic melts. *The Canadian Mineralogist* **44**, 1543-1555.

Gonde, C., Massare, D., Bureau, H., Martel, C., Pichavant, M.& Clocchiatti, R. (2006). In situ study of magmatic processes: a new experimental approach. *High Pressure Research* **26**, 243-250.

Grove, T.L. & Bence, A.E. (1979). Crystallization in a multiply saturated basalt magma; an experimental study of Luna 24 ferrobasalt. *Lunar and Planetary Science Conference* **X**, 439-478.

Hammer, J.E. (2004). Crystal nucleation in hydrous rhyolite: Experimental data applied to classical theory. *American Mineralogist* **89**, 1673-1679.

Hammer, J.E. (2005). Strange attractors: symbiosis in magma crystallization. *EOS, Transactions American Geophysical Union* **86**, V12A-07.

Hammer, J.E. (2008). Experimental studies of the kinetics and energetics of magma crystallization. In: Putirka, K.D. & Tepley III, F.J. (eds.) *Minerals, Inclusions and Volcanic Processes. The Mineralogical Society of America and Geochemical Society, Reviews in Mineralogy and Geochemistry* **69**, 9-59.

Hammer, J.E., Cashman, K.V., Hoblitt, R.P. & Newman, S. (1999). Degassing and microlite crystallization during pre-climactic events of the 1991 eruption of Mt. Pinatubo, Philippines. *Bulletin of Volcanology* **60**, 355-380.

Hammer, J.E., Cashman, K.V. & Voight, B. (2000). Magmatic processes revealed by textural and compositional trends in Merapi dome lavas. *Journal of Volcanology and Geothermal Research* **100**, 165-192.

Hammer, J.E. & Rutherford, M.J. (2002). An experimental study of the kinetics of decompression-induced crystallization in silicic melts. *Journal of Geophysical Research* **197**, 1-23.

Hammer, J.E., Rutherford, M.J. & Hildreth, W. (2002). Magma storage prior to the 1912 eruption at Novarupta, Alaska. *Contributions to Mineralogy and Petrology* **144**, 144-162.

Hammer, J.E., Sharp, T.G. & Wessel, P. (2010). Heterogeneous nucleation and epitaxial crystal growth of magmatic minerals. *Geology* **38**, 367-370.

Higgins, M.D. (1996a). Crystal size distributions and other quantitative textural measurements in lavas and tuff from Egmont volcano (Mt. Taranaki), New Zealand. *Bulletin of Volcanology* **58**, 194-204.

Higgins, M.D. (1996b). Magma dynamics beneath Kameni volcano, Thera, Greece, as revealed by crystal size and shape measurements. *Journal of Volcanology and Geothermal Research* **70**, 37-48.

Higgins, M.D. (1998). Origin of Anorthosite by textural coarsening: quantitative measurements of a natural sequence of textural development. *Journal of Petrology* **39**, 1307-1323.

Higgins, M.D. (1999). Origin of megacrysts in granitoids by textural coarsening: A crystal size distribution (CSD) study of microcline in the Cathedral Peak Granodiorite, Sierra Nevada, California. In: Castro, A., Fernandez, C., Vigneresse, J.L. (eds.) *Understanding Granites: Integrating New and Classical Techniques. Geological Society of London Special Publication* **168**, London, pp. 207-219.

Higgins, M.D. (2000). Measurement of crystal size distributions. *American Mineralogist* **85(9)**, 1105–1116.

Higgins, M.D. (2002). A crystal size-distribution study of the Kiglapait layered mafic intrusion, Labrador, Canada: evidence for textural coarsening. *Contributions to Mineralogy and Petrology* **144**, 314-330.

Higgins, M.D. (2006). Quantitative textural measurements in igneous and metamorphic petrology. Cambridge, UK: Cambridge University Press.

Higgins, M.D. & Chandrasekharam, D. (2007). Nature of sub-volcanic magma chambers, Deccan Province, India: evidence from quantitative textural analysis of plagioclase megacrysts in the Giant Plagioclase Basalts. *Journal of Petrology* **48**, 885-900.

Higgins, M.D. & Roberge, J. (2003). Crystal size distribution of plagioclase and amphibole from Soufrière Hills Volcano, Montserrat: evidence for dynamic crystallization-textural coarsening cycles. *Journal of Petrology* **44**, 1401-1411.

Higgins, M.D. & Roberge, J. (2007). Three magmatic components in the 1973 eruption of Eldfell volcano, Iceland: Evidence from plagioclase crystal size distribution (CSD) and geochemistry. *Journal of Volcanology and Geothermal Research* **161**, 247-260.

Hoblitt, R.P. & Harmon, R.S. (1993). Bimodal density distribution of cryptodome dacite from the 1980 eruption of Mount St. Helens, Washington. *Bulletin of Volcanology* **55**, 421-437.

Ikeda, S., Toriumi, M., Yoshida, H. & Shimizu, I. (2002). Experimental study of the textural development of igneous rocks in the late stage of crystallization: the importance of interfacial energies under non-equilibrium conditions. *Contributions to Mineralogy and Petrology* **142**, 397-415.

James, P.F. (1974). Kinetics of crystal nucleation in lithium silicate glasses. *Physics and Chemistry of Glasses* **15**, 95-105.

James, P.F. (1985). Kinetics of crystal nucleation in silicate glasses. *Journal of Non-Crystalline Solids* **73**, 517-540.

Jancic S. & Garside, J. (1976). A new technique for accurate crystal size distribution analysis in an MSMPR crystallizer. In: Mullin, J.F. (ed.) *Industrial Crystallization*. New York: Plenum Press, 472 p.

Janse, E.H. & deJong, E.J. (1976). The occurrence of growth dispersion and its consequences. In: Mullin, J.F. (ed.) *Industrial Crystallization*. New York: Plenum Press, 472 p.

Jerram, D.A., Cheadle, M.J. & Philpotts, A.R. (2003). Quantifying the Building Blocks of Igneous Rocks: Are Clustered Crystal Frameworks the Foundation? *Journal of Petrology* **44**, 2033-2051.

Jerram, D.A., Mock, A., Davis, G.R., Field, M. & Brown, R.J. (2009). 3D crystal size distributions: A case study on quantifying olivine populations in kimberlites. *Lithos* **112**, 223-235.

Johnsen, A. (1907). Tschermak's Zwillingstheorie und das Gesetz der Glimmerzwillinge. *Centralbl. Mineral. Geolog. Palaeontol.*

Kelton, K.F. (2004). Nucleation in glasses and liquids and nanostructure formation. *Physics and Chemistry of Glasses – European Journal of Glass Science and Technology Part B* **45**, 64-70.

Kile, D.E. & Eberl, D.D. (2003). On the origin of size-dependent and size-independent crystal growth; influence of advection and diffusion. *American Mineralogist* **88**, 1514-1521.

Kile, D.E., Eberl, D.D., Hoch, A.R. & Reddy, M.M. (2000). An assessment of calcite crystal growth mechanisms based on crystal size distributions. *Geochimica et Cosmochimica Acta* **64**, 2937-2950.

Kirkpatrick, R.J. (1975). Crystal growth from a melt: a review. *American Mineralogist* **60**, 798-614.

Kirkpatrick, R.J. (1981). Kinetics of crystallization of igneous rocks. *Reviews in Mineralogy* **8**, 321-398.

Kitazawa, S., Sunagawa, I. & Endo, Y. (1971). Growth and dissolution of cadmium iodide crystals. *Mineralogical Society of Japan Special Paper* **1**, 109-113 (Proceedings IMA-IAGOD Meetings '70, IMA Volume).

Kohut, E. & Nielsen, R.L. (2004). Melt inclusion formation mechanisms and compositional effects in high-An feldspar and high-Fo olivine in anhydrous mafic silicate liquids. *Contributions to Mineralogy and Petrology* **147**, 684-704.

Larsen, J.F. (2005). Experimental study of plagioclase rim growth around anorthite seed crystals in rhyodacitic melt. *American Mineralogist* **90**, 417-427.

Larsen, J.F. (2006). Rhyodacite magma storage conditions prior to the 3430 yBP caldera-forming eruption of Aniakchak volcano, Alaska. *Contributions to Mineralogy and Petrology* **152**, 523-540.

Lees, J.M. & Crosson, R.S. (1989). Tomographic inversion for three-dimensional velocity structure at Mount St. Helens using earthquake data. *Journal of Geophysical Research* **94**, 5716-5728.

Lentz, R.C.F. & McSween, H.Y.J. (2000). Crystallization of the basaltic shergottites: insights from crystal size distribution (CSD) analysis of pyroxenes. *Meteoritics and Planetary Science* **35(5)**, 919-927.

Lesher, C.E., Cashman, K.V. & Mayfield, J.D. (1999). Kinetic controls on crystallization of Tertiary North Atlantic basalt and implications for the emplacement and cooling history of lava at Site 989, Southeast Greenland rifted margin. *Proceedings of the Ocean Drilling Program* **163**, 135-148.

Lipman, P.W. & Banks, N.G. (1987). Aa flow dynamics, Mauna Loa 1984. *US Geological Survey Professional Paper* **1350**, 1527-1567.

Lofgren, G.E. (1973). Experimental crystallization of synthetic plagioclase at prescribed cooling rates. *EOS Transactions American Geophysical Union* **54**, 482.

Lofgren, G.E. (1974). An experimental study of plagioclase crystal morphology: isothermal crystallization. *American Journal of Science* **274**, 243-273.

Lofgren, G.E. (1980). Experimental studies on the dynamic crystallization of silicate melts. In: Hargraves, R.B. (ed.) *The Physics of Magmatic Processes*. Princeton, NJ: Princeton University Press, pp. 487-551.

Luth, W.C., Jahns, R.H. & Tuttle, O.F. (1964). The granite system at pressures of 4 to 10 kilobars. *Journal of Geophysical Research* **69**, 759-773.

Ma, C. & Rossman, G.R. (2009). Tistarite, Ti_2O_3, a new refractory mineral from the Allende meteorite. *American Mineralogist* **94**, 841-844.

Magee, C., O'Driscoll, B. & Chambers, A.D. (2010). Crystallization and textural evolution of a closed-system magma chamber: insights from a crystal size distribution study of the Lilloise layered intrusion, East Greenland. *Geological Magazine* **147**, 363-379.

Mangan, M.T. (1990). Crystal size distribution systematics and the determination of magma storage times: the 1959 eruption of Kilauea Volcano, Hawaii. *Journal of Volcanology and Geothermal Research* **44**, 295-302.

Mangan, M. & Sisson, T. (2000). Delayed, disequilibrium degassing in rhyolite magma: decompression experiments and implications for explosive volcanism. *Earth and Planetary Science Letters* **183**, 441-445.

Marsh, B.D. (1988). Crystal size distribution (CSD) in rocks and the kinetics and dynamics of crystallization; I. Theory. *Contributions to Mineralogy and Petrology* **99**, 277–291.

Marsh, B.D. (1998). On the interpretation of crystal size distributions in magmatic systems. *Journal of Petrology* **39**, 553-599.

Marsh, B.D., Gunnarsson, B., Congdon, R. & Carmody, R. (1991). Hawaiian basalt and Icelandic rhyolite: indicators of differentiation and partial melting. *Geologische Rundschau* **80/2**, 481-510.

Martel, C., Ali, A.R., Poussineau, S., Gourgaud, A. & Pichavant, M. (2006). Basalt-inherited microlites in silicic magmas: Evidence from Mount Pelee (Martinique, French West Indies). *Geology* **34**, 905-908.

Martel, C., Pichavant, M., Holtz, F., Scaillet, B., Bourdier, J-L. & Traineau, H. (1999). Effects of fO2 and H2O on andesite phase relations between 2 and 4 kbars. *Journal of Geophysical Research* **104**, 29,453-29,470.

Martel, C. & Poussineau, S. (2007). Diversity of eruptive styles inferred from the microlites of Mt Pelée andesite (Martinique, Lesser Antilles). *Journal of Volcanology and Geothermal Research* **166**, 233-254.

Martel, C. & Schmidt, B.C. (2003). Decompression experiments as an insight into ascent rates of silicic magmas. *Contributions to Mineralogy and Petrology* **144**, 397-415.

Mastrolorenzo, G. & Pappalardo, L. (2006). Magma degassing and crystallization processes during eruptions of high-risk Neapolitan-volcanoes: Evidence of common equilibrium rising processes in alkaline magmas. *Earth and Planetary Science Letters* **250**, 164-181.

Mattsson, H.B. (2010). Textural variation in juvenile pyroclasts from an emergent, Surtseyan-type, volcanic eruption: the Capelas tuff cone, São Miguel (Azores). *Journal of Volcanology and Geothermal Research* **189**, 81-91.

McCanta, M.C., Rutherford, M.J. & Hammer, J.E. (2007). Pre-eruptive and syn-eruptive conditions in the Black Butte, California dacite: Insight into crystallization kinetics in a silicic magma system. *Journal of Volcanology and Geothermal Research* **160**, 263-284.

McCarter, R.L., Fodor, R.V. & Trusdell, F. (2006). Perspectives on basaltic magma crystallization and differentiation: Lava-lake blocks erupted at Mauna Loa volcano summit, Hawaii. *Lithos* **90**, 187-213.

Means, W.D. & Park, Y. (1994). New experimental approach to understanding igneous texture. *Geology* **23**, 323-326.

Mikouchi, T., Zolensky, M., Ivanova, M., Tachikawa, O., Komatsu, M., Le, L. & Gounelle, M. (2009). Dmitryivanovite: A new high-pressure calcium aluminum oxide from the Northwest Africa 470 CH3 chondrite characterized using electron backscatter diffraction analysis. *American Mineralogist* **94**, 746-750.

Miller, T.P. & Smith, R.L. (1987). Late Quaternary caldera-forming eruptions in the eastern Aleutian arc, Alaska. *Geology* **15**, 434–438.

Moore, G. & Carmichael, I.S.E. (1998). The hydrous phase equilibria (to 3 kbar) of an andesite and basaltic andesite from western Mexico: constraints on water content and conditions of phenocryst growth. *Contributions to Mineralogy and Petrology* **130**, 304-319.

Moore, G., Vennemann, T. & Carmichael, I.S.E. (1998). An empirical model for the solubility of H_2O in magmas to 3 kilobars. *American Mineralogist* **83**, 36-42.

Morgan, D.J. & Jerram, D.A. (2006). On estimating crystal shape for crystal size distribution analysis. *Journal of Volcanology and Geothermal Research* **154**, 1-7.

Morgan, G.B. & London, D. (1996). Optimizing the electron microprobe analysis of hydrous alkali aluminosilicate glasses. *American Mineralogist* **81**, 1176–1185.

Moss, S., Russell, J.K., Scott Smith, B.H. & Brett, R.C. (2010). Olivine crystal size distributions in kimberlite. *American Mineralogist* **95**, 527-536.

Muncill, G.E. & Lasaga, A.C. (1987). Crystal-growth kinetics of plagioclase in igneous systems: One atmosphere experiments and application of a simplified growth model. *American Mineralogist* **72**, 299-311.

Nespolo, M. & Ferraris G. (2004). The oriented attachment mechanism in the formation of twins – a survey. *European Journal of Mineralogy* **16**, 401-406.

Nesse, W.D. (2000). *Introduction to Mineralogy*. New York: Oxford University Press, 442 pp.

Newman, S., Epstein, S. & Stolper, E. (1988). Water, carbon dioxide, and hydrogen isotopes in glasses from the ca. 1340 A.D. eruption of the Mono Craters, California: constraints on degassing phenomena and initial volatile content. *Journal of Volcanology and Geothermal Research* **35**, 75-96.

Nielsen, C. & Sigurdsson, H. (1981). Quantitative methods of electron microprobe analysis of sodium in natural and synthetic glasses. *American Mineralogist* **66**, 547-552.

Nicholis, M.G. & Rutherford, M.J. (2004). Experimental constraints on magma ascent rate for the Crater Flat volcanic zone hawaiite. *Geology* **32**, 489-492.

Noguchi, S., Toramaru, A. & Nakada, S. (2008). Relation between microlite textures and discharge rate during the 1991–1995 eruptions at Unzen, Japan. *Journal of Volcanology and Geothermal Research* **175**, 141-155.

Noguchi, S., Toramaru, A. & Shimano, T. (2006). Crystallization of microlites and degassing during magma ascent: Constraints on the fluid mechanical behavior of magma during the Tenjo eruption on Kozu Island, Japan. *Bulletin of Volcanology* **68**, 432-449.

Ohfuji, H., Boyle, A.P., Prior, D.J. & Rickard, D. (2005). Structure of framboidal pyrite: an electron backscatter diffraction study. *American Mineralogist* **90**, 1693-1704.

Papale, P., Moretti, R. & Barbato, D. (2006). The compositional dependence of the saturation surface of H2O+CO2 fluids in silicate melts. *Chemical Geology* **229**, 78-95.

Pappalardo, L., Ottolini, L. & Mastrolorenzo, G. (2007). The Campanian Ignimbrite (southern Italy) geochemical zoning: insight on the generation of a super-eruption from catastrophic differentiation and fast withdrawal. *Contributions to Mineralogy and Petrology* **156**, 1-16.

Peterson, T.D. (1996). A refined technique for measuring crystal size distributions in thin section. *Contributions to Mineralogy and Petrology* **124**, 395-405.

Philpotts, A.R. (1990). *Principles of Igneous and Metamorphic Petrology*. New Jersey: Prentice Hall, 498 pp.

Pichavant, M., Costa, F., Burgisser, A., Scaillet, B., Martel, C. & Poussineau, S. (2007). Equilibration scales in silicic to intermediate magmas – Implications for experimental studies. *Journal of Petrology* **48**, 1955-1972.

Pichavant, M., Martel, C., Bourdier, J-L. & Scaillet, B. (2002). Physical conditions, structure, and dynamics of a zoned magma chamber: Mount Pelee (Martinique, Lesser Antilles Arc). *Journal of Geophysical Research* **107(B5)**, 2093, doi:10.1029/2001JB000315.

Piochi, M., Mastrolorenzo, G. & Pappalardo, L. (2005). Magma ascent and eruptive processes from textural and compositional features of Monte Nuovo pyroclastic products, Campi Flegrei, Italy. *Bulletin of Volcanology* **67**, 663-678.

Porter, D.A. & Easterling, K.E. (1992). *Phase transformations in metals and alloys, 2nd edition*. London: Chapman and Hall, 514 pp.

Prior, D.J. (1999). Problems in determining the orientations of crystal misorientation axes, for small angular misorientations, using electron backscatter diffraction in the SEM. *Journal of Microscopy* **195**, 217–225.

Prior, D.J., Boyle, A.P., Brenker, F., Cheadle, M.C., Day, A., Lopez, G., Peruzzo, L., Potts, G.J., Reddy, S., Spiess, R., Timms, N.E., Trimby, P., Wheeler, J., & Zetterström, L. (1999). The application of electron backscatter diffraction and orientation contrast imaging in the SEM to textural problems in rocks. *American Mineralogist*, **84**: 1741-1759.

Prior, D.J., Mariani, E. & Wheeler, J. (2009). EBSD in the Earth Sciences: Applications, Common Practice, and Challenges. In: *Electron Backscatter Diffraction in Materials Science, 2nd Edition*. New York: Springer, pp. 345-360.

Punin, Y.O., Shtukenberg, A.G., Smetannikova, O.G. & Amelin, K.S. (2009). Plagioclase tiwn associations from the basic volcanic rocks of the Kamchatkan, Russia: growth conditions and formation mechanisms. *European Journal of Mineralogy* **22**, 139-145.

Pupier, E., Duchene, S. & Toplis, M.J. (2008). Experimental quantification of plagioclase crystal size distribution during cooling of basaltic liquid. *Contributions to Mineralogy and Petrology* **155**, 555-570.

Randolph, A.D. & Larson, M.A. (1971). *Theory of Particulate Processes*. New York: Academic Press.

Reed, S.J.B. (1993). *Electron Microprobe Analysis*. Cambridge: Cambridge University Press.

Renner, J., Evans, B. & Hirth, G. (2002). Grain growth and inclusion formation in partially molten carbonate rocks. *Contributions to Mineralogy and Petrology* **142**, 501-514.

Renzulli, A., Del Moro, S., Menna, M., Landi, P. & Piermattei, M. (2009). Transient processes in Stromboli's shallow basaltic system inferred from dolerite and magmatic breccia blocks erupted during the 5 April 2003 paroxysm. *Bulletin of Volcanology* **71**, 795-813.

Resmini, R.G. (2007). Modeling of crystal size distributions (CSDs) in sills. *Journal of Volcanology and Geothermal Research* **161(1-2)**, 118-130.

Resmini, R.G. & Marsh, B.D. (1995). Steady-state volcanism, paleoeffusion rates, and magma system volume inferred from plagioclase crystal size distributions in mafic lavas; Dome Mountain, Nevada. *Journal of Volcanology and Geothermal Research* **68(4)**, 273–296.

Riker, J.M., Cashman, K.V., Kauahikaua, J.P. & Montierth, C.H. (2009). The length of channelized lava flows: Insight from the 1859 eruption of Mauna Loa Volcano, Hawai‘i. *Journal of Volcanology and Geothermal Research* **183**, 139-156.

Roedder, E. (1984). Fluid Inclusions. *Mineralogical Society of America and Geochemical Society, Reviews in Mineralogy and Geochemistry* **12**, 644 pp.

Roman, D.C. & Cashman, K.V. (2006). The origin of volcano-tectonic earthquake swarms. *Geology* **34**, 457-460.

Ross, J.V. (1957). Combination twinning in plagioclase feldspars. *American Journal of Science* **255**, 650-655.

Royet, J.-P. (1991). Stereology: A method for analyzing images. *Progress in Neurobiology* **37**, 433-474.

Rutherford, M.J. (2008). Magma ascent rates. In: Putirka, K.D. & Tepley III, F.J. (eds.) *Minerals, Inclusions and Volcanic Processes. The Mineralogical Society of America and Geochemical Society, Reviews in Mineralogy and Geochemistry* **69**, 241-271.

Rutherford, M.J. & Devine, J.D. (1996). Pre-eruption pressure-temperature conditions and volatiles in the 1991 dacitic magma of Mount Pinatubo. In: Newhall, C. & Punongbayan, R. (eds.) *Fire and Mud: Eruptions and Lahars of Mount Pinatubo, Philippines*. Seattle, WA: University of Washington Press, pp. 751-766.

Rutherford, M.J. & Devine, J.D. (1997). Changing magma conditions and ascent rates during the Soufriere Hills eruption on Montserrat. *GSA Today* **8**, 1-7.

Rutherford, M.J. & Gardner, J.E. (2000). Rates of magma ascent. In: Sigurdsson, H.S. (ed.) *Encyclopedia of Volcanoes*. San Diego, CA: Academic Press, pp. 207-218.

Rutherford, M.J. & Hill, P.M. (1993). Magma ascent rates from amphibole breakdown: experiments and the 1980-1986 Mount St. Helens eruptions. *Journal of Geophysical Research* **98**, 19667-19685.

Rutherford, M.J., Sigurdsson, H., Carey, S. & Davis, A. (1985). The May 18, 1980 Eruption of Mount St. Helens 1. Melt composition and experimental phase equilibria. *Journal of Geophysical Research* **90**, 2929-2947.

Ryerson, F.J., Weed, H.C. & Piwinskii, A.J. (1988). Rheology of subliquidus magmas 1: picritic compositions. *Journal of Geophysical Research* **93**, 3421-3436.

Sahagian, D.L. & Proussevitch, A.A. (1998). 3D particle size distributions from 2D observations; stereology for natural applications. *Journal of Volcanology and Geothermal Research* 84(3-4), 173-196.

Salisbury, M.J., Bohrson, W.A., Clynne, M.S., Ramos, F.C. & Hoskin, P. (2008). Multiple plagioclase crystal populations identified by crystal size distribution and in situ chemical data: implications for timescales of magma chamber processes associated with the 1915 eruption of Lassen Peak, CA. *Journal of Petrology* **49**, 1755-1780.

Saltikov, S.A. (1967). The determination of the size distribution of particles in an opaque material from a measurement of the size distributions of their sections. In: Elias, H. (ed.) *Proceedings of the Second International Congress for Stereology*. Berlin: Springer-Verlag, pp. 163-173.

Scandone, R. & Malone, S.D. (1985). Magma supply, magma discharge and readjustment of the feeding systems of Mount St. Helens during 1980. *Journal of Volcanology and Geothermal Research* **23**, 239-262.

Scandone, R., Cashman, K.V. & Malone S.D. (2007). Magma supply, magma ascent and the style of volcanic eruptions. *Earth and Planetary Science Letters* **253**, 513-529.

Schaskolsky, M. & Schubnikow, A. (1933). Über die künstliche Herstellung gesetzmässiger Kristallverwachsungen des Kalialauns. *Zeitschrift für Kristallographie* **85**, 1-16.

Schiavi, F., Walte, N. & Keppler, H. (2009). First in situ observation of crystallization processes in a basaltic-andesitic melt with the moissanite cell. *Geology* **37**, 963-966.

Schwartz, A.J., Kumar, M., Adams, B.L. & Field, D.P. (2009). *Electron Backscatter Diffraction in Materials Science, 2nd Edition*. New York: Springer, 403 pp.

Schwindinger, K.R. (1999). Particle dynamics and aggregation of crystals in a magma chamber with application to Kilauea Iki olivines. *Journal of Volcanology and Geothermal Research* **88**, 209-238.

Schwindinger, K.R. & Anderson, A.T. (1989). Synneusis of Kilauea Iki olivines. *Contributions to Mineralogy and Petrology* **103**, 187-198.

Sen, G., Borges, M. & Marsh, B.D. (2006). A case for short duration of Deccan Trap eruption. *EOS Transactions American Geophysical Union* **87(20)**, doi:10.1029/2006EO200001.

Shea, T., Larsen, J.F., Gurioli, L., Hammer, J.E., Houghton, B.F. & Cioni, R. (2009). Leucite crystals: Surviving witnesses of magmatic processes preceding the 79AD eruption at Vesuvius, Italy. *Earth and Planetary Science Letters* **281**, 88-98.

Smith, J.V. (1974a). *Feldspar Minerals, vol 1: Crystal Structure and Physical Properties*. New York: Springer-Verlag, 627 pp.

Smith, J.V. (1974b). *Feldspar Minerals, vol 2: Chemical and Textural Properties*. New York: Springer-Verlag, 690 pp.

Smith, R., Kilburn, C.R.J. & Sammonds, P.R. (2007). Rock fracture as a precursor to lava dome eruptions at Mount St Helens from June 1980 to October 1986. *Bulletin of Volcanology* **69**, 681-693.

Sisson, T.W. & Grove, T.L. (1993). Experimental investigations of the role of H20 in calc-alkaline differentiation and subduction zone magmatism. *Contributions to Mineralogy and Petrology* **113**, 143-166.

Spandler, C. & O'Neill, H.St.C. (2010) Diffusion and partition coefficients of minor and trace elements in San Carlos olivine at 1,300°C with some geochemical implications. *Contributions to Mineralogy and Petrology* **159**, 791-818.

Spiess, R., Peruzzo, L., Prior, D.J. & Wheeler, J. (2001). Development of garnet porphyroblasts by multiple nucleation, coalescence and boundary misorientation-driven rotations. *Journal of Metamorphic Geology* **19**, 269-290.

Stevenson, R.J., Dingwell, D.B., Webb, S.L. & Sharp, T.G. (1996). Viscosity of microlite-bearing rhyolitic obsidians: an experimental study. *Bulletin of Volcanology* **58**, 298-309.

Sunagawa, I. (1981). Characteristics of crystal growth in nature as seen from the morphology of mineral crystals. *Bulletin de Mineralogie* **104**, 81-87.

Sunagawa, I. (2005). *Crystals: Growth, Morphology, and Perfection*. New York: Cambridge University Press, 295 pp.

Suzuki, Y., Gardner, J.E. & Larsen, J.F. (2007). Experimental constraints on syneruptive magma ascent related to the phreatomagmatic phase of the 2000AD eruption of Usu volcano, Japan. *Bulletin of Volcanology* **69**, 423-444.

Szramek, L., Gardner, J.E. & Larsen, J. (2006). Degassing and microlite crystallization of basaltic andesite magma erupting at Arenal Volcano, Costa Rica. *Journal of Volcanology and Geothermal Research* **157**, 182-201.

Toothill, J., Williams, C. A., MacDonald, R., Turner, S. P., Rogers, N. W., Hawkesworth, C. J., Jerram, D. A., Ottley, C. J. & Tindle, A. G. (2007). A Complex Petrogenesis for an Arc Magmatic Suite, St Kitts, Lesser Antilles. *Journal of Petrology* **48**, 3-42.

Trimby, P.W., Prior, D.J. & Wheeler, J. (1998). Grain boundary hierarchy development in a quartz mylonite. *Journal of Structural Geology* **20**, 917–935.

Trua, T., Serri, G., Marani, M., Runzulli, A. & Gamberi, F. (2002). Volcanological and petrological evolution of Marsili Seamount (southern Tyrrhenian Sea). *Journal of Volcanology and Geothermal Research* **114**, 441-464.

Tuffen, H., Dingwell, D.B., & Pinkerton, H. (2003). Repeated fracture and healing of silicic magma generate flow banding and earthquakes? *Geology* **31**, 1089-1092.

Turner, S., George, R., Jerram, D.A., Carpenter, N. & Hawkesworth, C. (2003). Case studies of plagioclase growth and residence times in island arc lavas from Tonga and the Lesser Antilles, and a model to reconcile discordant age information. *Earth and Planetary Science Letters* **214**, 279-294.

Tuttle, O.F. & Bowen, N.L. (1958). Origin of granite in light of experimental studies in the system NaAlSi3O8—KalSi3O8—SiO2—H2O. *Geological Society of America Memoirs* **74**, 153 pp.

Underwood, E.E. (1970). Quantitative stereology. Reading, Massachusetts: Addison-Wesley.

Van der Plas, L. & Tobi, A.C. (1965). A chart for judging the reliability of point counting results. *American Journal of Science* **263**, 87-90.

Vance, J.A. (1969). On synneusis. *Contributions to Mineralogy and Petrology* **24**, 7-29.

Vance, J.A. & Gilreath, J.P. (1967). The effect of synneusis on phenocryst distribution patterns in some porphyritic igneous rocks. *American Mineralogist* **52**, 529-536.

Vinet, N. & Higgins, M.D. (2010). Magma solidification processes beneath KilaueaVolcano, Hawaii: a quantitative textural and geochemical study of the 1969-1974 Mauna Ulu lavas. *Journal of Petrology* **51**, 1297-1332.

Viola, C. (1902). Beitrag zur Zwillingsbildung. *Zeitschrift für Kristallographie* **36**, 234-244

Vogt, J.H.L. (1921). The physical chemistry of the crystallization and magmatic differentiation of igneous rocks. *The Journal of Geology* **29**, 318-350.

Voorhees, P.W. (1992). Ostwald Ripening of Two-Phase Mixtures. *Annual Review of Materials Science* **22**, 197-215.

Walker, D., Kirkpatrick, R.J., Longhi, J. & Hays, J.F. (1976). Crystallization history of lunar picritic basalt sample 12002: phase-equilibria and cooling-rate studies. *Geological Society of America Bulletin* **87**, 646-656.

Walker, D., Powell, M.A., Lofgren, G.E. & Hays, J.F. (1978). Dynamic crystallization of a eucrite basalt. *Proceedings of the 9th Lunar and Planetary Science Conference* **1**, 1369-1391.

Waters, C. & Boudreau, A. E. (1996). A reevaluation of crystal-size distributions in chromite cumulates. *American Mineralogist* **81**, 1452–1459.

Welsch, B., Faure, F., Famin, V., Baronnet, A. & Bachélery, P. (in review) Dendritic crystallization: A single process for all the textures of olivine in basalts. *Journal of Petrology*.

Wilson, L., Sparks, R.S.J. & Walker, G.P.L. (1980). Explosive volcanic eruptions, IV, The control of magma properties and conduit geometry on eruption column behaviour. *Geophysical Journal of the Royal Astronomical Society* **63**, 117-148.

Wong, L.J. & Larsen, J.F. (2010). The Middle Scoria sequence: A Holocene violent strombolian, subplinian and phreatomagmatic eruption of Okmok volcano, Alaska. *Bulletin of Volcanology* **72**, 17-31.

Zieg, M.J. & Lofgren, G.E. (2006). An experimental investigation of texture evolution during continuous cooling. *Journal of Volcanology and Geothermal Research* **154**, 74-88.

Zieg, M.J. & Marsh, B.D. (2002). Crystal size distributions and scaling laws in the quantification of igneous textures. *Journal of Petrology* **43**, 85-101.

Zhang, Y. & Behrens, H. (2000). H_2O diffusion in rhyolitic melts and glasses. *Chemical Geology* **169**, 243-262.

Zhang, Y., Stolper, E.M. & Wasserburg, G.J. (1991). Diffusion of water in rhyolitic glasses. *Geochimica et Cosmochimica Acta* **55**, 441-456.